

Seismic Crack Propagation and Structural Damage Analysis in Gravity Dams

Sanket Suresh Ingle

A Thesis

In the Department of

Building, Civil and Environmental Engineering

Presented in Partial Fulfillment of the Requirements

For the Degree of

Master of Applied Science (Civil Engineering) at

Concordia University

Montreal, Quebec, Canada

August 2025

© Sanket Suresh Ingle, 2025

CONCORDIA UNIVERSITY

School of Graduate Studies

This is to certify that the thesis prepared

By: **Sanket Suresh Ingle**

Entitled: **Seismic crack propagation and structural damage analysis in gravity dams**

and submitted in partial fulfillment of the requirements for the degree of

Master of Applied Science (Civil Engineering)

complies with the regulations of the University and meets the accepted standards with respect to originality and quality.

Signed by the final Examining Committee:

_____ Chair

Dr. Jassim Hassan

_____ Examiner

Dr. Hang Xu

_____ Examiner

Dr. Jassim Hassan

_____ Thesis Supervisor

Dr. Lan Lin

_____ Thesis Supervisor

Dr. Samuel Li

Approved by _____

Dr. Chunjiang An, Graduate Program Director

Dr. Mourad Debbabi, Dean of Gina Cody School of Engineering
and Computer Science

Abstract

Seismic Crack Propagation and Structural Damage Analysis in Gravity Dams

Sanket Suresh Ingle

Gravity dams are critical infrastructure for hydropower generation, water supply, irrigation, and flood control. However, their large mass and rigid geometry make them particularly vulnerable to seismic loading. The failure of such dams during earthquakes can result in catastrophic consequences, including loss of life, downstream infrastructure damage, and long-term environmental disruption. In regions of moderate seismicity like Eastern Canada, the risk is often underestimated due to limited historical damage records. This study addresses that gap by evaluating the seismic behavior of two concrete gravity dams using nonlinear finite element modeling techniques, with a specific focus on tensile cracking and structural degradation.

The investigation employed ABAQUS software to simulate the seismic response of concrete gravity dams under combined hydrostatic and earthquake loads. The Concrete Damaged Plasticity (CDP) model was used to represent the nonlinear behavior of concrete, including cracking, crushing, and stiffness degradation. Model validation was performed using the well-documented Koyna Dam in India, which experienced significant damage during the 1967 Mw 6.5 earthquake. The validation process involved modal analysis, crest displacement comparison, and tensile damage correlation to ensure the model's reliability before applying it to Canadian Dams.

Following validation, the same modeling approach was applied to two dams in Eastern Canada, Dam D1 (35 meters high) and Dam D2 (90 meters high) with consistent material properties. Both dams were assumed to have fixed bases, and soil-structure interaction effects were not explicitly included. A total of 22 ground motion records from the 1988 Mw 5.9 Saguenay Earthquake, collected from 11 recording stations, were used as seismic loading. Each record included both longitudinal and transverse components and was scaled to the design-level spectrum to simulate high-magnitude scenarios and observe potential damage thresholds.

The results revealed distinct differences in seismic response between the two dams. Dam D1, being shorter and stiffer, exhibited limited crest displacements and minor, localized

tensile cracking, mostly at the upstream heel. In contrast, Dam D2 experienced significantly higher crest displacements exceeding 100 mm in several simulations. And widespread tensile damage at both the crest and the base, especially under scaled acceleration records. The spatial and temporal patterns of damage indicated classic flexural behavior, with tension developing at the crest and heel due to cantilever action and stress wave reflection

These findings underscore the critical influence of dam geometry, mass, and natural frequency characteristics on seismic performance. The results emphasize the need for modal analysis in preliminary seismic safety assessments and demonstrate the value of nonlinear modeling techniques in capturing progressive damage. By applying realistic earthquake inputs from within the region, this study contributes to a better understanding of dam vulnerability in Eastern Canada and provides a framework for future seismic assessments and retrofit prioritization.

Acknowledgments

First and foremost, I bow my head in gratitude to God, whose constant presence, blessings, and grace have given me the strength and clarity to persevere through every step of this journey. His divine guidance has been my greatest support.

I extend my sincere thanks to my supervisors, Dr. Samuel Li and Dr. Lan Lin, for their valuable guidance, encouragement, and unwavering support throughout my research. Their mentorship has been vital to the completion of this thesis.

I am deeply thankful to my parents, Sushila and Suresh Ingle, for their unconditional love, sacrifices, and blessings. I am equally grateful to my brother Shubham for always standing by my side and inspiring me with his constant support.

I would also like to express my heartfelt appreciation to my friends for their encouragement, companionship, and emotional support, and to my colleagues for their collaboration and positive spirit throughout this academic journey.

To everyone who has supported me directly or indirectly, thank you from the bottom of my heart.

Table of Contents

| | |
|---|-----------|
| Chapter 1 : Introduction | 1 |
| 1.1 Background | 1 |
| 1.2 Motivation | 2 |
| 1.3 Research Objectives | 3 |
| 1.4 Methodology Overview..... | 4 |
| 1.5 Importance of the Study | 5 |
| 1.6 Organization of the Thesis | 5 |
| Chapter 2 : Literature Review..... | 7 |
| 2.1 Introduction | 7 |
| 2.2 Previous studies..... | 7 |
| 2.2.1 Historical seismic failures of gravity dams..... | 7 |
| 2.2.2 Linear and Nonlinear Analysis of Concrete Dams | 9 |
| 2.2.3 Numerical modeling using ABAQUS and CDP..... | 10 |
| 2.2.4 Seismic cracking and FEM..... | 11 |
| 2.2.5 Benchmark studies with Koyna dam | 12 |
| 2.2.6 Dam safety and fragility in eastern Canada | 12 |
| 2.3 Existing seismic design standards and code procedures | 13 |
| 2.3.1 Canadian seismic design standards for gravity dams | 14 |
| 2.3.2 International seismic guidelines for gravity dams | 15 |
| 2.4 Summary | 16 |
| Chapter 3 : Methodology | 19 |
| 3.1 Dam geometry | 19 |

| | | |
|--------------------|--|-----------|
| 3.2 | Finite element analysis method..... | 20 |
| 3.2.1 | Compressive stress-strain curve..... | 20 |
| 3.2.2 | Cracking and failure of concrete..... | 22 |
| 3.2.3 | Tensile and compressive damage..... | 26 |
| 3.3 | Loading on dam..... | 27 |
| 3.4 | Motions of dam elements..... | 28 |
| 3.5 | Natural Frequency of Dam..... | 29 |
| 3.6 | Scaling of Earthquake Records..... | 29 |
| Chapter 4 : | Results | 31 |
| 4.1 | Model Validation..... | 31 |
| 4.1.1 | Natural frequency of Koyna Dam..... | 33 |
| 4.1.2 | Seismic analysis..... | 34 |
| 4.2 | Natural frequencies of D1 and D2..... | 39 |
| 4.3 | Earthquake Input Records: Overview and Identification..... | 40 |
| 4.3.1 | Ground motion spectral properties and scaling..... | 41 |
| 4.4 | Results of tensile damage..... | 42 |
| 4.4.1 | Dam D1 – Response to original acceleration records..... | 42 |
| 4.4.2 | Dam D1 – Response to scaled acceleration records..... | 46 |
| 4.4.3 | Dam D2 – Response to original acceleration records..... | 56 |
| 4.4.4 | Dam D2 – Response to scaled acceleration records..... | 60 |
| 4.5 | Discussion..... | 67 |
| 4.5.1 | Heel Damage Mechanisms..... | 67 |
| 4.5.2 | Crest Damage Mechanisms..... | 67 |
| 4.5.3 | Crest Displacement Response..... | 68 |

| | | |
|---------------------|---|-----------|
| 4.5.4 | Modal Interaction Effects | 68 |
| 4.5.5 | Compressive Damage | 69 |
| 4.5.6 | Evaluation Framework and Comparative Insights..... | 69 |
| Chapter 5 : | Conclusions | 72 |
| 5.1 | Summary and Conclusions..... | 72 |
| 5.2 | Recommendations and Future Work..... | 73 |
| Chapter 6 : | References | 75 |
| Appendix A — | Abaqus input: Dam 1 (Modal Analysis)..... | 81 |
| Appendix B — | Abaqus input: Dam 1 (Seismic Analysis) | 87 |
| Appendix C — | Abaqus input: Dam 2 (Seismic Analysis) | 93 |

List of Figures

| | |
|---|----|
| Figure 3.1 Cross sections for dam: (a) D1; (b) D2 | 19 |
| Figure 3.2 Cross-section, showing the finite element mesh used for FE computations: (a) D1; (b) D2 | 20 |
| Figure 3.3 Stress-strain curve for concrete under compression..... | 21 |
| Figure 3.4 Stress-strain curve for concrete under tension..... | 23 |
| Figure 3.5 Response of concrete to uniaxial loading: (a) tension, (b) compression adapted from ABAQUS..... | 25 |
| Figure 3.6 Tensile damage parameter d_t vs cracking strain ϵ_t^{cr} | 26 |
| Figure 4.1 Cross-section of the Koyna Dam showing dimensions (Pekau and Feng 1995).... | 31 |
| Figure 4.2 (a) Scaled laboratory model of the Koyna Dam; (b) cross section of the scaled laboratory model dam, showing boundary element discretization used for numerical computation in Pekau and Feng (1995). | 32 |
| Figure 4.3 Time series of the transverse acceleration recorded during the 1967 earthquake.. | 34 |
| Figure 4.4 Comparison of horizontal crest displacement $u_{c(t)}$ between this study and ABAQUS (2006)..... | 35 |
| Figure 4.5 Comparison of tensile damage d_t results of Koyna Dam; (a) $t = 3.90$ s, (b) 3.93 s, (c) $t = 4.26$ s, (d) $t = 4.28$ s, (e) $t = 4.62$ s, (f) $t = 4.63$ s. | 37 |
| Figure 4.6 Comparison of tensile damage results of Koyna Dam. (a) $t = 4.10$ s, (b) 4.13 s, (c) $t = 4.25$ s, (d) $t = 4.44$ s, (e) $t = 10$ s, (f) $t = 10$ s..... | 38 |
| Figure 4.7 Graph showing horizontal crest displacement with time $u_{c(t)}$ for D1- site 7L.... | 43 |
| Figure 4.8 Contours of tensile damage d_t for D1 at time $t = 3$ s for site 7L. | 43 |
| Figure 4.9 Graph showing horizontal crest displacement with time $u_{c(t)}$ for D1- site 8L.... | 44 |
| Figure 4.10 Contours of tensile damage d_t for D1 at time $t = 11.78$ s for site 8L. | 44 |

| | |
|--|----|
| Figure 4.11 Graph showing horizontal crest displacement with time $u_{c(t)}$ for D1- site 20L. | 45 |
| Figure 4.12 Contours of tensile damage d_t for D1 at time $t = 11.78$ s for site 20L. | 46 |
| Figure 4.13 Graph showing horizontal crest displacement with time $u_{c(t)}$ for D1- scaled acceleration record site 1L. | 47 |
| Figure 4.14 Contours of tensile damage d_t for D1 at time: (a) $t = 11.96$ s; (b) $t = 14.26$ s; (c) $t = 16.15$ s; (d) $t = 17.74$ s for scaled acceleration record of site 1L. | 48 |
| Figure 4.15 Graph showing horizontal crest displacement with time $u_{c(t)}$ for D1- scaled acceleration record site 2L. | 49 |
| Figure 4.16 Contours of tensile damage d_t for D1 at time: (a) $t = 17.88$ s; (b) $t = 18.60$ s; (c) $t = 24.57$ s; (d) $t = 38.75$ s for scaled acceleration record of site 2L. | 50 |
| Figure 4.17 Graph showing horizontal crest displacement with time $u_{c(t)}$ for D1- scaled acceleration record site 7L. | 51 |
| Figure 4.18 Contours of tensile damage d_t for D1 at time: (a) $t = 0.34$ s; (b) $t = 0.75$ s; (c) $t = 4.52$ s; (d) $t = 17.74$ s for scaled acceleration record of site 7L. | 51 |
| Figure 4.19 Graph showing horizontal crest displacement with time $u_{c(t)}$ for D1- scaled acceleration record site 9L. | 52 |
| Figure 4.20 Contours of tensile damage d_t for dam 1 at time: (a) $t = 1.40$ s; (b) $t = 14.69$ s; (c) $t = 17.42$ s; (d) $t = 38.85$ s for scaled acceleration record of site 9L. | 53 |
| Figure 4.21 Graph showing horizontal crest displacement with time $u_{c(t)}$ for D1- scaled acceleration record site 10L. | 54 |
| Figure 4.22 Contours of tensile damage d_t for D1 at time: (a) $t = 13.51$ s; (b) $t = 14.05$ s; (c) $t = 17.89$ s; (d) $t = 32.90$ s for scaled acceleration record of site 10L. | 54 |
| Figure 4.23 Graph showing horizontal crest displacement with time $u_{c(t)}$ for D1- scaled acceleration record site 14L. | 55 |
| Figure 4.24 Contours of tensile damage d_t for dam 1 at time: (a) $t = 0.071$ s; (b) $t = 0.32$ s; (c) $t = 1.31$ s; (d) $t = 17.35$ s for scaled acceleration record of site 14L. | 56 |

Figure 4.25 Graph showing horizontal crest displacement with time $u_{c(t)}$ for D2- site 1T... 57

Figure 4.26 Contours of tensile damage d_t for D2 at time $t = 17.28$ s for record of site 1T... 58

Figure 4.27 Graph showing horizontal crest displacement with time $u_{c(t)}$ for D2- site 9T... 58

Figure 4.28 Contours of tensile damage d_t for D2 at time $t = 15.20$ s for record of site 9T... 59

Figure 4.29 Graph showing horizontal crest displacement with time uct for D2- site 20L.. 59

Figure 4.30 Contours of tensile damage d_t for D2 at time $t = 11.29$ s for record of site 20L. 60

Figure 4.31 Contours of tensile damage d_t for D2 at time: (a) $t = 13.74$ s; (b) $t = 17.29$ s; (c) $t = 14.26$ s for scaled acceleration record of site 1L. 61

Figure 4.32 Contours of tensile damage d_t for dam 2 at time: (a) $t = 14.83$ s; (b) $t = 15.13$ s; (c) $t = 16.83$ s; (d) $t = 39.06$ for scaled acceleration record of site 9L..... 62

Figure 4.33 Contours of tensile damage d_t for D2 at time: (a) $t = 14.78$ s; (b) $t = 17.03$ s; (c) $t = 17.75$ s; (d) $t = 39.15$ s for scaled acceleration record of site 9T. 63

Figure 4.34 Contours of tensile damage d_t for D2 at time: (a) $t = 0.27$ s; (b) $t = 0.53$ s; (c) $t = 6.91$ s; (d) $t = 17.75$ s for scaled acceleration record of site 14L..... 64

Figure 4.35 Contours of tensile damage d_t for dam 2 at time: (a) $t = 7.33$ s; (b) $t = 8.49$ s; (c) $t = 12.72$ s; (d) $t = 33.86$ s for scaled acceleration record of site 16L. 65

Figure 4.36 Contours of tensile damage d_t for dam 2 at time: (a) $t = 10.56$ s; (b) $t = 11.30$ s; (c) $t = 12.41$ s; (d) $t = 20.59$ s for scaled acceleration record of site 20L..... 66

List of Tables

| | |
|--|----|
| Table 3.1 Key parameters of concrete used in ABAQUS computation. | 24 |
| Table 4.1 Key parameters of concrete used in ABAQUS computation of the Koyna Dam in this study. | 33 |
| Table 4.2 Natural frequencies of the Koyna Dam. | 33 |
| Table 4.3 Comparison of displacement peaks with respective time. | 35 |
| Table 4.4 Natural frequencies of Dam D1 and D2 | 39 |
| Table 4.5 Saguenay earthquake records used in seismic simulations. | 40 |
| Table 4.6 Ground motion characteristics for Saguenay earthquake records. | 42 |

List of Symbols

| Symbol | Definition | Unit |
|------------|-----------------------------|-------------------|
| σ | Uniaxial stress | N/m ² |
| ϵ | Strain | Dimensionless |
| E | Young's modulus | N/m ² |
| E_o | Initial elastic modulus | N/m ² |
| m | Mass | Kg |
| V | Volume | m ³ |
| ρ | Mass density | kg/m ³ |
| ν | Poisson's ratio | Dimensionless |
| ξ | Damping ratio | Dimensionless |
| g | Acceleration due to gravity | m/s ² |
| F_g | Gravity load | N/m ³ |
| P | Hydrostatic pressure | N/m ² |
| h | Depth of water level | m |
| H | Total height of the Dam | m |
| F_s | Seismic load | N |
| M | Mass matrix | Kg |
| C | Damping matrix | N·s/m |

| | | |
|----------------------|--|------------------|
| K | Stiffness matrix | N/m |
| $u(t)$ | Displacement vector | m |
| $\dot{u}(t)$ | Velocity vector | m/s |
| $\ddot{u}(t)$ | Acceleration vector | m/s ² |
| $\ddot{u}_g(t)$ | Time-dependent ground acceleration | m/s ² |
| α and β | Rayleigh damping coefficients | |
| σ_c | Compressive Stress | MPa |
| σ_{c0} | Compressive yield stress | MPa |
| σ_{cu} | Ultimate compressive strength | MPa |
| f'_c | Compressive Strength | MPa |
| σ_t | Tensile stress | MPa |
| σ_{t0} | Cracking stress | MPa |
| ϵ_c | Compressive strain | Dimensionless |
| ϵ_0 | Strain at peak stress | Dimensionless |
| ϵ_{cu} | Ultimate compressive strain | Dimensionless |
| ϵ_t | Tensile strain | Dimensionless |
| ϵ_{cr} | Cracking strain | Dimensionless |
| ω_i | Angular frequency of the i 'th vibration | rad/s |
| ϕ_i | Eigenvector | Dimensionless |

| | | |
|-------------------|--------------------------------------|---------------|
| f_n | Frequency | Hz |
| T | Natural period | sec |
| $u_{c(t)}$ | Horizontal displacement at the crest | m |
| $u_{d(t)}$ | Absolute displacement of the dam | m |
| $u_{g(t)}$ | Ground displacement | m |
| d_t | Tensile damage variable | Dimensionless |
| d_c | Compressive damage variable | Dimensionless |
| ϵ_c^{pl} | Plastic strain in compression | Dimensionless |
| ϵ_t^{pl} | Plastic strain in tension | Dimensionless |
| ϵ_t^{cr} | Cracking strain | Dimensionless |
| ϵ_c^{in} | Crushing strain | Dimensionless |
| t | Temperature, | °C |
| f_i | Field variables | Hz |

Chapter 1 : Introduction

1.1 Background

Gravity dams are among the most vital civil structures globally, essential for hydroelectric power generation, flood control, irrigation, and water supply (Lee and Fenves, 1998). These structures rely primarily on their self-weight and geometric configuration to resist external forces such as hydrostatic pressure, uplift, and seismic excitation. As of 2022, there are over 59,000 large dams worldwide, and gravity dams account for a significant proportion due to their simplicity and strength as reported in International Commission on Large Dams (ICOLD, 2022).

From an energy point of view, gravity dams power a substantial portion of the global electricity supply. The Three Gorges Dam in China, a gravity-arch hybrid structure, is the world's largest hydroelectric facility. It has an installed capacity of 22,500 MW and generates over 100 terawatt-hours (TWh) of electricity annually, supplying power to more than 60 million people. Similarly, Hoover Dam in the United States produces approximately 4.2 billion kWh per year, serving around 1.3 million people across three states.

Gravity dams also play a central role in irrigation and agriculture, supporting over 1 billion hectares of farmland globally, directly impacting the food security of over 2 billion people. In India, the Bhakra Dam irrigates 10 million acres, while in Egypt, the Aswan High Dam supports year-round agriculture for millions of hectares (Tayie,2018). Many dams also serve as sources of drinking water, especially in arid and densely populated areas, such as Cape Town's Theewaterskloof Dam and Los Angeles's Owens River system. Equally important is the flood control function of gravity dams. These structures store excess runoff and mitigate downstream flooding risks. During the 2011 Missouri River flood, the U.S. Army Corps of Engineers' dam network prevented billions of dollars in damages (U.S. Army Corps of Engineers, 2012) Similarly, the W.A.C. Bennett Dam in British Columbia plays a critical role in managing peace River floods (Beltaos & Peters, 2020).

Despite their importance, gravity dams are susceptible to seismic vulnerability, especially older ones built before seismic design standards were standardized. The Fujinuma Dam in Japan failed catastrophically during the 2011 Tōhoku Earthquake, resulting in downstream flooding and loss of life (Tanaka et al., 2012). Similarly, Iran's Sefidrud Dam experienced significant crest

damage during the 1990 Manjil Earthquake, with peak accelerations exceeding 0.55g (Ghaemian & Ghobarah, 1997).

In the Canadian context, gravity dams are integral to national infrastructure. Canada is the third-largest producer of hydroelectric power globally, with hydropower accounting for ~60% of its total electricity generation. Major gravity dams such as Robert-Bourassa Dam (5,616 MW) in Quebec and W.A.C. Bennett Dam (2,730 MW) in British Columbia are integral to Canada's energy grid (Hydro-Québec, 2023). Moreover, Canadian dams provide municipal water supply, agricultural irrigation, and flood control, especially in densely populated provinces like Quebec and Ontario. According to the Canadian Dam Association (2013), there are over 933 large dams in Canada, with more than 60% constructed before 1970, often without seismic resilience in their original designs (CDA, 2013). In Eastern Canada, seismicity is classified as moderate, but the 1988 Saguenay Earthquake (Mw 5.9) revealed the region's susceptibility to damaging ground motion (Bernier et al., 2016).

1.2 Motivation

Given the critical role gravity dams play in hydroelectric generation, water supply, and flood mitigation, their structural integrity under seismic events is of great importance, particularly in regions with aging infrastructure and evolving seismic understanding. In Canada, more than 60% of the large dams were built prior to 1970, a period when seismic design considerations were either minimal or entirely absent (Canadian Dam Association, 2013). Despite Canada's classification as a region of moderate seismicity, past events such as the 1988 Saguenay Earthquake (Mw 5.9) revealed the potential for damaging ground motions in Eastern Canada, leading to increased scrutiny of the seismic resilience of critical infrastructure (Bernier et al., 2016).

Several Canadian studies have begun addressing dam vulnerability assessment. However, these are often based on linear-elastic or empirical criteria that fail to capture realistic damage mechanisms such as tensile cracking, stiffness degradation, and material failure (Segura et al., 2019; Duan et al., 2019). Moreover, there remains a lack of validated, nonlinear finite element models that simulate actual seismic damage progression in Canadian dams using region-specific earthquake records.

This research addresses that gap by implementing a nonlinear damage-based modeling framework using ABAQUS and the CDP model. It presents a detailed seismic assessment of two

gravity dams in Quebec D1 in Montreal and D2 in La Malbaie, subjected to both original and scaled ground motions from the 1988 Saguenay Earthquake. By explicitly incorporating each dam's geometry, material behavior, and modal analysis, the study captures localized failure mechanisms such as tensile cracking and crest displacement that are often overlooked in traditional linear approaches.

The novelty of this work lies in its application of site-specific earthquake records from an actual seismic event that occurred in Quebec, offering a rare regional case study. The use of scaled motions allows evaluation of performance under varying seismic intensities, aligning with modern performance-based design principles. Furthermore, by comparing the seismic responses of two dams with different structural configurations, this research highlights how geometry influences vulnerability and crack propagation, identifying critical damage zones particularly at the upstream heel and crest. The findings enhance the understanding of structural vulnerability under seismic loading and offer valuable input for seismic risk assessment.

1.3 Research Objectives

The primary aim of this thesis is to assess the seismic vulnerability of concrete gravity dams in Canada by leveraging nonlinear finite element modeling, ground motion scaling, and historical earthquake records. A core objective is the development of detailed finite element models for two representative gravity dams building on previous nonlinear FEM studies (Al Marahlleh, 2022; Alembagheri, 2016). These models are designed to accurately simulate the structural response of the dams under both static (hydrostatic) and dynamic (seismic) loading conditions, allowing for a comprehensive understanding of stress distribution and failure mechanisms. Another major goal is to estimate the fundamental vibration frequencies of the dams through modal analysis, a practice supported by established vibration testing approaches (Bader & Clayton, 2022).

A critical component of the study is the investigation of crack initiation and propagation. By employing the CDP model in ABAQUS, the research aims to examine how tensile damage develops over time, including its location, orientation, and severity under different seismic scenarios. This insight into crack behavior provides valuable information about the structural integrity and serviceability of the dams. Additionally, the study involves scaling the Saguenay Earthquake ground motion records to the design level. This step simulates more intense seismic events to explore damage thresholds and capture nonlinear structural responses, expanding on prior

vulnerability studies (Yazdani & Alembagheri, 2017). Finally, the research evaluates overall seismic performance by comparing the structural behavior of the dams under both original and scaled earthquake inputs. This comparison identifies critical crack zones, helps quantify displacement responses, and reveals how dam geometry and frequency characteristics affect vulnerability. Collectively, these objectives support a more informed and realistic approach to dam safety assessment under seismic loading.

1.4 Methodology Overview

This research adopts a nonlinear finite element approach to assess the seismic vulnerability of two concrete gravity dams located in Eastern Canada. The methodology consists of four main stages:

1. Finite Element Modeling:

Two dams, labeled D1 and D2, were selected for this study. Dam D1 is 35 meters high with a base width of 27 meters, while Dam D2 stands 90 meters high with a 70-meter base. Both models were developed using ABAQUS software and were assigned identical material properties to enable direct comparison. The models were meshed using 2D plane strain elements (CPE4R) and subjected to gravity, hydrostatic, and seismic loading.

2. Model Validation:

The modeling technique was validated using the well-documented Koyna Dam in India, which experienced notable seismic damage during the 1967 Mw 6.5 earthquake. Validation focused on matching natural frequencies and tensile damage patterns to ensure accuracy before applying the method to Canadian dams.

3. Seismic Loading:

Ground motion records were sourced from the 1988 Mw 5.9 Saguenay Earthquake, one of the most significant seismic events in Eastern Canada. Data from 11 recording sites were used, with both longitudinal and transverse components. Each record was scaled to the design-level spectrum using SeismoLEE software to simulate more severe seismic scenarios and better evaluate structural thresholds.

4. Finite Element Analysis:

Dynamic simulations were performed in ABAQUS using the CDP model, which captures nonlinear concrete behavior such as cracking, stiffness degradation, and crushing. The analysis

emphasized crest displacements and the spatial evolution of tensile damage to assess failure mechanisms under both original and scaled excitations.

This methodological framework provides a comprehensive basis for evaluating seismic performance and identifying structural vulnerabilities in gravity dams, particularly in seismically moderate regions like Eastern Canada.

1.5 Importance of the Study

This study plays a vital role in helping engineers, regulators, and dam operators assess the seismic reliability of gravity dams, particularly in regions like Eastern Canada where moderate seismicity is often underestimated. Through nonlinear finite element simulations incorporating both original and scaled earthquake records, the analysis captures how dam geometry and dynamic behavior influence structural performance. It highlights critical damage-prone zones, such as the upstream heel and dam crest, which are especially vulnerable to tensile cracking under seismic loading.

The findings provide actionable insights for retrofit planning, inspection prioritization, and performance-based maintenance strategies. Unlike traditional linear analyses, this approach captures progressive material degradation and cracking mechanisms that reflect realistic seismic response. The modeling method is adaptable to other dam sites with minimal modifications, making it a practical tool for broader seismic risk assessment. By combining advanced analysis techniques with region-specific earthquake data, the study contributes valuable technical evidence to inform future updates in dam safety regulations and long-term infrastructure resilience planning.

1.6 Organization of the Thesis

The thesis is organized into the following chapters:

Chapter 1 – Introduction: This chapter presents the background and significance of gravity dams in global and Canadian contexts. It discusses the seismic risks associated with these structures, particularly in regions like Eastern Canada. The chapter outlines the research motivation, defines the study's objectives, describes the modeling methodology, and highlights the importance of assessing dam performance under realistic seismic scenarios.

Chapter 2 - Literature Review: This chapter reviews prior research related to the seismic performance of gravity dams, with a focus on failure mechanisms, modeling techniques, and existing design standards. It begins by examining historical dam failures caused by earthquakes

and the lessons learned from those events. Key developments in numerical modeling are discussed, particularly the use of ABAQUS and the CDP model to simulate cracking and material degradation. The chapter also explores benchmark studies using the Koyna. Finally, relevant national and international seismic codes are reviewed to contextualize the modeling choices and analysis procedures used in this research.

Chapter 3 - Methodology: This chapter describes in detail the steps taken to build, validate, and analyze the finite element models. It explains the geometry selection, material properties, meshing strategy, boundary conditions, loading types (gravity, hydrostatic, and seismic), and scaling of earthquake records. It also outlines the rationale for choosing the CDP model and how model validation is carried out using the Koyna Dam case.

Chapter 4 - Results: This chapter presents the outcomes of the nonlinear seismic analyses conducted on Dam D1 and Dam D2. It includes detailed results on crest displacements, tensile damage patterns, and the spatial distribution of cracking under both original and scaled Saguenay earthquake records. Subsections highlight damage mechanisms at the crest and heel, differences in modal response, and the influence of dam geometry on structural vulnerability. A comparative evaluation between the two dams is provided, supported by contour plots, displacement graphs, and technical interpretation of results.

Chapter 5 – Conclusion: This chapter summarizes the key findings of the study, emphasizing the effects of geometry, material response, and seismic loading on damage development in gravity dams. It outlines the study's technical contributions to nonlinear modeling and seismic risk assessment, particularly for structures in Eastern Canada. Limitations of the current modeling approach are acknowledged, including assumptions related to dam–foundation interaction. The chapter concludes with practical recommendations for future research, including incorporating soil-structure interaction, and expanding the framework to other dam sites.

Chapter 2 : Literature Review

2.1 Introduction

Concrete gravity dams are essential components of water infrastructure worldwide, some of them are located in regions of moderate to high seismicity. The potential for catastrophic failure due to seismic loading necessitates robust methods for safety and stability assessment. Historically, dam safety analyses have relied on simplified analytical methods or empirical seismic design provisions. Past earthquake-induced dam failures have shown the inadequacy of such traditional approaches. The 1967 Koyna earthquake in India caused severe cracking in the gravity dam, highlighting the need for seismic design in dam engineering.

With advancements in computational engineering, tools like ABAQUS have become indispensable for evaluating dam performance under various loading scenarios. These tools incorporate complex material models and dynamic analysis capabilities that enable researchers to simulate real-world conditions with increasing accuracy. In particular, ABAQUS offers built-in constitutive models such as the Concrete Damage Plasticity (CDP) model, which allows for detailed representation of cracking, crushing, and other nonlinear behaviors in concrete structures. The platform also supports both implicit and explicit time integration schemes, enabling simulations of transient dynamic loading such as earthquakes. Its flexibility in handling large deformations and contact interactions makes it a valuable tool for structural assessments.

This chapter presents a comprehensive review of literature relevant to the modeling, assessment, and design of gravity dams under seismic loading. Emphasis is given to numerical modeling using ABAQUS, developments in concrete damage modeling and validation studies using the Koyna Dam.

2.2 Previous studies

2.2.1 Historical seismic failures of gravity dams

Understanding seismic-induced failure in gravity dams is essential before discussing modeling techniques. Real-world failures provide critical insights into the mechanisms of structural breakdown, especially under seismic loading. Several case studies, including the Koyna Dam (India), Fujinuma Dam (Japan), and Sefidrud Dam (Iran), have been instrumental in shaping

seismic safety standards and model validation approaches in dam engineering (Tanaka et al., 2012; Tidke & Adhikary, 2021).

The Koyna Dam, damaged in the 1967 earthquake (Mw 6.5), remains the most studied gravity dam failure worldwide. Cracks developed along construction joints and near the crest of the dam, primarily due to high horizontal accelerations and insufficient provision for dynamic loads. This failure prompted the inclusion of seismic design provisions in Indian dam codes and served as a benchmark for seismic modeling (Chopra & Chakrabarti, 1973; Pekau et al., 1995).

Another significant incident was the Fujinuma Dam failure in Japan during the 2011 Tōhoku earthquake. Although it was an embankment dam, it underscores the consequences of underestimating seismic hazard. The dam's total collapse, which led to downstream fatalities, illustrates how older dam infrastructure not retrofitted for seismic loading can catastrophically fail. While not a concrete gravity dam, the event emphasized the urgent need for safety reassessment of all dam types under extreme seismic loading (Matsumoto et al., 2012; Tanaka et al., 2012).

In Iran, Sefidrud Dam experienced damage in the 1990 Manjil earthquake. The recorded crest acceleration exceeded 0.55g, resulting in longitudinal and transverse cracking. The dynamic amplification and resonance effects were cited as primary causes of structural damage. Post-event studies emphasized the role of hydrodynamic pressure, dam-foundation interaction, and energy dissipation mechanisms, guiding future analytical modeling approaches (Ghaemian & Ghobarah, 1997).

In their study of Pine Flat Dam, Chávez and Fenves (1995) demonstrated that seismic ground motions can induce substantial stresses and displacements in concrete gravity dams, reinforcing the importance of dynamic analysis for evaluating structural performance (Chavez & Fenves, 1995).

Ground motion characteristics play a critical role in determining the seismic response of gravity dams. Variations in amplitude, frequency content, and duration can significantly influence stress distribution, crack initiation, and displacement patterns (Sesli et al., 2016; Zou et al., 2017). Bray and Rodriguez-Marek emphasized that certain ground motion features, such as high velocity pulses and long-period content can amplify structural demands (Bray & Rodriguez-Marek, 2004). Similarly, Yazdani and Alembagheri (2017) showed that even under standard seismic conditions, dynamic amplification effects can result in localized damage, particularly near the dam crest and heel. In addition, Chen et al. (2019) and Mansouri et al. (2011) highlighted failure modes and

fracture mechanisms in large concrete gravity dams subjected to seismic excitation. These studies highlight the importance of using representative and properly scaled ground motion records to ensure that structural analyses capture the realistic demands imposed by seismic loading (Yazdani & Alembagheri, 2017). In this thesis, these insights support the selection and scaling of earthquake inputs for dynamic analysis and underscore the need for detailed stress evaluation in seismic performance assessment.

These case studies and research findings highlight the key factors influencing seismic vulnerability in gravity dams. Critical mechanisms include stress concentration, crack propagation, and dynamic amplification during strong ground motions. Scaled earthquake records are used to evaluate displacements and identify potential crack zones. The ABAQUS platform, combined with the CDP model, enables simulation of inelastic concrete behavior and crack development. This approach supports performance-based seismic assessment within a practical and computationally efficient framework.

2.2.2 Linear and Nonlinear Analysis of Concrete Dams

2.2.2.1 Linear analysis

In linear analysis, concrete is assumed to behave as a homogeneous, isotropic, and perfectly elastic material throughout the loading history. This approach is widely used in early seismic studies of dams due to its computational simplicity and ability to capture global response parameters such as modal frequencies, crest displacements, and hydrodynamic effects (Chopra, 1973; Lin & Adams, 2008). However, linear analysis does not consider material degradation processes such as cracking, crushing, or stiffness reduction under repeated or large seismic loads. As a result, it can provide only a first-order estimate of dam response, and it is often insufficient for identifying localized damage mechanisms or predicting progressive failure. For example, linear time-history analyses of the Koyna Dam captured overall displacement trends but failed to reproduce observed cracking patterns at the crest and heel (Alembagheri, 2016).

2.2.2.2 Nonlinear analysis

Nonlinear analysis incorporates both material nonlinearity (tensile cracking, compressive crushing, stiffness degradation) and, in some cases, geometric nonlinearity (large displacements, sliding, uplift). This is typically achieved through advanced constitutive models such as fracture mechanics, smeared crack approaches, or plastic-damage formulations. Among these, the CDP

model in ABAQUS has become widely adopted due to its ability to simulate isotropic damage, tensile softening, and cyclic degradation (Lubliner et al., 1989; Lee & Fenves, 1998; Hafezolghorani et al., 2017; Lei et al., 2023). Unlike linear analysis, nonlinear approaches allow the simulation of crack initiation, propagation, and eventual instability under dynamic loading, providing a realistic representation of seismic damage evolution. Studies of the Koyna and Sefidrud Dams, for instance, demonstrated that nonlinear finite element models reproduced observed cracking locations and magnitudes far more accurately than linear methods (Ghaemian & Ghobarah, 1997; Duan et al., 2019).

2.2.2.3 Rationale for this study

Given the focus of this thesis on seismic crack propagation and damage assessment, nonlinear analysis was adopted. While linear methods are useful for preliminary assessments, they underestimate tensile failure at critical stress concentration zones, such as the upstream heel and crest. Nonlinear modeling, particularly with the CDP framework, allows the explicit representation of stiffness softening, stress redistribution, and localized damage under both original and scaled earthquake inputs. By capturing these progressive damage mechanisms, the adopted approach provides a more reliable basis for seismic safety evaluation and retrofit planning for Canadian dams

2.2.3 Numerical modeling using ABAQUS and CDP

Abaqus provides multiple constitutive models for simulating cracking in concrete, including the smeared crack model, the brittle cracking model, and the more CDP model. The smeared crack model represents cracks as distributed strains over elements but suffers from mesh dependency and limited post-cracking behavior. The brittle cracking model focuses on tensile failure initiation but neglects compressive crushing and cyclic degradation. In contrast, the CDP model combines plasticity theory and damage mechanics, enabling simultaneous simulation of tensile cracking, compressive crushing, and stiffness degradation. Owing to these advantages, CDP has become the preferred approach in nonlinear seismic analysis of concrete dams (Lubliner et al., 1989; Lee & Fenves, 1998). FEM plays an important role in the seismic assessment of civil infrastructure. ABAQUS is commonly employed in research and engineering practice to simulate nonlinear concrete behavior using the CDP model (Serra et al., 2017; Madandoust et al., 2017). The CDP model incorporates principles from plasticity theory and damage mechanics, allowing

representation of both tensile cracking and compressive crushing in concrete. This enables detailed analysis of structural response under seismic loading conditions. Accurate seismic assessment of gravity dams requires considering the coupled effects of dam, reservoir, and foundation rock interaction.

Sarkhel et al. (2020) employed ABAQUS to develop a two-dimensional finite element model of the Koyna Dam using the CDP model to represent nonlinear concrete behavior. The study demonstrated that the CDP formulation was effective in capturing tensile cracking and compressive crushing, which are critical failure modes in seismic response analysis of concrete dams. The study showed that the CDP model was effective in capturing key damage mechanisms such as tensile cracking under seismic loading. The resulting stress distributions and displacement patterns were consistent with those reported in earlier numerical studies on the Koyna Dam, supporting the model's applicability for seismic response analysis. The use of ABAQUS facilitated detailed tracking of stress development and displacement fields, enabling realistic assessment of damage mechanisms under dynamic loading. These findings affirm the suitability of ABAQUS and the CDP model for evaluating seismic performance of gravity dams, especially when the focus is on internal stress evolution and crack formation (Sarkhel et al., 2020).

A significant contribution to practical implementation came from Hafezolghorani et al., who developed a simplified tabular format for CDP parameters for common concrete grades. Their Simplified CDP (SCDP) model was validated using prestressed beams and compared favorably with empirical data and other numerical models (Hafezolghorani et al., 2017). Foundational work by Lubliner et al. (1989) and subsequent enhancements by Grassl et al. (2013) have shaped the development of the CDP model widely used in ABAQUS (Grassl et al., 2013). These studies introduced a framework that accounts for both tensile cracking and compressive crushing in concrete, making it suitable for simulating nonlinear behavior under seismic loading. Although originally developed for general concrete structures, the CDP model has been applied effectively in dam simulations to assess stress concentrations, damage initiation, and crack propagation (Lei et al., 2023; Lubliner et al., 1989). conditions.

2.2.4 Seismic cracking and FEM

Cracking under seismic loads is a primary concern in concrete dams. The Finite Element Method (FEM) enables the modeling of discontinuities without remeshing, making it suitable for crack initiation and propagation studies (Jiang et al., 2013; Zhang et al., 2013; Qu et al., 2020; Zou et al.,

2017) conducted a seismic study of Longtan Dam using Extended FEM (XFEM) and applied Koyna earthquake records as input motion. Their study showed early crack initiation and propagation leading to changes in dam stiffness and damping characteristics. The results validated XFEM as a powerful tool in dam safety modeling. Similarly, some studies demonstrated crack trajectories using FEM in ABAQUS and emphasized its potential in identifying failure modes before catastrophic outcomes.

A unique aspect of FEM is its ability to simulate crack paths within the dam body and foundation rock.(Zhai et al., (2022); Zhang et al., 2013; Xu et al., 2022) In seismic analysis, this allows engineers to evaluate failure progression without requiring prior knowledge of crack locations. The use of dynamic XFEM with cohesive segment modeling has shown that crack velocity, branching, and arrest phenomena can all be realistically captured. Researchers also integrate XFEM with Rayleigh damping and strain-rate dependent material models to improve accuracy.

2.2.5 Benchmark studies with Koyna dam

The Koyna Dam in India is widely used as a benchmark for validating numerical models. It experienced substantial damage during the 1967 earthquake, making it a valuable case for seismic analysis. Pekau (1973) and Zou (2017) utilized a strain-space cracking model to simulate the failure pattern observed in the Koyna Dam. Their findings showed good agreement with observed crack profiles, affirming the model's predictive capability.

Chopra and Chakrabarti (1981) developed a hydrodynamic pressure model that accounted for dam-reservoir interaction, a critical element often neglected in simplified analyses. Koyna simulations also demonstrate the importance of mesh size, element type (e.g., CPE4R vs. CAX4R), and time integration schemes (implicit vs. explicit) in capturing seismic response. Many studies have extended the original 2D models to 3D configurations, allowing better simulation of stress concentrations and modal interactions.

2.2.6 Dam safety and fragility in eastern Canada

In Eastern Canada, particularly in regions such as Quebec, seismicity is moderate but non-negligible, especially considering the presence of aging dam infrastructure. Many gravity dams in this area were constructed before the introduction of modern seismic design standards, creating a growing need for re-evaluation using contemporary analytical approaches. These structures are

increasingly vulnerable not only due to their age but also due to evolving understandings of regional seismic hazard.

Several Canadian studies have explored seismic risk in this context. Segura et al. (2019) developed fragility curves for a case-study dam in northeastern Canada using a probabilistic framework based on the Generalized Conditional Intensity Measure (GCIM). Their method incorporated spectral acceleration and peak ground velocity to estimate failure probabilities associated with sliding and cracking. While their work offers a valuable probabilistic approach, it relies on simplified modeling assumptions and does not capture the localized damage mechanisms that can arise during dynamic events. (Segura et al., 2019)

Similarly, Bernier et al. assessed seismic fragility using conditional spectrum-based analysis for Eastern Canadian dams, considering overturning, sliding, and uplift. Their study emphasized the importance of foundation properties and variability in ground motions. However, their models abstract some nonlinear material behaviors and do not explore detailed damage progression such as cracking patterns or internal stress evolution. (Bernier et al. 2016)

These studies collectively demonstrate growing interest in seismic risk assessment for Canadian dams. However, they primarily emphasize system-level failure modes and statistical estimation methods. In contrast, this thesis focuses on nonlinear finite element modeling to investigate detailed seismic responses of gravity dams, including crack formation and internal damage mechanisms under scaled ground motion records

2.3 Existing seismic design standards and code procedures

Evaluating the seismic safety of gravity dams requires adherence to well-established design codes and engineering guidelines. These frameworks are essential for ensuring that dam structures can withstand seismic loading without catastrophic failure. The design criteria outlined in both national and international codes aim to standardize safety margins, improve modeling accuracy, and minimize seismic risk for aging infrastructure. They typically include performance-based requirements, definitions of design earthquake levels, and recommendations for nonlinear dynamic analysis. These documents also emphasize the need to consider dam-reservoir interaction, and hydrodynamic pressure when assessing seismic vulnerability. The increasing reliance on finite element simulations and time-history analysis has further shaped the modern code requirements, pushing toward more accurate and region-specific seismic evaluations. This section reviews key

Canadian and global guidelines relevant to gravity dam assessment and identifies how they support the modeling strategies used in this study.

2.3.1 Canadian seismic design standards for gravity dams

In Canada, the seismic evaluation of gravity dams is governed by two principal regulatory documents: Dam Safety Guidelines (Canadian Dam Association or CDA, 2013) and the National Building Code of Canada 2010 or NBCC 2010 (National Research Council of Canada, 2010). The CDA Guidelines offer a comprehensive, risk-informed framework that classifies dams based on the consequences of failure and assigns performance requirements accordingly. A core feature of this framework is the specification of three earthquake levels-Operating Basis Earthquake (OBE), Maximum Design Earthquake (MDE), and Maximum Credible Earthquake (MCE). The OBE represents a relatively frequent, lower-intensity event under which a dam must remain fully operational without damage. The MDE corresponds to a stronger but less frequent event, where limited, repairable damage is acceptable, provided there is no loss of function or reservoir control. The MCE, by contrast, is the largest plausible event a dam could experience, and structures must be able to avoid catastrophic failure even if significant damage occurs. These categories ensure that dam performance is tailored to the level of risk posed by each structure and its surroundings. The CDA guidelines also advocate for nonlinear time-history analysis (NLTHA), particularly for Dams where failure could cause major damage like those investigated in this thesis. This enables a more detailed assessment of inelastic behavior, including tensile cracking and stiffness degradation. Site-specific seismic hazard analysis is also recommended, using techniques such as the Conditional Mean Spectrum (CMS) or Generalized Conditional Intensity Measure (GCIM), which allow engineers to model seismic demand more accurately by reflecting regional ground motion characteristics.

The CDA framework also emphasizes the importance of modeling various structural and environmental interactions, including reservoir-dam hydrodynamic effects and potential cracking behavior. This is especially pertinent for the two dams studied in this thesis, as both were modeled under hydrostatic and seismic loads using ABAQUS and the CDP model. Complementing the CDA, NBCC 2010 outlines national seismic design provisions and hazard maps, developed using probabilistic methods. It defines a 2% probability of exceedance in 50 years, equivalent to a 2,475-year return period, for determining seismic loading intensity. The NBCC 2010 mandates dynamic analysis, either modal response spectrum or nonlinear time-history methods depending on the

infrastructure's classification. Its inclusion of importance factors ensures that structures like dams, which serve critical public functions, are held to higher safety standards. In a study by Duan et al. (2019), these Canadian codes were applied to evaluate the seismic performance of gravity dams D1 and D2 using ABAQUS. Their findings confirmed the practical utility of the codes and reinforced the importance of incorporating geometry, material properties, and site-specific seismicity into dam modeling and safety evaluations.

2.3.2 International seismic guidelines for gravity dams

Globally, Seismic safety assessment of gravity dams is a global concern, addressed by several internationally recognized institutions that have developed comprehensive technical guidelines. Among these, the Federal Emergency Management Agency or FEMA (2005) in the United States plays a leading role. FEMA (2005) guidelines provide a structured framework for evaluating seismic loads, modeling dam response, and inspecting damage after an earthquake. Key areas of emphasis include the analysis of cracking, base sliding mechanisms, and the application of both simplified and advanced modeling techniques such as the FEM and XFEM. The guidelines also recommend incorporating hydrodynamic pressure effects using established methods like Westergaard's approach, which is particularly relevant when simulating the dam-reservoir interaction under dynamic conditions. These tools and procedures are directly applicable to the type of numerical simulations performed in this study, offering useful reference standards for validating modeling strategies in seismic evaluation.

The International Commission on Large Dams or ICOLD (2022) also provides essential recommendations for the seismic design and assessment of dams through its Bulletin 148. It stresses the need for site-specific seismic hazard analysis, which includes regional geological investigation and the use of detailed hazard curves tailored to each dam's location. ICOLD (2022) advocates the development of three-dimensional dynamic models for large dams, taking into account reservoir sloshing effects and foundation damping. These recommendations align with the modeling decisions made in this thesis, where localized ground motions and site characteristics were incorporated to better assess the response of Canadian gravity dams under the Saguenay Earthquake scenario. In addition, although the American Concrete Institute's (2014) ACI 318-14 is not dam-specific, it provides structural design criteria for concrete elements that are relevant to the structural components of gravity dams. Clauses related to critical section detailing, pile cap behavior, and flexural or shear performance of footings serve as supplementary guidance,

particularly when considering base stress distribution and reinforcement planning for dam foundations.

Lastly, the United States Army Corps of Engineers (USACE) has developed the EM 1110-2-2200 guidelines (U.S. Army Corps of Engineers, 2003), which offer a dam-specific design framework. These standards cover a wide range of seismic evaluation topics, including the generation of earthquake ground motion spectra, assessment of sliding resistance, and checks for overturning moments under dynamic conditions. USACE procedures often emphasize stability evaluation through safety factors and capacity-demand ratios under seismic scenarios, making them a valuable reference for assessing the structural safety of dams subjected to intense ground shaking. Overall, these international guidelines provide foundational knowledge and technical methodologies that complement national standards. The practices outlined by FEMA (2005), International Commission on Large Dams (2022), American Concrete Institute (2014) and USACE support the modeling strategy adopted in this study and reinforce the importance of integrating hydrodynamic forces, material behavior, and structural dynamics in seismic safety evaluations of gravity dams.

2.4 Summary

This chapter provides a comprehensive review of the existing body of knowledge on the seismic performance of concrete gravity dams, emphasizing both practical case studies and advanced numerical modeling methods. The introduction establishes the significance of evaluating seismic vulnerability in gravity dams, particularly in moderate-to-high seismic zones. Traditional empirical and linear methods are acknowledged for their limitations, especially in light of historical failures such as the 1967 Koyna earthquake, which demonstrated the critical need for robust seismic design and performance-based assessments. Tools like ABAQUS and the Concrete Damage Plasticity (CDP) model have gained traction for simulating realistic nonlinear responses, including cracking and crushing, under dynamic loading. These tools form the basis of contemporary seismic safety evaluations and are pivotal to the modeling approach adopted in this thesis.

The subsequent sections examine prior research and international case studies to contextualize dam failures under earthquake loading. Notable events such as the collapse of Fujinuma Dam in Japan and damage to the Sefidrud Dam in Iran highlight recurring seismic

vulnerabilities, particularly stress concentration and tensile cracking at the crest and heel. These events underscore the importance of selecting representative ground motion records and scaling methods in simulation studies. Researchers such as Yazdani & Alembagheri (2017), Bray & Rodriguez-Marek (2004), and Alembagheri (2016) have emphasized the influence of ground motion characteristics on structural response, reinforcing the need for time-history analysis. The literature supports the use of scaled regional records to capture stress distributions and failure mechanisms accurately, as done in this study using Saguenay Earthquake data.

Advanced modeling efforts are further explored through discussions on ABAQUS and the CDP model. The reviewed studies show the effectiveness of these tools in capturing damage mechanisms in dam structures. Sarkhel et al. (2020) validated the CDP model for the Koyna Dam, while others like Hafezolghorani et al. (2017) introduced simplified parameter schemes to increase modeling efficiency. Foundational contributions by Lubliner and Grassl helped establish CDP as a standard for nonlinear concrete modeling. The (FEM) and its extension, XFEM, are recognized for their capability to simulate crack initiation and propagation without predefining crack paths, making them suitable for dam safety assessments. These insights affirm the selection of CDP and FEM techniques in this thesis.

Several benchmark studies, particularly those involving the Koyna Dam, demonstrate how mesh density, element types, and time integration choices affect simulation accuracy. These studies provide essential validation frameworks for seismic modeling and support the approach used in this research. Additionally, dam safety assessments in Eastern Canada are reviewed, with a focus on fragility curves, probabilistic modeling, and structural vulnerability. Research by Segura et al. (2019) outlines system-level risks and statistical estimations but lacks the damage-specific resolution offered by nonlinear modeling approaches (Segura et al., 2019; Bernier et al., 2016). This thesis aims to bridge that gap by capturing progressive tensile damage under realistic seismic input.

Finally, the chapter explores seismic design standards and regulatory frameworks that guide gravity dam evaluations. Canadian codes like the Dam Safety Guidelines (Canadian Dam Association, 2013) and NBCC (2010) advocate performance-based assessments using nonlinear methods, site-specific hazard analysis, and regional scaling techniques. The use of design earthquakes such as OBE, MDE, and MCE ensures that dam responses are evaluated across a spectrum of seismic intensities. Internationally, guidelines from FEMA, ICOLD, USACE, and

ACI provide complementary methodologies for seismic safety, including recommendations for dam-reservoir interaction, 3D dynamic modeling, and foundation damping. Together, these codes inform the modeling framework in this thesis and reinforce the need for realistic and region-specific seismic evaluation.

Chapter 3 : Methodology

3.1 Dam geometry

This study analysed the structural performance of two concrete gravity dams: dam D1, located in Montreal, Quebec; dam D2, located in La Malbaie, Quebec, which were considered in Duan et al. (2019). The geometries of the dams are as follows (Fig. 3.1): D1 had a top width of $T_w = 5$ m, a base width of $B_w = 27.5$ m, a depth of upstream water $h = 32$ m, and a total height of $H = 35$ m, whereas D2 had the same top width as D1, a base width of $B_w = 70$ m. As illustrated in Fig. 3.1, the crest elevations of both dams are similar; specifically, the crest is located 3 m below the top of D1 and 4 m below the top of D2. The face slopes were 1:0.282 for D1 and 1:0.793 for D2. Dam D1 and Dam 2 are considered to represent low and high dams, respectively, in the areas of moderate and high seismicity in eastern Canada.

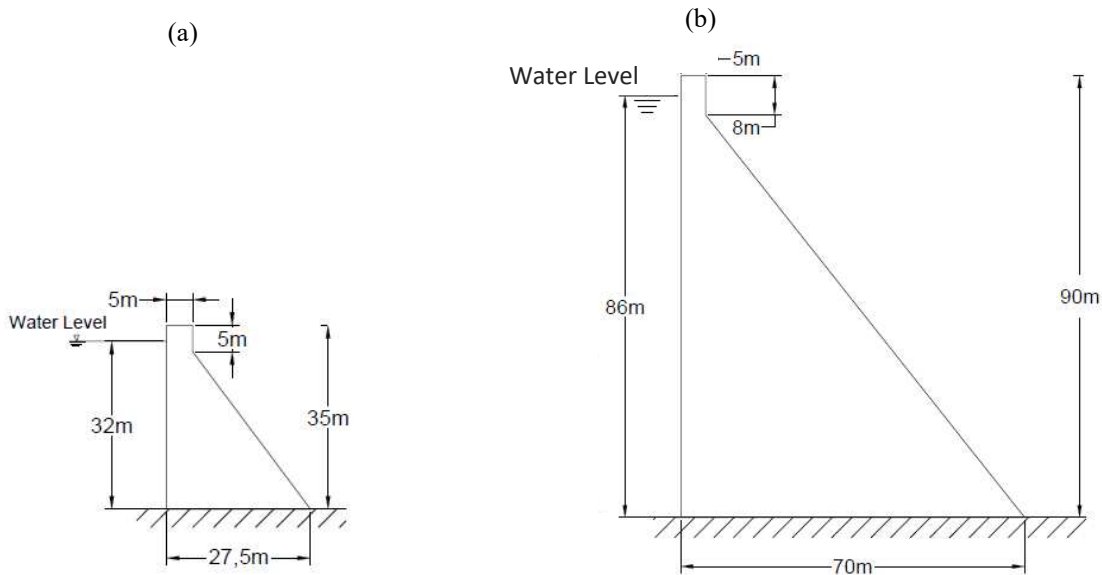


Figure 3.1 Cross sections for dam: (a) D1; (b) D2

3.2 Finite element analysis method

In this study, D1 and D2 were subjected to gravity, hydraulic, and seismic loads. Their behaviours were modelled using the method of continuum, plane strain element, 4-node bilinear, reduced integration, abbreviated as CPE4R (Alsuleimanagha and Liang, 2012; Mazighi and Mihoubi, 2022; Sarkhel et al., 2020). In particular, for D1, the lead block and the subregion were simulated using mesh 12 (horizontal) x 10 (vertical) and 12 x 20 the subregion, respectively. For D2, they were 20 x 8 and 20 x 30, respectively. The element size in the subregion was approximately 2.3 m for D1 and 2.0 m for D2, which is comparable to the size used in the ABAQUS verification study on the Koyna dam, whose dimensions are similar to those of D2. Examples of FE meshes are shown in Fig. 3.2. There are 403 nodes and 360 elements for D1, and 819 nodes and 760 elements for D2.

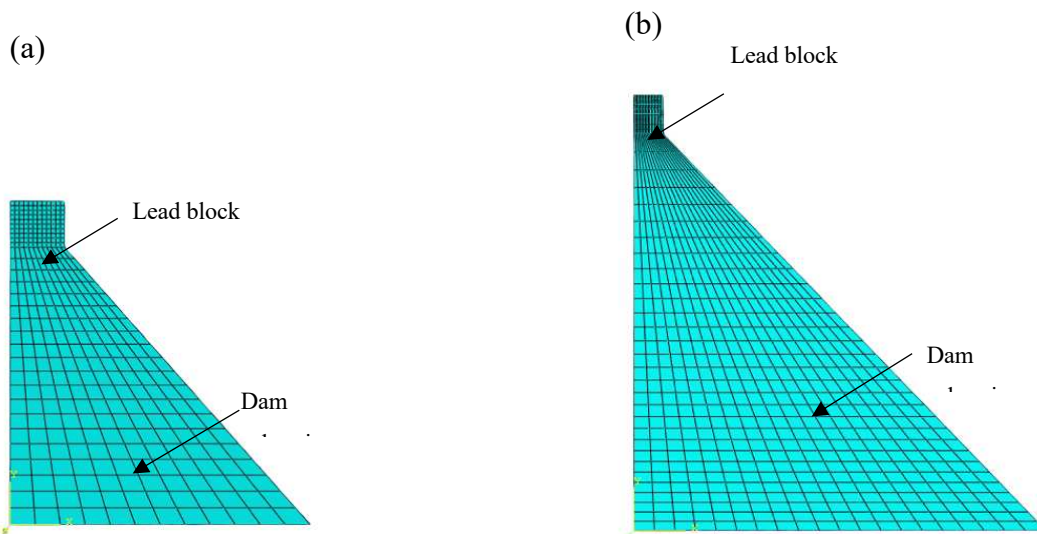


Figure 3.2 Cross-section, showing the finite element mesh used for FE computations: (a) D1; (b) D2

3.2.1 Compressive stress-strain curve

The compressive stress-strain curve was used to define the material behaviour of concrete under compression. This study obtained the curve by modifying the Hognestad model (Hognestad, 1912). This curve displayed two regions: an ascending parabolic branch when concrete reaches its

ultimate strength σ_{cu} , followed by the descending linear branch (Fig. 3.3). Concrete is considered to be crushed when the ultimate compress strain ϵ_{cu} of 0.0035 is reached, as stipulated in the Canadian Standards Association (2019). A typical value for strain at peak stress is $\epsilon_0 = 0.002$. From the computed compressive stress σ_c , the curve in Fig. 3.3 permits the determination of concrete damage like cracking in the dam.

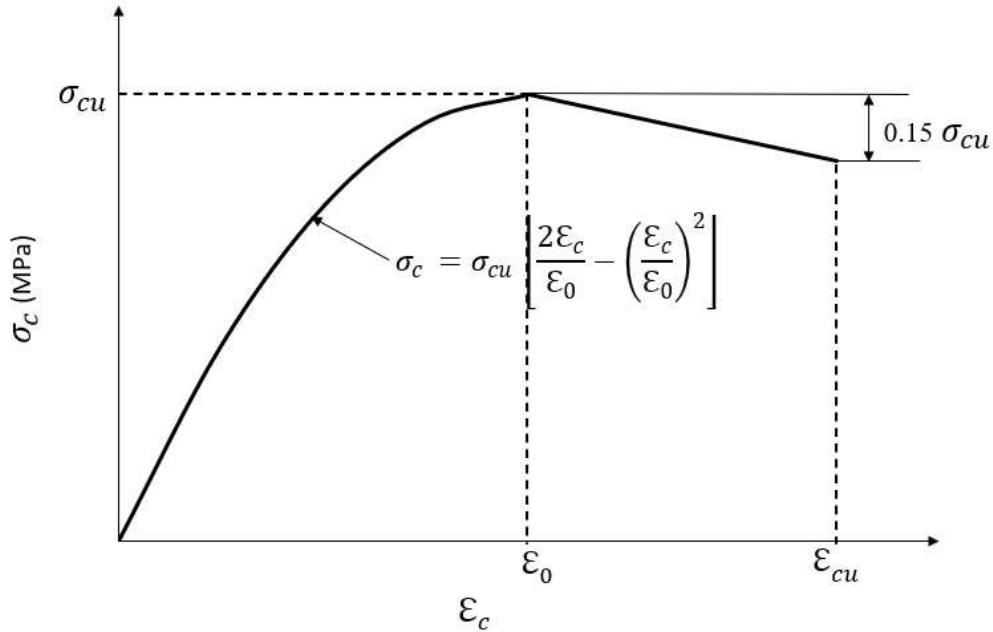


Figure 3.3 Stress-strain curve for concrete under compression.

Canadian Standards Association (2019) does not provide a stress-strain curve of concrete under tension. This study followed the European Committee for Standardization (2004) for the curve (Fig. 3.4), where the cracking strain (ϵ_{cr}) represents the onset of micro-crack formation in concrete.

The corresponding cracking stress, σ_{t0} , was obtained from CSA A23.3-19, given by

$$\sigma_{t0} = 0.6\sqrt{\sigma_{cu}} \quad (1)$$

When concrete is in the elastic stage, the relation between σ_{t0} and ϵ_{cr} follows Hook's Law. Once the strain in the concrete exceeds ϵ_{cr} , its strength starts to decrease to enter so-called concrete soften zone, with the stress to be 77% of the initial stress σ_{t0} . Then the stress decreases progressively with increasing strain due to crack propagation. At four times the cracking strain

ϵ_{cr} , the tensile stress drops to 45% of σ_{t0} and at a strain level of 8.7 times ϵ_{cr} , the residual tensile stress reduces to 10% σ_{t0} . The curve in Fig. 3.4 determined concrete damage from the computed tensile stress σ_t ,

3.2.2 Cracking and failure of concrete

Since concrete has extremely low tensile strength (which is about 10% of its compressive strength), it is susceptible to structural cracking. For quantifying the effect of cracking on the overall performance of concrete structures, ABAQUS provides several constitutive models to simulate the cracking behavior of concrete, such as smeared crack model, brittle cracking model, and concrete damaged plasticity model. The smeared crack model distributes cracking as strain softening across elements but is prone to mesh sensitivity and cannot capture cyclic behavior. The brittle cracking model initiates cracks once tensile strength is exceeded but neglects compressive crushing and post-cracking stiffness degradation, limiting its applicability for seismic assessment.

In contrast, the CDP model combines plasticity theory with continuum damage mechanics, allowing the simultaneous simulation of tensile cracking and compressive crushing. It introduces stiffness degradation through isotropic damage elasticity and incorporates both tensile and compressive plasticity, enabling realistic representation of crack initiation, propagation, and post-failure behavior (Lubliner et al., 1989; Lee & Fenves, 1998; Chen et al., 2019; Lei et al., 2023). For these reasons, the CDP model was adopted in this study to evaluate nonlinear seismic response and progressive damage in gravity dams.

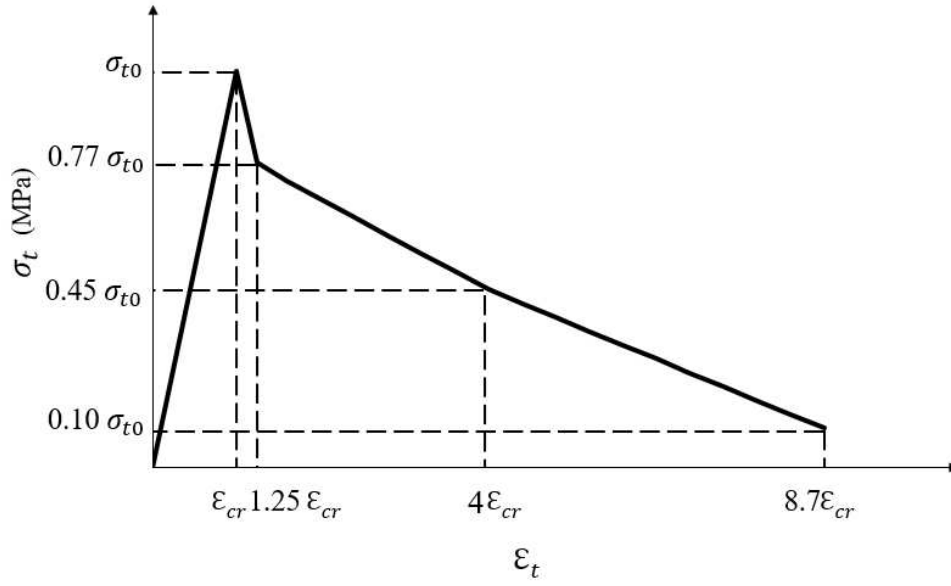


Figure 3.4 Stress-strain curve for concrete under tension.

The behaviour of concrete is characterised by linear elasticity followed by strain softening in tension (Fig. 3.5a) and stress hardening followed by strain softening in compression (Fig. 3.5b). For concrete under tension, the stress-strain response is elastic until the initial (i.e., maximum) tensile stress σ_{t0} is reached. The stress σ_{t0} corresponds to the onset of micro-cracking, which is a critical factor in assessing the tensile failure of concrete. Beyond σ_{t0} , micro-cracking occurs, leading to stiffness degradation which can be estimated by $(1 - d_t) E_0$. Similarly, under uniaxial compression, concrete exhibits a linear response up to the initial yield stress σ_{c0} . As the stress increases, the concrete enters a plastic regime where stress hardening occurs until it reaches the ultimate stress σ_{cu} , after which strain softening begins due to crushing failure mechanisms.

The concrete stress-strain relationships under tension and compression are expressed as:

$$\sigma_t = (1 - d_t)E_o(\epsilon_t - \epsilon_t^{pl}) \quad (2)$$

$$\sigma_c = (1 - d_c)E_o(\epsilon_c - \epsilon_c^{pl}) \quad (3)$$

$$\epsilon_t^{pl} = \epsilon_t^{cr} - \frac{d_t}{1 - d_t} \frac{\sigma_t}{E_o} \quad (4)$$

$$\varepsilon_c^{pl} = \varepsilon_c^{in} - \frac{d_c}{1 - d_c} \frac{\sigma_c}{E_0} \quad (5)$$

where σ_t is the tensile stress (MPa); d_t is the tensile damage variable (ranging between 0 and 1); E_0 is the initial undamaged elastic modulus (N/m); ε_t is the total tensile strain; ε_t^{pl} is the plastic strain in tension to represent cracking of the concrete; σ_c is the compressive stress (MPa); d_c is the compressive damage variable; ε_c is the total compressive strain; ε_c^{pl} is the plastic strain in compression to represent crushing of the concrete. The material properties used in this study are given in Table 3.1.

Table 3.1 Key parameters of concrete used in ABAQUS computation.

| Parameter | Symbol | Value | Unit |
|---|---------------|-------|-------------------|
| Concrete compressive ultimate stress | σ_{cu} | 25 | MPa |
| Concrete initial yield compressive stress | σ_{c0} | 11 | MPa |
| Concrete initial tensile stress | σ_{t0} | 3 | MPa |
| Concrete mass density | ρ | 240 | kg/m ³ |
| Young's modulus | E | 25000 | MPa |
| Poisson's ratio | ν | 0.15 | |

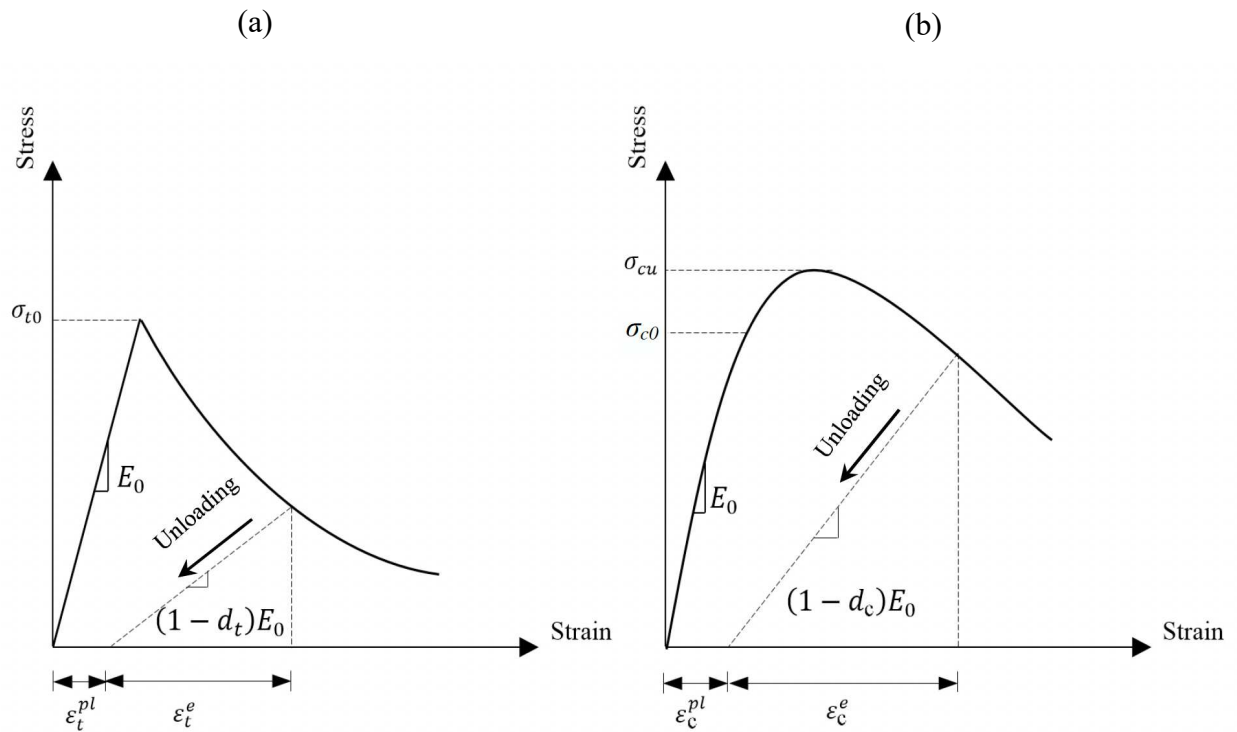


Figure 3.5 Response of concrete to uniaxial loading: (a) tension, (b) compression adapted from ABAQUS.

Concrete gravity dams differ from conventional reinforced concrete buildings. While reinforcement is present in certain components such as spillway piers, gates, galleries, and sometimes in contraction joints, the main dam body is typically constructed with very low reinforcement ratios. The global seismic performance of a gravity dam is therefore governed primarily by the nonlinear behavior of the mass concrete rather than by reinforcement. Several benchmark studies, including those on the Koyna Dam (Chopra & Chakrabarti, 1973; Pekau et al., 1995) and Canadian case studies (Duan et al., 2019), have modeled the dam body as plain concrete without embedded reinforcement, focusing on tensile cracking and compressive crushing as the dominant damage modes. In line with these practices, reinforcement was not explicitly modeled in the present study. Instead, the Concrete Damaged Plasticity (CDP) model was adopted to capture the essential nonlinear concrete behavior under seismic loading, including crack initiation, propagation, and progressive stiffness degradation.

3.2.3 Tensile and compressive damage

This study implemented nonlinear concrete modeling and quantified the degradation of stiffness due to micro-cracking in tension and crushing in compression, using two scalar damage parameters: 1) tensile damage, d_t , and 2) compressive damage, d_c , in order to track the material deterioration under loading. The values of d_t and d_c ranged from zero (undamaged) to one (complete loss of load-carrying capacity). These two damage parameters were essential for simulating the progressive failure of concrete under seismic and cyclic loads. They depend on plastic strain, temperature, θ , and other potential field-dependent variable, f_i , i.e., $d_t = d_t(\varepsilon_t^{pl}, \theta, f_i)$ and $d_c = d_c(\varepsilon_c^{pl}, \theta, f_i)$. In this study, they are expressed as

$$d_t = 1 - \frac{\sigma_t}{\sigma_{t0}} \quad (6)$$

$$d_c = 1 - \frac{\sigma_c}{\sigma_{cu}} \quad (7)$$

Values of σ_{t0} and σ_{cu} are listed in Table 3.1. Note that σ_t and σ_c are given in Eqs. 2 and 3, respectively. For illustration, Figure 3.6 present the tensile damage parameter d_t vs the cracking strain ε_t^{cr} .

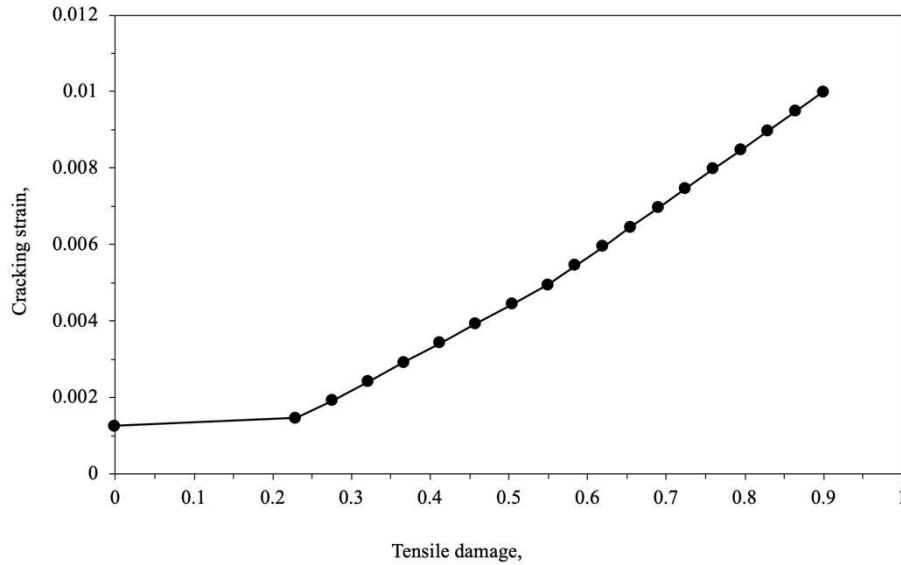


Figure 3.6 Tensile damage parameter d_t vs cracking strain ε_t^{cr} .

3.3 Loading on dam

Gravity, hydrostatic, and earthquake loads were applied on the dams. The gravity load due to dam's self-weight was modelled as a body force acting throughout the dam's volume. The gravity load per unit volume is given by

$$\mathbf{f}_g = \rho \mathbf{g} \quad (8)$$

where g is the acceleration due to gravity, taken as 9.81 m/s^2 . This load in the vertical direction contributes significantly to the internal stress distribution and is critical for evaluating sliding, overturning, and overall stability under both static and dynamic conditions. Modeling the self-weight as a body force ensures a realistic simulation of the dam's behavior, in accordance with established practices (Lupoi and Callari, 2012; Bernier et al., 2016).

The hydrostatic load associated with the hydrostatic pressure, p , is exerted by water in the reservoir on the upstream face of the dam (Fig. 3.1), calculated as

$$p = \rho_w g h \quad (9)$$

where ρ_w is the density of water (1000 kg/m^3); h is the depth of water measured from the bottom of the dam (see Fig. 3.1 (in m)). p increases linearly with h and reaches the maximum at the base of the dam. The pressure distribution was imposed as the boundary condition along the upstream face, aligning with standard practices in seismic performance assessments of gravity dams as in previous studies (Lupoi and Callari, 2012; Bernier et al., 2016).

The earthquake load or seismic force, f_s , plays a critical role in the assessment of the stability and safety of a gravity dam. This study investigated the seismic behaviours of D1 and D2 using acceleration records from the 1988 Saguenay Earthquake, which was one of the most significant seismic events recorded in eastern Canada. The earthquake occurred on November 25, 1988, with a 5.9 moment magnitude, at approximately 35 km south of Chicoutimi, Quebec. This study used a total of 22 acceleration time-history records, collected from different recording stations across Quebec. The records included both longitudinal and transverse components. This study applied the two components independently to the dam models to observe directional effects.

The seismic force f_s (N) acting on mass m can be computed using Newton's second law

$$f_s = m \ddot{u}_g(t) \quad (10)$$

where $u_g(t)$ is the time-dependent ground displacement (m) from the seismic records; a dot placed above a variable represents the derivative of that variable with respect to time. The applied time

history of acceleration \ddot{u}_g reflected earthquake conditions, allowing for an accurate assessment of dynamic response.

3.4 Motions of dam elements

In response to external time-varying loads, the displacement vector, $u(t)$, for individual FE nodes (Fig. 3.2) was computed using the dynamic equation in finite element form

$$M\ddot{u}(t) + C\dot{u}(t) + Ku(t) = -M\ddot{u}_g(t) \quad (11)$$

where M is a mass matrix (kg) consisting of the elements; C is the corresponding damping matrix (N·s/m); K is the corresponding stiffness matrix (N/m). In Eq. 11, three primary forces acting on the dam: 1) inertial force $M\ddot{u}(t)$ represents the resistance due to mass acceleration; 2) damping force $C\dot{u}(t)$ accounts for energy dissipation due to material and structural damping; 3) the stiffness force $Ku(t)$ represents elastic restoring forces due to structural rigidity. The seismic loading was applied through acceleration $\ddot{u}_g(t)$ at the nodes at the base of the dam.

The procedures for numerical computations consisted of several steps:

- 1) Define the mass matrix of the dam.
- 2) Input the damping characteristics based on Rayleigh damping, given by

$$C = \alpha M + \beta K \quad (12)$$

where α and β are Rayleigh damping coefficients, respectively.

- 3) Assign earthquake acceleration at the dam base.
- 4) Solve Eq. (11) using an implicit time integration (Chopra, 1995). The key output variables interested in this study are:

- Horizontal displacements at the nodes (Fig. 3.2), which measure the movement of the dam relative to the ground motion.
- Tensile stress and damage formulae for the calculation of the stress). The damage is calculated from Eq. 6, but the calculation needs the tensile stress as input.

The horizontal displacement at a given note in the dam can be calculated as

$$u_c(t) = u_d(t) - u_g(t) \quad (13)$$

where u_d is absolute displacement of the dam (in m) and u_g is the ground displacement (in m). An analysis of the above-mentioned output variables allows one to assess the structural integrity of

the dam under earthquake conditions and to make recommendations for design improvements and reinforcements if necessary.

3.5 Natural Frequency of Dam

The dynamic characteristics of the dam were determined by conducting a frequency extraction (Chopra, 1995). The first four natural frequencies (f_n) were calculated by using the eigenvalue problem

$$(K - \omega_i^2 M) \phi_i = 0 \quad (14)$$

where K accounts for the mass distribution of the structure; the term ω_i denotes the angular frequency (in rad/s) of the i 'th vibration mode; ϕ_i represents the eigenvector (mode shape) associated with that frequency. The natural frequency f_n in Hz was obtained using

$$f_n = \frac{\omega_i}{2\pi} \quad (15)$$

This analysis is crucial for understanding the dam's vibration behaviour under dynamic loads such as earthquakes. f_n is utilized to find Natural Period, T , of dams

$$T = \frac{1}{f_n} \quad (16)$$

Which later used for calculating elastic response spectral acceleration.(Bader & Clayton, 2022).

3.6 Scaling of Earthquake Records

In this study, we first conducted an analysis of the gravity dam using ABAQUS software, incorporating gravity load, hydrostatic load, and the original set of Saguenay earthquake records. This initial analysis provided a baseline understanding of the dam's response under seismic conditions.(ABAQUS, 2014) The earthquake records, sourced from multiple sites across Quebec, were then used to simulate the seismic loading on the dam and assess its structural performance under varying seismic excitations. Following this, we scaled these records to match the design spectrum at the fundamental period T_1 of the dam. The design spectrum for the dam site was developed in accordance with NBCC and Canadian Highway Bridge Design Code (CHBDC) for 5% damping, site class C (hard rock). This scaling allowed us to assess the dam's response under more severe seismic conditions and better understand its vulnerability to future earthquakes.

We used SeismoLEE software to generate the elastic response spectral acceleration from the original acceleration records. This software allowed for the precise calculation of the spectral acceleration for each seismic event, which was essential for understanding the dynamic response of the dam under varying earthquake excitations. The generated spectral acceleration data were then used to scale the earthquake excitation two times the design level, ensuring they aligned with the design spectral acceleration for the subsequent seismic analysis of the dam.

Chapter 4 : Results

4.1 Model Validation

To validate the modeling techniques described above for evaluating the two dams considered in this study, a case study was conducted on the Koyna Dam (Fig. 4.1) which sustained magnitude 6.5 earthquake that occurred on December 11, 1967. Ground accelerations recorded at the site during the event were 0.49 g in the stream direction, 0.63 g in the cross-stream direction, and 0.34 g vertically. The most notable structural damage consisted of horizontal cracks appearing on both the

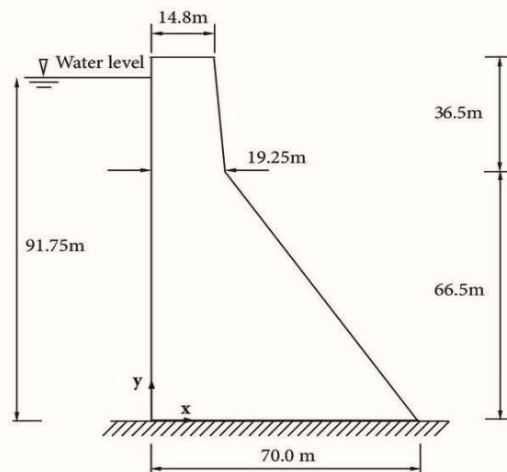


Figure 4.1 Cross-section of the Koyna Dam showing dimensions (Pekau and Feng 1995).

upstream and downstream faces. Pekau and Feng (1995) developed a new procedure for evaluation of the fracture of concrete gravity dams during strong earthquakes. The results of their numerical analysis were compared with experiments conducted at the University of California, Berkeley. Figure 4.2 (a) shows the 1:500 scale model constructed from plaster, while Figure 4.2 (b) illustrates the finite element model used by Pekau and Feng (1995). It is worth noting that the developers of ABAQUS also conducted a sensitivity analysis on the Koyna Dam to test their software. The input data used for this analysis was made publicly available online(<https://classes.engineering.wustl.edu/2009/spring/mase5513/abaqus/docs/v6.6/books/exa/default.htm?startat=ch02s01aex67.html>). Table 4.1 summarizes the concrete properties used in the analysis of the Koyna Dam.

(a)



(b)

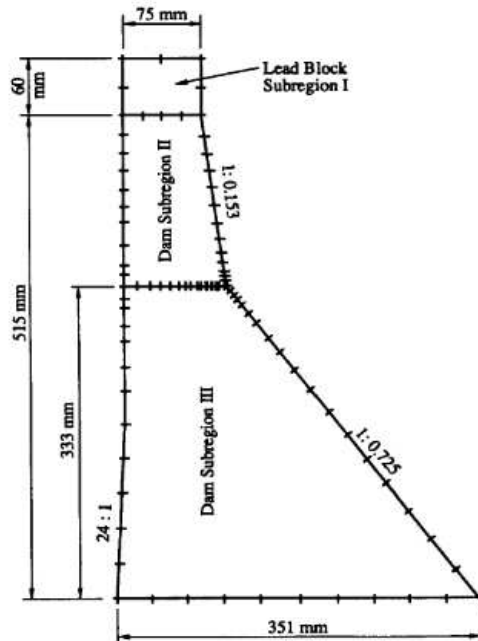


Figure 4.2 (a) Scaled laboratory model of the Koyna Dam; (b) cross section of the scaled laboratory model dam, showing boundary element discretization used for numerical computation in Pekau and Feng (1995).

Table 4.1 Key parameters of concrete used in ABAQUS computation of the Koyna Dam in this study.

| Parameters | Symbol | Values | Unit |
|---|---------------|--------|-------------------|
| Concrete compressive ultimate stress | σ_{cu} | 25 | MPa |
| Concrete initial yield compressive stress | σ_{c0} | 13 | MPa |
| Concrete tensile stress | σ_{t0} | 3 | MPa |
| Concrete mass density | ρ | 2400 | Kg/m ³ |
| Young's modulus | E | 31027 | MPa |
| Poisson's ratio | ν | 0.15 | |

4.1.1 Natural frequency of Koyna Dam

The first step in the validation process involved conducting a modal analysis to compare the natural frequencies of the Koyna Dam obtained in this study with those reported in the literature. The results, summarized in Table 4.2, show good agreement between the present study and the reference studies by Chopra and Chakrabarti (1973) and Pekau and Feng (1995). It can be seen in the table that the frequencies from this study are almost the same as provided in the ABAQUS online source. The maximum deviation is approximately 5.26% for Mode 4 compared to Pekau and Feng's results, while the differences with Chopra and Chakrabarti's data remain under 3%. This small discrepancy indicates that the mass and stiffness of the Koyna Dam were accurately modeled.

Table 4.2 Natural frequencies of the Koyna Dam.

| Mode number | Chopra & Chakrabarti (1973) | Pekau et al. (1995) | ABAQUS open-source | Present Study |
|-------------|-----------------------------|---------------------|--------------------|---------------|
| 1 | 19.27 | 19.28 | 18.86 | 18.86 |
| 2 | 51.50 | 50.13 | 49.97 | 50.00 |
| 3 | 67.56 | 70.43 | 68.16 | 68.134 |
| 4 | 99.73 | 103.79 | 98.27 | 98.331 |

4.1.2 Seismic analysis

Seismic analysis of the Koyna Dam was conducted using the acceleration time history recorded in the stream direction during the earthquake event (Figure 4.3). The ground motion excitation was applied at the dam's base, which was assumed to be fully fixed. A damping ratio of 3% was adopted for the first mode, and Rayleigh stiffness was assumed to be proportional to damping. It is important to note that static analysis on the dam due to gravity and hydraulic loads was completed prior to the application of the seismic load.

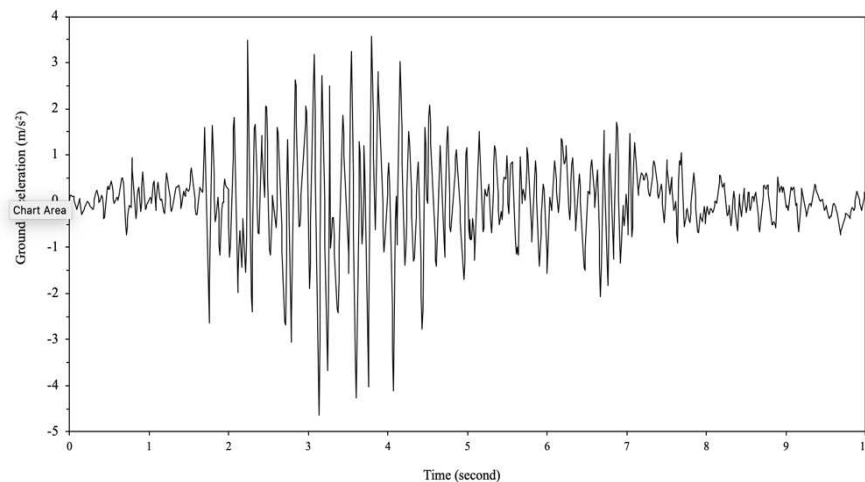


Figure 4.3 Time series of the transverse acceleration recorded during the 1967 earthquake.

4.1.2.1 Results of displacement time history

The displacement time history at the dam crest obtained in this study (Figure 4.4) was compared with the corresponding result available from the ABAQUS open-source webpage, which serves as the sole reference for such a comparison. It is important to note that, due to the unavailability of the original ABAQUS time history data, the result presented in Fig. 4.4 is based on data extracted from an image of the displacement time history published online and subsequently converted to Excel. While this procedure allowed for a clearer and higher-quality overlay of the two results, the digitization process may introduce minor discrepancies in amplitude and time alignment. These small differences, visible in Figure 4.4, are therefore attributed to the limitations of curve tracing rather than inherent modeling inaccuracies. The negative displacement in Fig. 4.4 indicates the displacement in the dam upstream direction. However, the comparison of the first five

displacement peaks seems reasonable as provided in Table 4.3. In particular, the maximum displacement from present study (39.53 mm) is compatible with the maximum of 40.83 mm from ABAQUS open source.

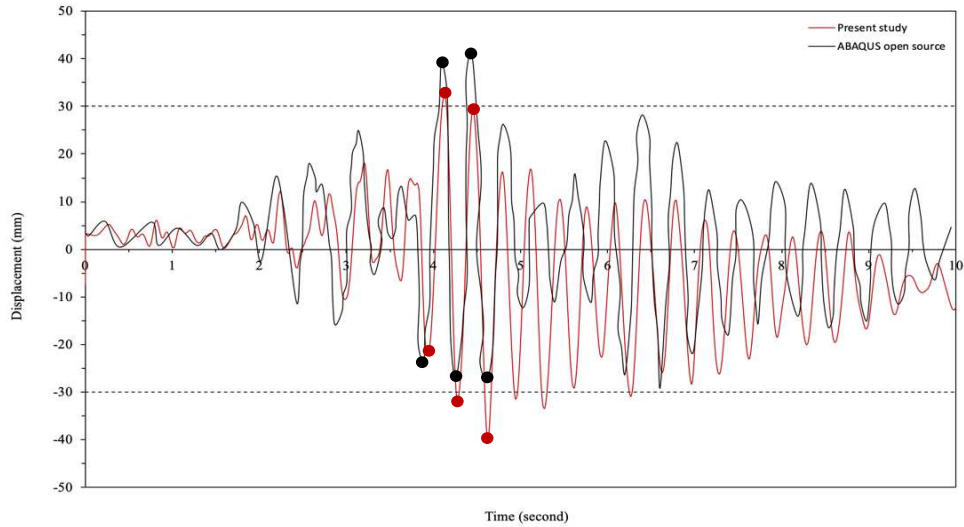


Figure 4.4 Comparison of horizontal crest displacement $u_c(t)$ between this study and ABAQUS (2009).

Table 4.3 Comparison of displacement peaks with respective time.

| ABAQUS Open Source | | Present Study | |
|--------------------|-------------------|---------------|-------------------|
| Time step (s) | Displacement (mm) | Time step (s) | Displacement (mm) |
| 3.90 | -24.05 | 3.93 | -22.17 |
| 4.26 | -19.30 | 4.28 | -31.80 |
| 4.62 | -27.31 | 4.62 | -39.53 |
| 4.10 | 39.38 | 4.13 | 32.33 |
| 4.45 | 40.83 | 4.44 | 26.78 |

*Time step was adjusted from source

4.1.2.2 Results of damage to the dam

Figure 4.5 and Figure 4.6 illustrates the dam damage at the five-time steps corresponding to the displacement peaks listed in Table 4.3 and at the time $t = 10$ s, based on both the simulation conducted in this study and the ABAQUS open-source results. In general, the results match well except the present study was not able to predict the damage to the face of the dam on the upstream side. However, it should not be a concern given the damage is extremely small with d_i is about 0.25.

Based on the comparison of natural frequencies, displacement peaks, and damage results between the present study and those obtained using the ABAQUS open source, it can be concluded that the numerical modelling techniques exercised in this study are promising for providing reliable results.

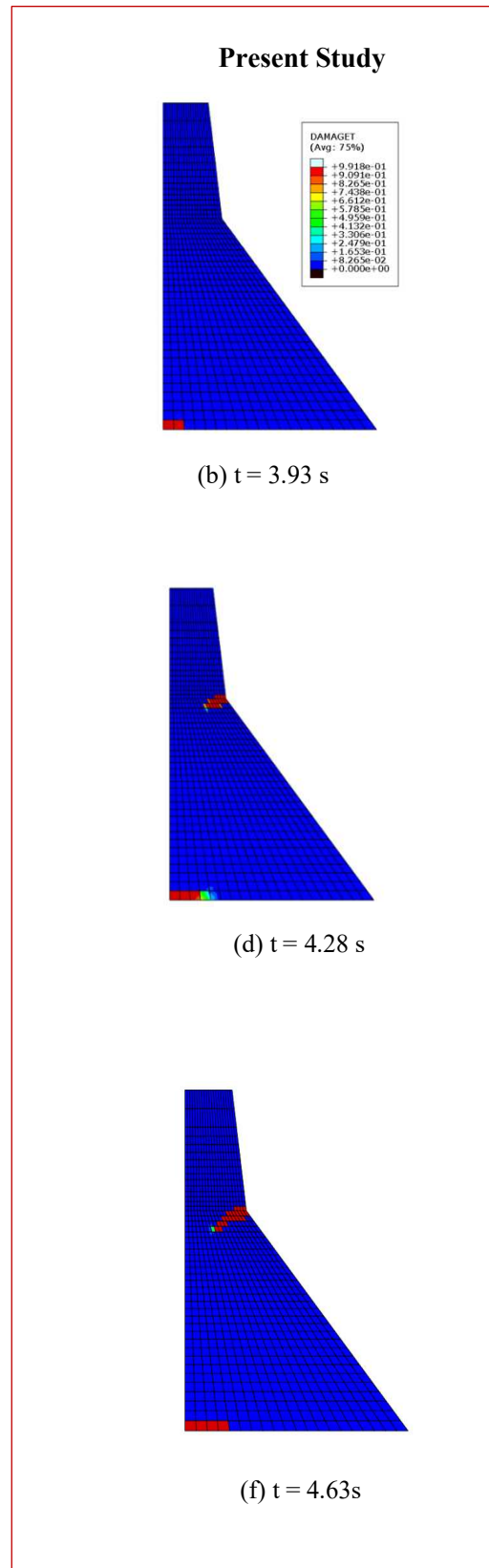
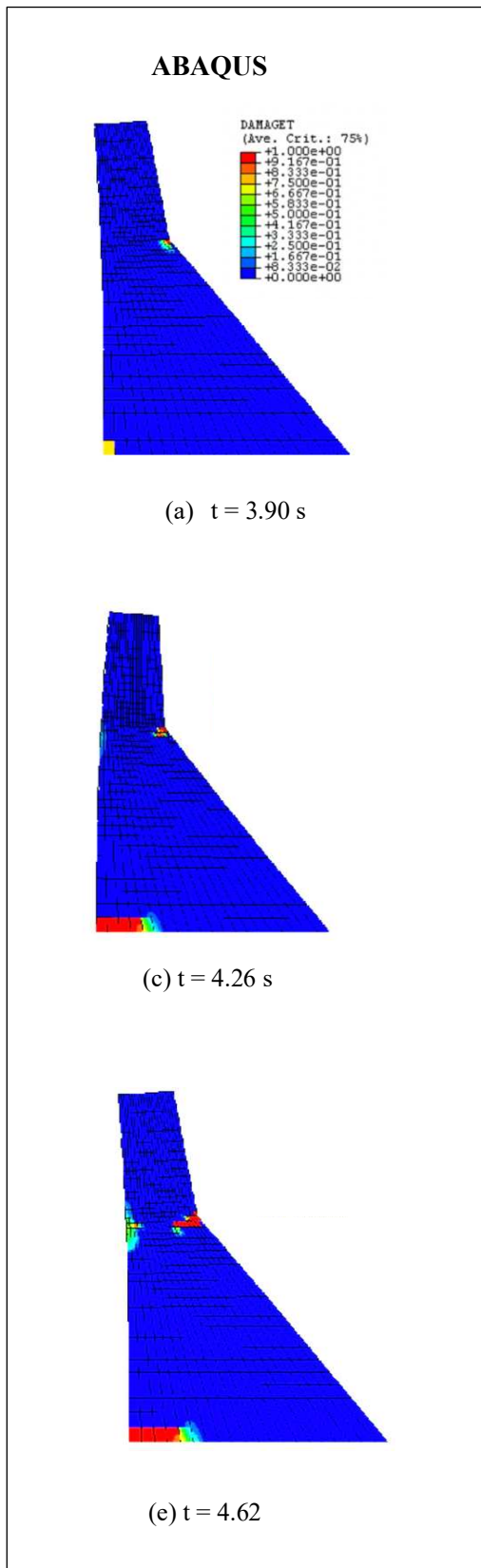


Figure 4.5 Comparison of tensile damage d_t results of Koyna Dam: (a) $t = 3.90$ s; (b) 3.93 s; (c) $t = 4.26$ s; (d) $t = 4.28$ s; (e) $t = 4.62$ s; (f) $t = 4.63$ s.

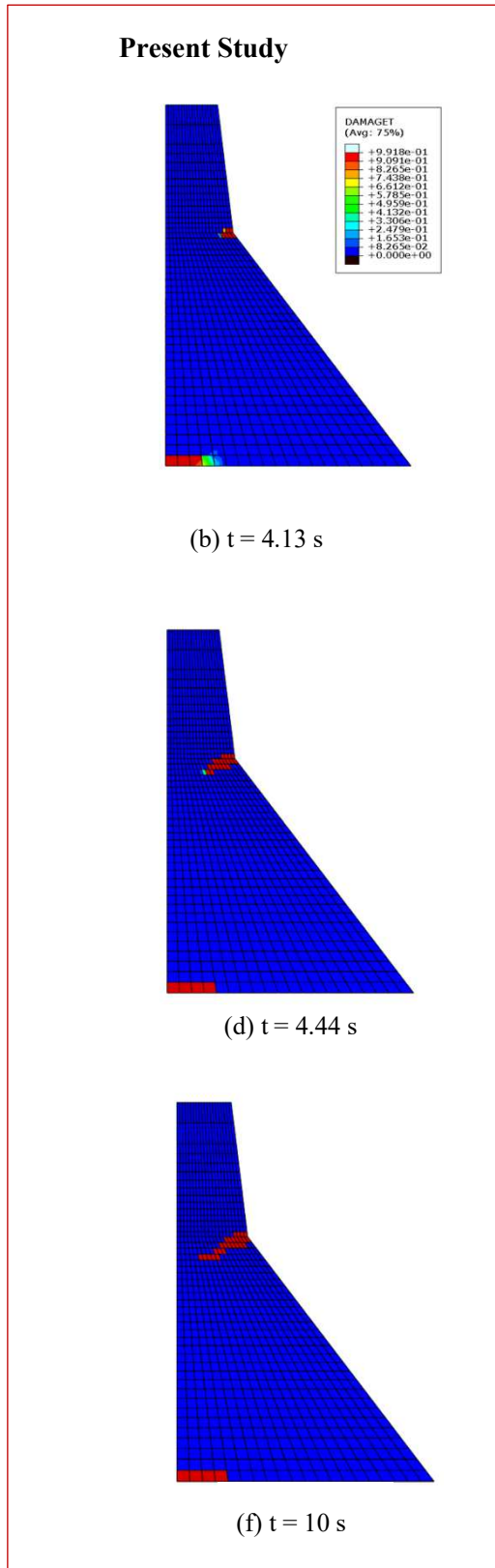
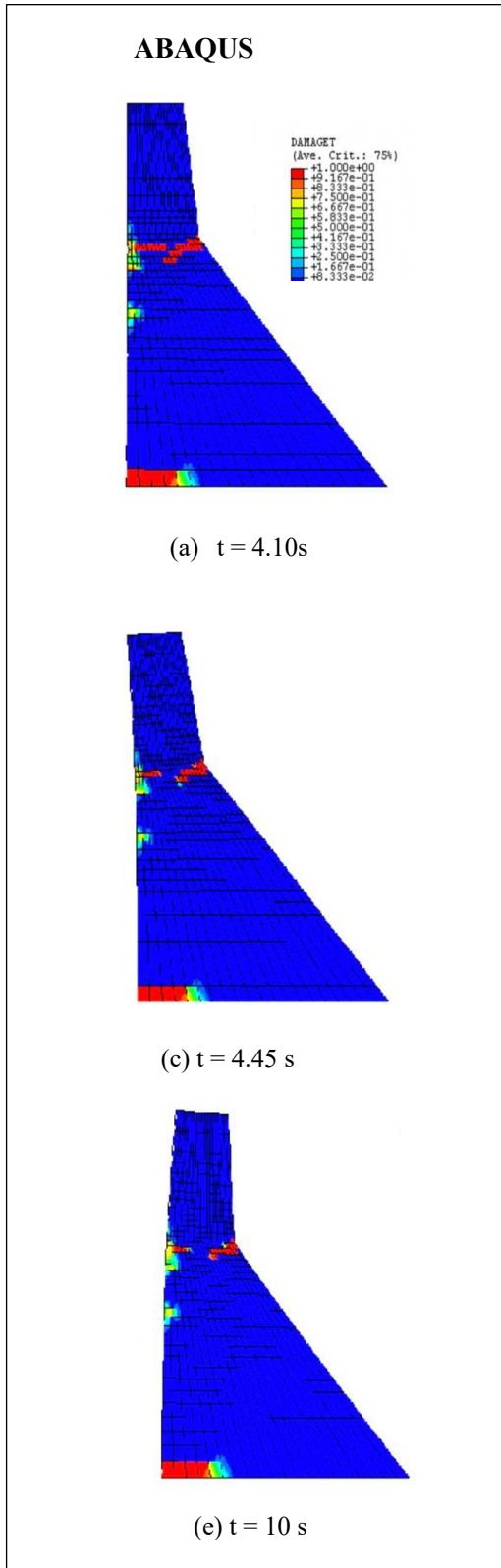


Figure 4.6 Comparison of tensile damage d_t results of Koyna Dam: (a) $t = 4.10\text{ s}$; (b) 4.13 s ; (c) $t = 4.25\text{ s}$; (d) $t = 4.44\text{ s}$; (e) $t = 10\text{ s}$; (f) $t = 10\text{ s}$.

4.2 Natural frequencies of D1 and D2

To assess the dynamic characteristics of the dams under seismic loading, a modal analysis was conducted for both Dam D1 (Montreal) and Dam D2 (La Malbaie) using modal extraction in Abaqus. The first four natural frequencies were obtained, as presented in Table 4.4. These results indicate that Dam D1, being more compact and structurally stiffer, exhibits significantly higher natural frequencies than Dam D2. The first mode for Dam D1 is approximately 2.3 times higher than that of Dam D2, suggesting a much stiffer response to dynamic excitation.

Table 4.4 Natural frequencies of Dam D1 and D2

| MODE | Natural frequency (rad sec ⁻¹) | |
|------|--|---------|
| | Dam D1 | Dam D2 |
| 1 | 68.453 | 29.699 |
| 2 | 161.504 | 63.521 |
| 3 | 192.517 | 80.629 |
| 4 | 234.720 | 103.481 |

In both dams, the fundamental mode shape primarily involved horizontal displacement concentrated near the crest, which is typical for gravity dams. The higher modes showed more complex vibration patterns with nodal points along the dam height.(Chopra , 1995). Understanding these natural frequencies is critical in seismic analysis since they indicate the potential for resonance with ground motion frequencies. Given that Dam D2 has lower frequency values, it may be more susceptible to resonance effects when subjected to long-period ground motions, potentially leading to greater structural response under certain seismic scenarios. These frequency results were later used to guide the scaling of earthquake records and interpret the displacement and damage response under seismic loading, as discussed in the later sections

4.3 Earthquake Input Records: Overview and Identification

To assess the seismic response of the dams, 22 acceleration time history records from the 1988 Saguenay Earthquake were used each comprising longitudinal and transverse components recorded at 11 different locations across Quebec. These records, originally provided in unscaled form, were later scaled to simulate design-level earthquake intensity. The complete set of ground motions used in this study is summarized in Table 4.5. To maintain clarity throughout the result sections, each record has been assigned a simplified site code (e.g., Site 1L, 1T, 2L, etc.) where the number corresponds to the recording site, and the suffix L or T refers to the longitudinal or transverse component, respectively. These designations are used consistently in displacement and damage plots, figures, and result discussions that follow

Table 4.5 Saguenay earthquake records used in seismic simulations.

| Site Code | Record No. | Component | Recording Location | Record Length (s) |
|-----------|------------|--------------|--------------------|-------------------|
| Site 1L | 1 | Longitudinal | St-Ferreol, Quebec | 48.64 |
| Site 1T | 2 | Transverse | St-Ferreol, Quebec | 48.64 |
| Site 2L | 3 | Longitudinal | Quebec City | 39.04 |
| Site 2T | 4 | Transverse | Quebec City | 39.04 |
| Site 5L | 5 | Longitudinal | Tadoussac | 38.96 |
| Site 5T | 6 | Transverse | Tadoussac | 38.96 |
| Site 7L | 7 | Longitudinal | Baie-St-Paul | 17.74 |
| Site 7T | 8 | Transverse | Baie-St-Paul | 17.74 |
| Site 8L | 9 | Longitudinal | La Malbaie | 29.66 |
| Site 8T | 10 | Transverse | La Malbaie | 29.66 |
| Site 9L | 11 | Longitudinal | St-Pascal | 39.07 |
| Site 9T | 12 | Transverse | St-Pascal | 39.07 |

| Site Code | Record No. | Component | Recording Location | Record Length (s) |
|-----------|------------|--------------|--------------------|-------------------|
| Site 10L | 13 | Longitudinal | Riviere-Ouelle | 33.26 |
| Site 10T | 14 | Transverse | Riviere-Ouelle | 33.26 |
| Site 14L | 15 | Longitudinal | Ste-Lucie | 17.76 |
| Site 14T | 16 | Transverse | Ste-Lucie | 17.76 |
| Site 16L | 17 | Longitudinal | Chicoutimi-Nord | 33.99 |
| Site 16T | 18 | Transverse | Chicoutimi-Nord | 33.99 |
| Site 17L | 19 | Longitudinal | St-Andre | 28.35 |
| Site 17T | 20 | Transverse | St-Andre | 28.35 |
| Site 20L | 21 | Longitudinal | Les Eboulements | 20.65 |
| Site 20T | 22 | Transverse | Les Eboulements | 20.65 |

4.3.1 Ground motion spectral properties and scaling

To reflect the dynamic characteristics of the dams, all earthquake records were spectrally analyzed and scaled based on the fundamental period of each structure. The first-mode eigenfrequencies, obtained from Abaqus modal analysis, corresponded to 0.091 seconds for Dam D1 and 0.212 seconds for Dam D2. Using SeismoLEE software, Spectral Acceleration (Sa) and Spectral Velocity (Sv) were calculated for each record at these respective periods. Each ground motion was then scaled to produce a 5% damped spectral acceleration that matched the target Sa at the dam's fundamental period. This method, as proposed by Baker and Cornell (2006) and Shome et al. (1998), ensures that the seismic input aligns with the structure's natural frequency, thereby enabling more accurate evaluation of seismic demand and structural performance. The computed spectral parameters and their ratios (Sa/Sv) for both dams are summarized in Table 4.6

Table 4.6 Ground motion characteristics for Saguenay earthquake records.

| Rec. No. | Recording Site | Record Length(s) | Dam 1 | | | Dam 2 | | |
|----------|-----------------|------------------|-----------------------|---------|--------|-----------------------|---------|--------|
| | | | Sa(m/s ²) | Sv(m/s) | Sa/Sv | Sa(m/s ²) | Sv(m/s) | Sa/Sv |
| 1 | St-Ferreol | 48.64 | 1.8395 | 0.0205 | 9.129 | 0.3301 | 0.1017 | 3.245 |
| 2 | Quebec | 39.04 | 0.5457 | 0.0050 | 10.995 | 0.1568 | 0.0457 | 3.428 |
| 3 | Tadoussac | 38.96 | 0.8076 | 0.0100 | 8.224 | 0.0285 | 0.0003 | 79.242 |
| 4 | Baie-st-paul | 17.740 | 1.3141 | 1.3141 | 0.102 | 0.2471 | 0.0746 | 3.310 |
| 5 | La-Malbaie | 29.655 | 1.9040 | 1.9040 | 0.102 | 0.2987 | 0.0755 | 3.956 |
| 6 | St-Pascal | 39.065 | 0.6938 | 0.6938 | 0.102 | 0.1129 | 0.0291 | 3.880 |
| 7 | Riviere-Ouelle | 33.26 | 0.6803 | 0.0038 | 18.014 | 0.0998 | 0.0296 | 3.372 |
| 8 | Ste-Lucie | 17.755 | 0.1897 | 0.0021 | 8.830 | 0.0293 | 0.0080 | 3.646 |
| 9 | Chocoutimi-Nord | 33.995 | 3.2474 | 0.0351 | 9.426 | 0.19053 | 0.0662 | 2.876 |
| 10 | St-Andre | 28.35 | 4.2412 | 0.0586 | 7.374 | 0.15948 | 0.0527 | 3.022 |
| 11 | Les Eboulements | 20.65 | 1.9176 | 0.0232 | 8.418 | 0.2700 | 0.0823 | 3.280 |

4.4 Results of tensile damage

4.4.1 Dam D1 – Response to original acceleration records

The overall response of Dam D1 to these original Saguenay acceleration records was favorable, with the structure exhibiting high resilience and stability. Tensile damage was recorded in only a few cases record 7, 8, and 20. Even in these instances, the observed damage was minimal and spatially confined, typically occurring at the upstream heel.

In the simulation corresponding to Site 7 (Baie-St-Paul), For the transverse Acceleration at Site 7 (7L), the response was comparable in location but somewhat lower in damage magnitude. The maximum displacement reached 2.22 mm at 7.09 seconds (Fig. 4.7), indicating a sharper and earlier motion in the downstream direction. A small tensile damage developed (Fig. 4.8) even earlier, at 1.00 second, registering a peak damage value of 6.21×10^{-4} . While the displacement in

this case was greater than that of 7L, the damage remained smaller and more localized, suggesting that the direction and concentration of input energy significantly influence tensile failure development.

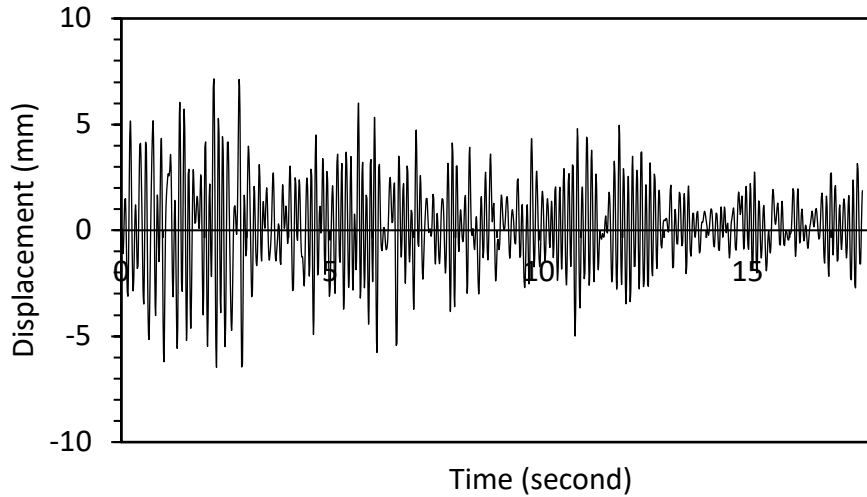


Figure 4.7 Graph showing horizontal crest displacement with time $u_c(t)$ for D1- site 7L.

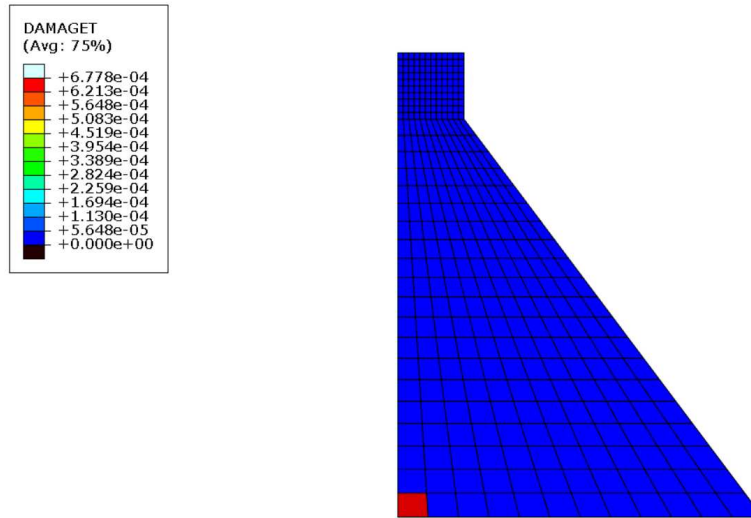


Figure 4.8 Contours of tensile damage d_t for D1 at time $t = 3$ s for site 7L.

The simulation for Site 8L produced the largest crest displacement recorded across all original ground motion cases, reaching 11.74 mm at 10.3 seconds (Fig. 4.9). Interestingly, tensile

damage initiated earlier, and the damage reached its peak before the point of maximum displacement (Fig. 4.10). The peak tensile damage value was 9.35×10^{-3} , confined to a small region at the upstream base corner, following the failure pattern observed in most Dam D1 simulations.

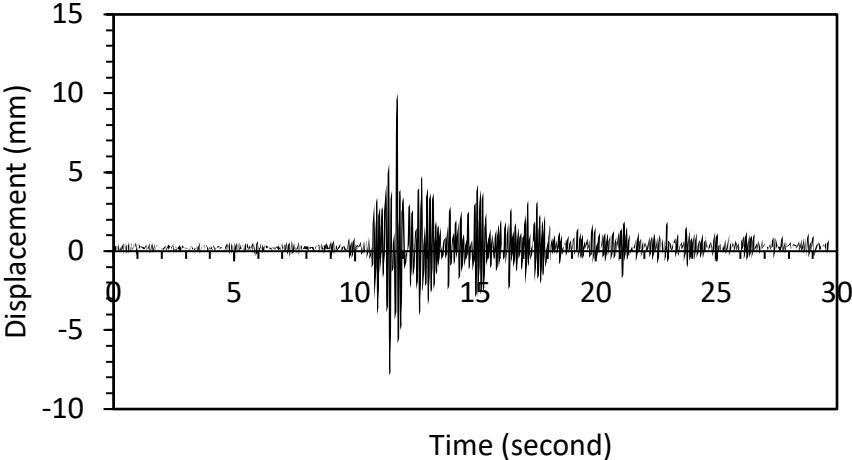


Figure 4.9 Graph showing horizontal crest displacement with time $u_c(t)$ for D1- site 8L.

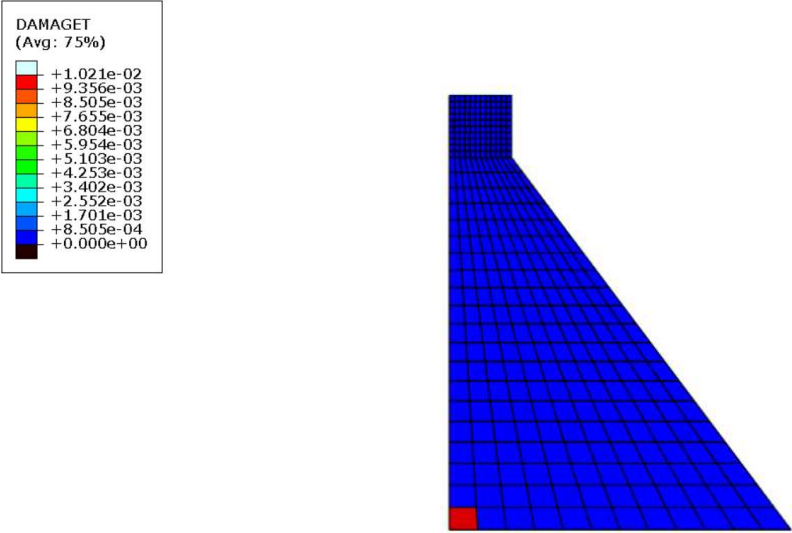


Figure 4.10 Contours of tensile damage d_t for D1 at time $t = 11.78$ s for site 8L.

This case is particularly significant because it highlights how prolonged and moderate-magnitude seismic excitation can result in progressive stress accumulation, even in the absence of strong or immediate peak accelerations. The delayed displacement maximum, relative to early tensile damage, suggests that material fatigue under repeated stress cycles played a dominant role in initiating failure.

Another instance of localized cracking was observed in the simulation for Site 20L, where the dam experienced a maximum crest displacement of -8.89 mm at 11.92 seconds (Fig. 4.11). A corresponding tensile damage initiated shortly after, peaking at 12.18 seconds with a maximum damage value of 3.09×10^{-3} (Fig. 4.12). The damage remained confined to a small region at the upstream heel, following the common failure pattern seen in other acceleration records. The temporal separation between displacement peak and damage peak underscores the effect of accumulated stress over time, wherein tensile failure may be induced not by a single impulse but by repeated or sustained motion crossing the material's threshold gradually.

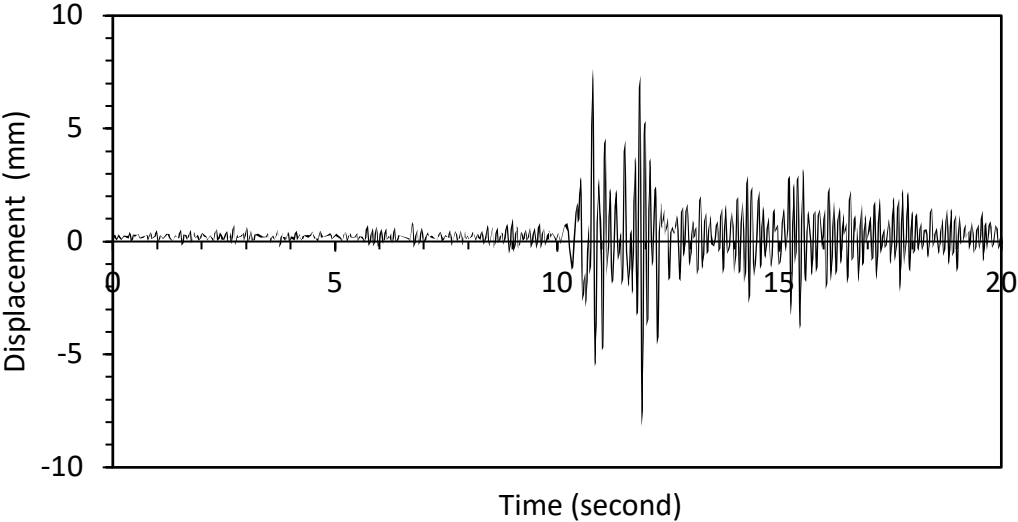


Figure 4.11 Graph showing horizontal crest displacement with time $u_c(t)$ for D1- site 20L.

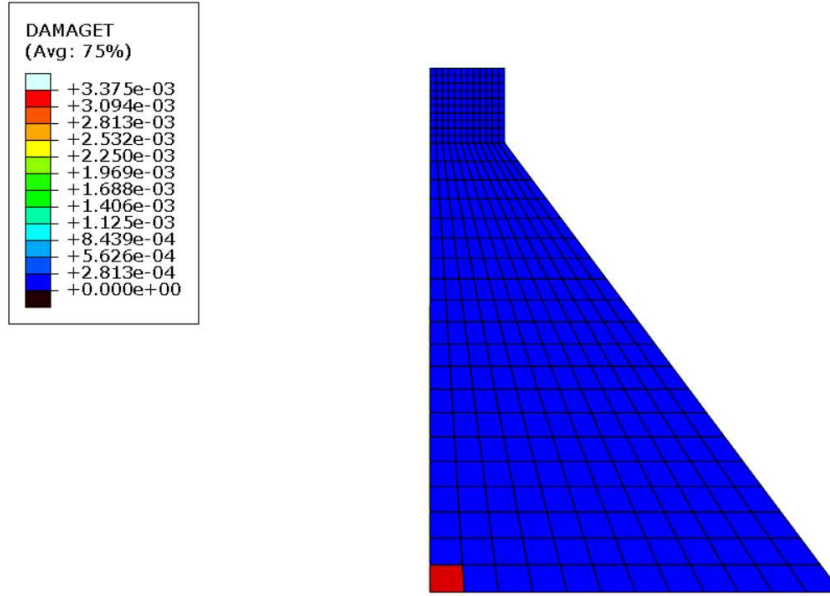


Figure 4.12 Contours of tensile damage d_t for D1 at time $t = 11.78$ s for site 20L.

Overall, these results confirm that Dam D1 maintained its integrity under the original, unscaled Saguenay earthquake records. Tensile damage was sparse, low in magnitude, and consistently restricted to critical base zones.

Displacement values across all simulations ranged from approximately 3 mm to 12 mm, with most peaks occurring within the first 3 to 12 seconds of ground motion. In many cases, damage initiation either coincided with or slightly lagged behind the displacement peaks, emphasizing the role of early, high-velocity ground motion phases in structural stress development. Figures associated with this section (Sites 7, 8, and 20 – both longitudinal and transverse) visually illustrate the recorded displacement responses and tensile damage contours.

4.4.2 Dam D1 – Response to scaled acceleration records

While Dam D1 exhibited strong performance under the original ground motions, its response under scaled acceleration records revealed more significant seismic vulnerability. The same 22 earthquake records from the 1988 Saguenay Earthquake, scaled using two design level, were applied to the dam to simulate a more intense seismic scenario. Under these amplified conditions, tensile damage became widespread across most simulations. Except for Record 16L

and 17L, nearly all ground motions resulted in visible tensile damage, with damage consistently concentrated at the upstream base corner and, in several cases, extending to the downstream wall near the crest. The most severe damages have discussed in this section.

The simulation for Site 1L showed a maximum crest displacement of -36.88 mm at 15.90 seconds (Fig. 4.13), indicating a strong dynamic response to the scaled longitudinal ground motion. Tensile damage emerged in two primary zones: at the upstream base corner (Fig. 4.14), where the peak damage reached 1.11×10^{-2} , and at the downstream wall below the crest level, where a secondary damage zone registered values up to 9.08×10^{-3} . Cracks were first observed at 11.96 seconds and intensified progressively, peaking by 16.15 seconds, following the acceleration pulse. The magnitude of tensile damage remained moderate; the emergence of multiple zones highlights the dam's structural sensitivity not only at its heel but also near the top under scaled seismic input.

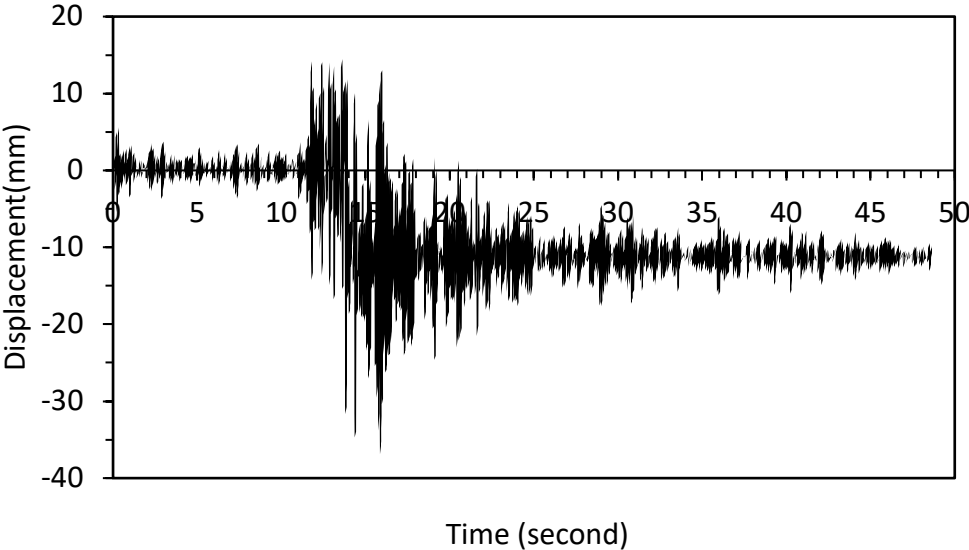


Figure 4.13 Graph showing horizontal crest displacement with time $u_c(t)$ for D1- scaled acceleration record site 1L

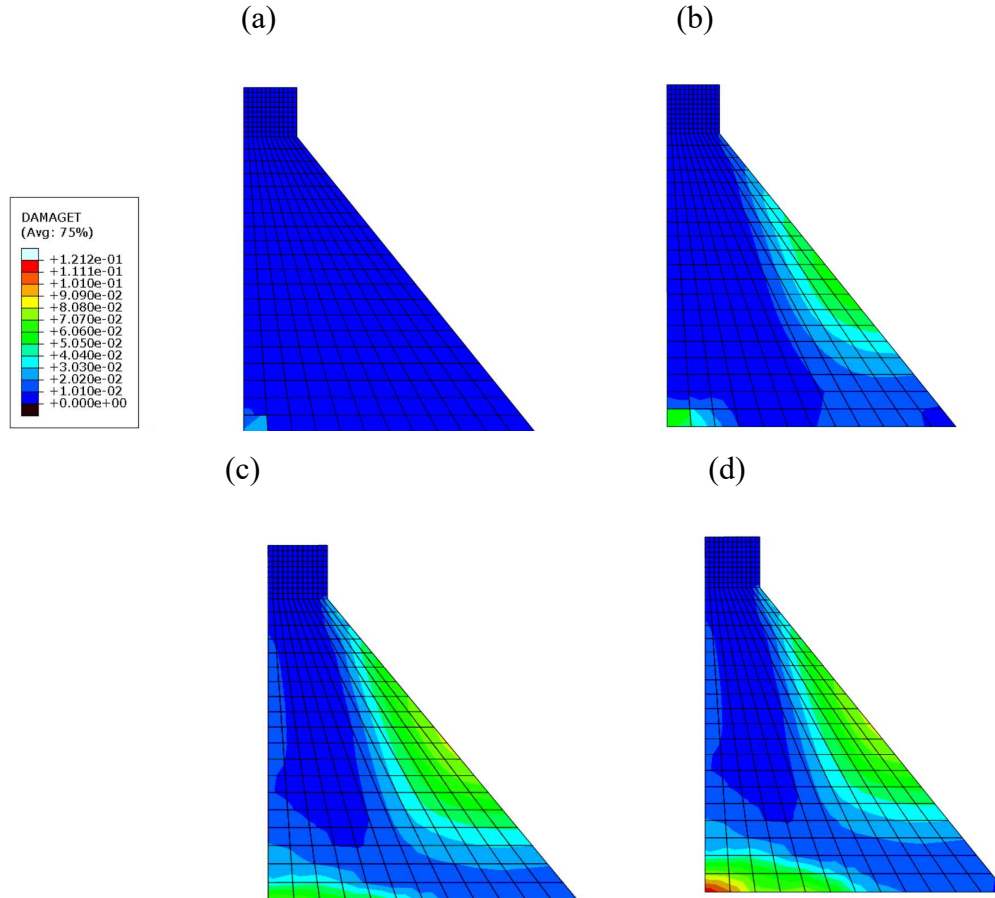


Figure 4.14 Contours of tensile damage d_t for D1 at time: (a) $t = 11.96$ s; (b) $t = 14.26$ s; (c) $t = 16.15$ s; (d) $t = 17.74$ s for scaled acceleration record of site 1L.

The simulation for Site 2L resulted in the highest recorded crest displacement across all scaled acceleration cases, peaking at 43.74 mm at 18.26 seconds (Fig. 4.15). This large deformation coincided with significant tensile damage at the upstream base (Fig. 4.16), where the maximum recorded damage value reached 4.84×10^{-1} . The tensile damage extended laterally through successive damage contours of 3.52×10^{-1} , 2.26×10^{-1} , and 8.80×10^{-2} , forming a wide and well-defined damage zone concentrated in the dam's heel region. Despite the intensity of the input and the extensive base cracking, tensile damage along the downstream wall remained minimal, suggesting that the dynamic force was predominantly transmitted and absorbed on the upstream face. This simulation highlights how high-intensity, longitudinal ground motion can lead to deep cracking near the base, where hydrostatic pressure and inertial forces converge.

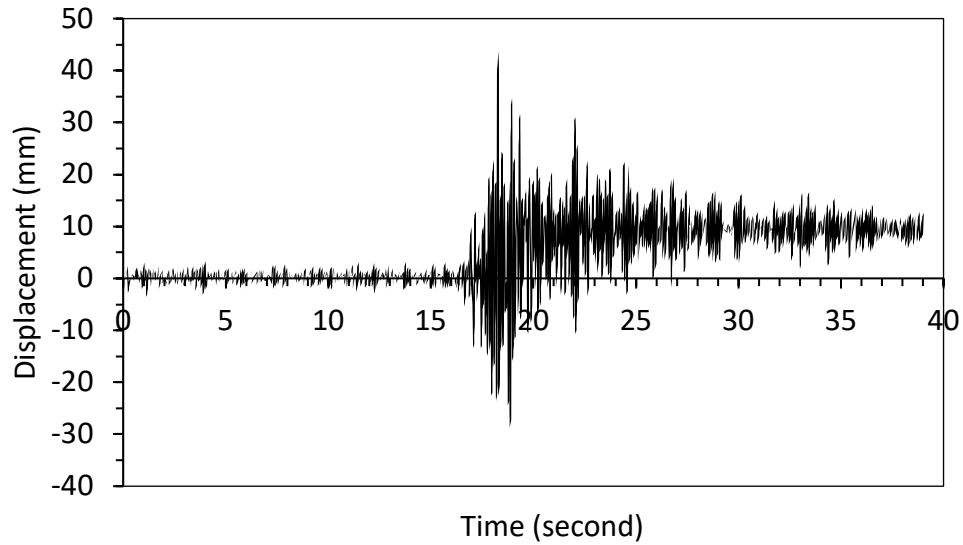


Figure 4.15 Graph showing horizontal crest displacement with time $u_c(t)$ for D1- scaled acceleration record site 2L

The simulation corresponding to Site 7L exhibited one of the most severe damage responses among all scaled ground motion records. The dam experienced a maximum displacement of -31.98 mm at 1.79 seconds (Fig. 4.17), with a rapid spike in crest deformation early in the seismic event. This abrupt motion was closely followed by extensive tensile cracking, which developed across more than half of the upstream base and continued into the downstream sloping wall (Fig. 4.18).

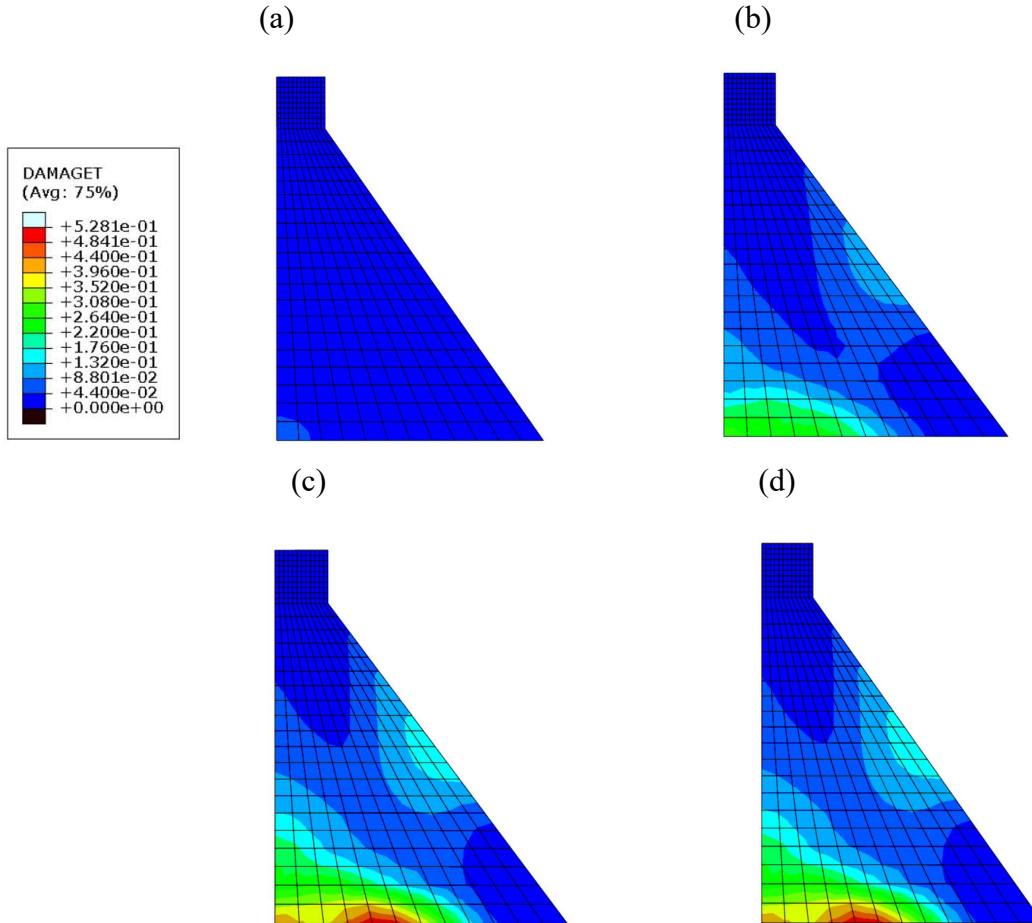


Figure 4.16 Contours of tensile damage d_t for D1 at time: (a) $t = 17.88$ s; (b) $t = 18.60$ s; (c) $t = 24.57$ s; (d) $t = 38.75$ s for scaled acceleration record of site 2L.

The peak tensile damage at the base reached 8.25×10^{-1} , indicating near-complete material degradation in that region. Damage propagation followed a broad arc, with subsequent contours measuring 6.77×10^{-2} and 5.41×10^{-2} , extending across the dam's lower third. On the downstream wall, the damage was also pronounced, with values of 5.25×10^{-1} and 4.06×10^{-1} . This simulation demonstrates the critical vulnerability of the dam under high-energy transverse excitations, where not only the base but also the downstream face can experience severe cracking.

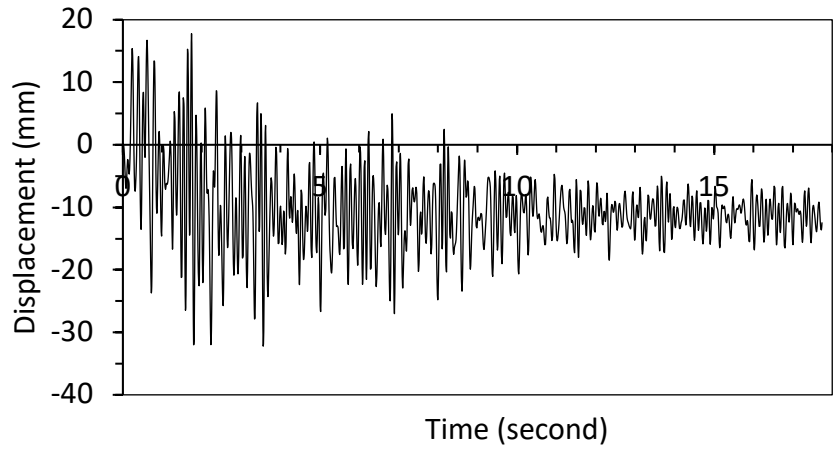


Figure 4.17 Graph showing horizontal crest displacement with time $u_c(t)$ for D1- scaled acceleration record site 7L.

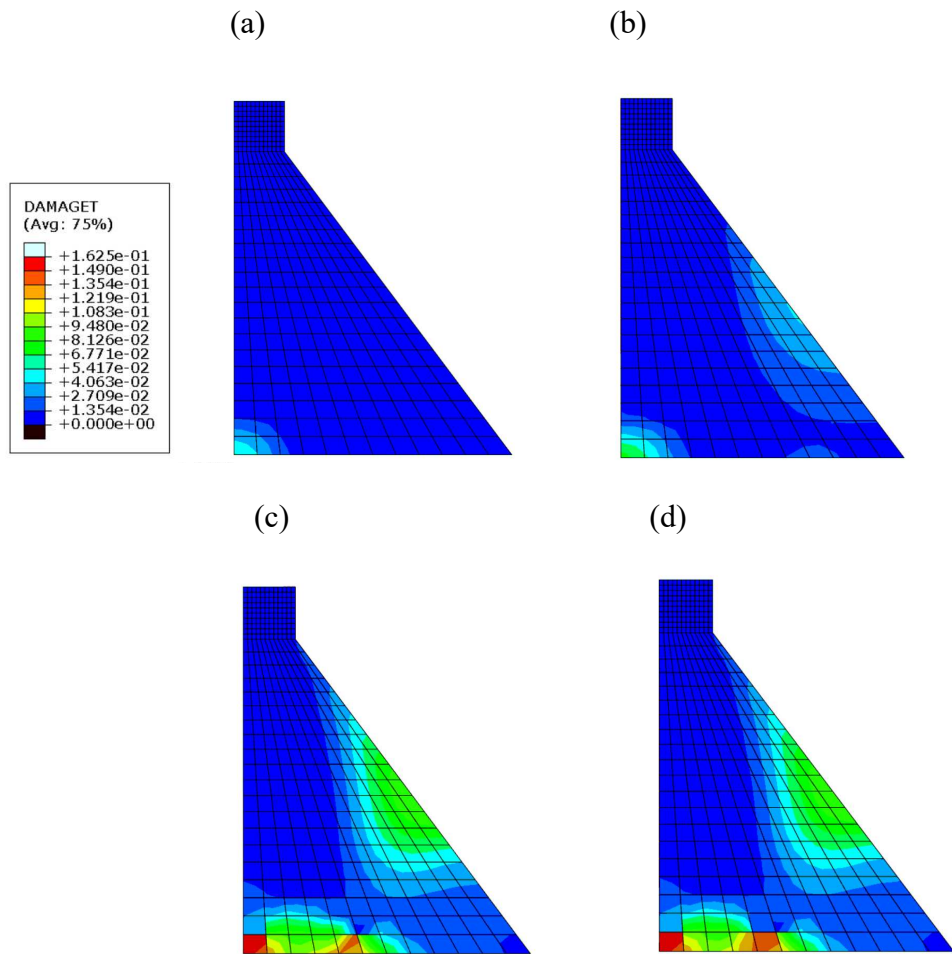


Figure 4.18 Contours of tensile damage d_t for D1 at time: (a) $t = 0.34$ s; (b) $t = 0.75$ s; (c) $t = 4.52$ s; (d) $t = 17.74$ s for scaled acceleration record of site 7L.

The simulation for Site 9L resulted in a maximum displacement of -25.59 mm at time 14.88 seconds (Fig. 4.19), recorded at the dam crest during a sharp and energetic shaking phase. This ground motion produced notable tensile damage at the upstream base corner (Fig. 4.20), with a peak value of 1.48×10^{-1} . The damage gradually extended across adjacent zones, forming a concentrated crack band with surrounding contour values of 1.21×10^{-1} and 1.07×10^{-1} .

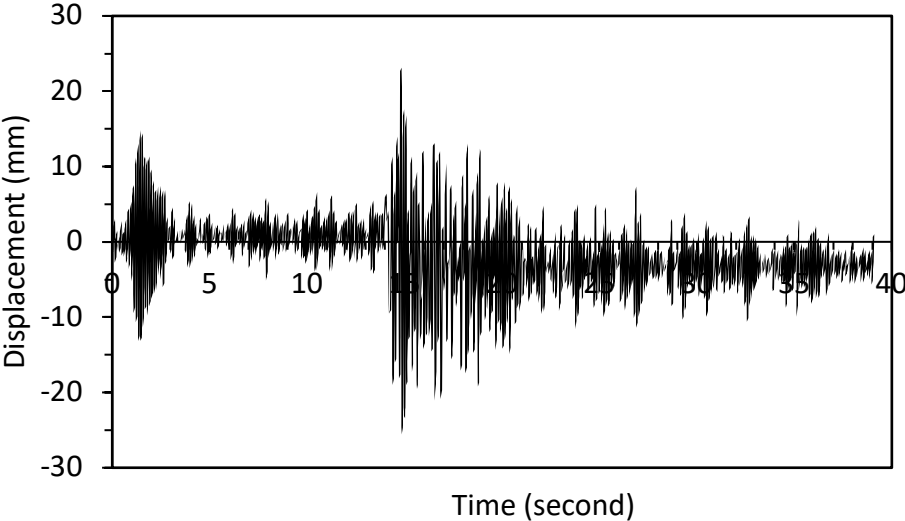


Figure 4.19 Graph showing horizontal crest displacement with time $u_{c(t)}$ for D1- scaled acceleration record site 9L.

In addition, minor tensile cracking was observed along the downstream wall, particularly below the crest. The damage in this region ranged from 6.74×10^{-2} to 4.04×10^{-2} , suggesting that the dam also experienced some degree of stress reversal or flexural tension from dynamic ground input.

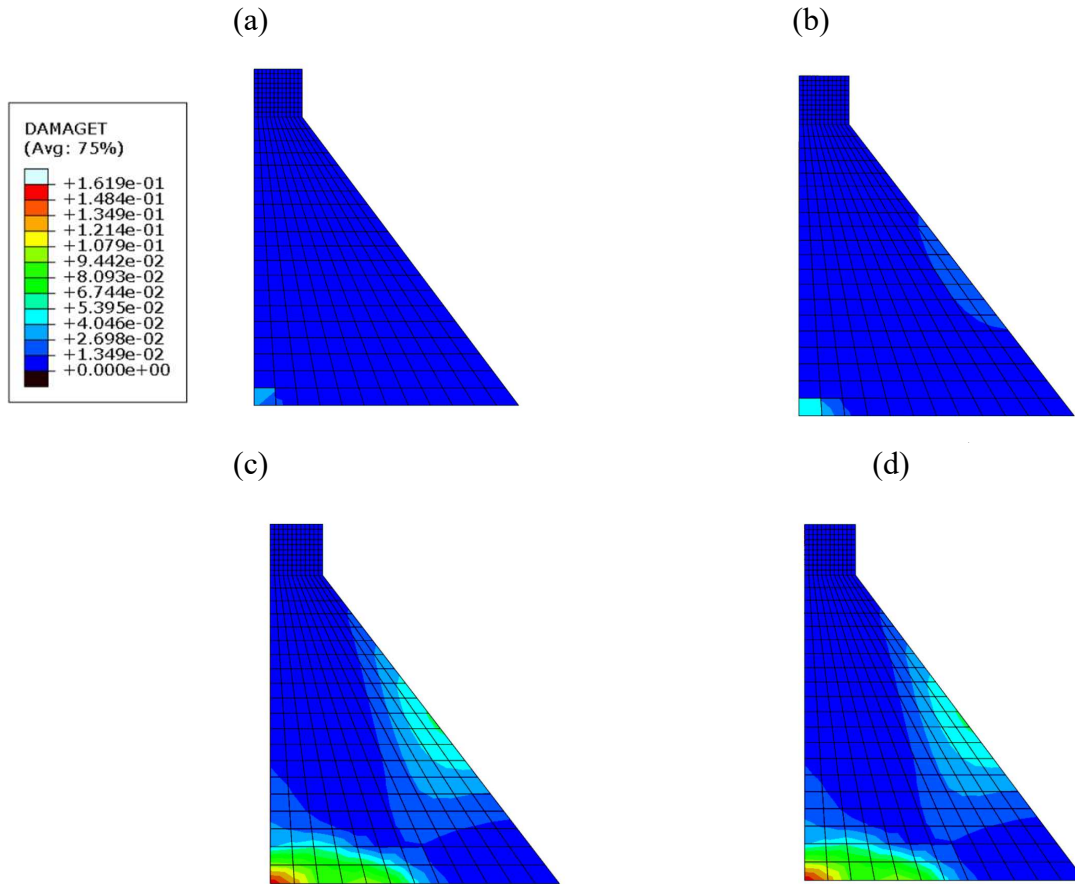


Figure 4.20 Contours of tensile damage d_t for D1 at time: (a) $t = 1.40$ s; (b) $t = 14.69$ s; (c) $t = 17.42$ s; (d) $t = 38.85$ s for scaled acceleration record of site 9L.

The simulation for Site 10L under scaled seismic excitation resulted in a maximum crest displacement of 32.40 mm at 13.75 seconds (Fig. 4.21). This ground motion input induced significant tensile stress responses, leading to damage both at the upstream heel and the downstream wall (Fig. 4.22). Cracking first initiated at the base, where the peak tensile damage reached 3.25×10^{-1} , surrounded by gradually reducing contour zones of 2.36×10^{-1} and 1.77×10^{-1} , indicating a broad area of stress propagation from the heel toward the core of the dam.

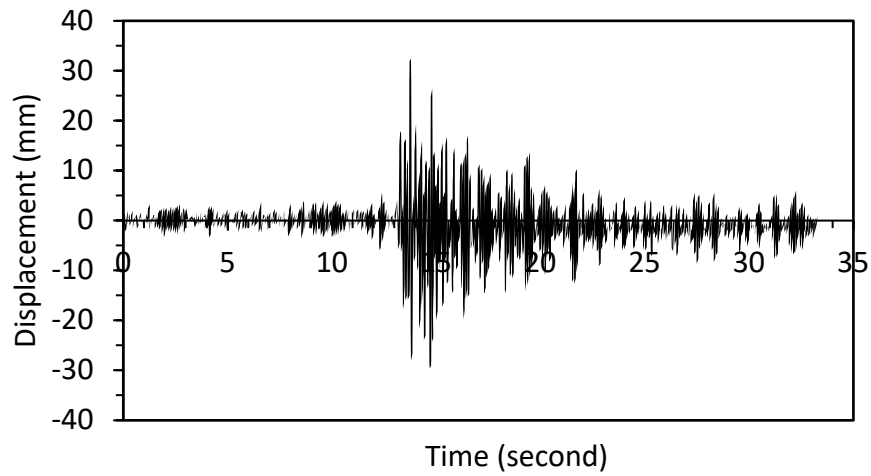


Figure 4.21 Graph showing horizontal crest displacement with time $u_{c(t)}$ for D1- scaled acceleration record site 10L.

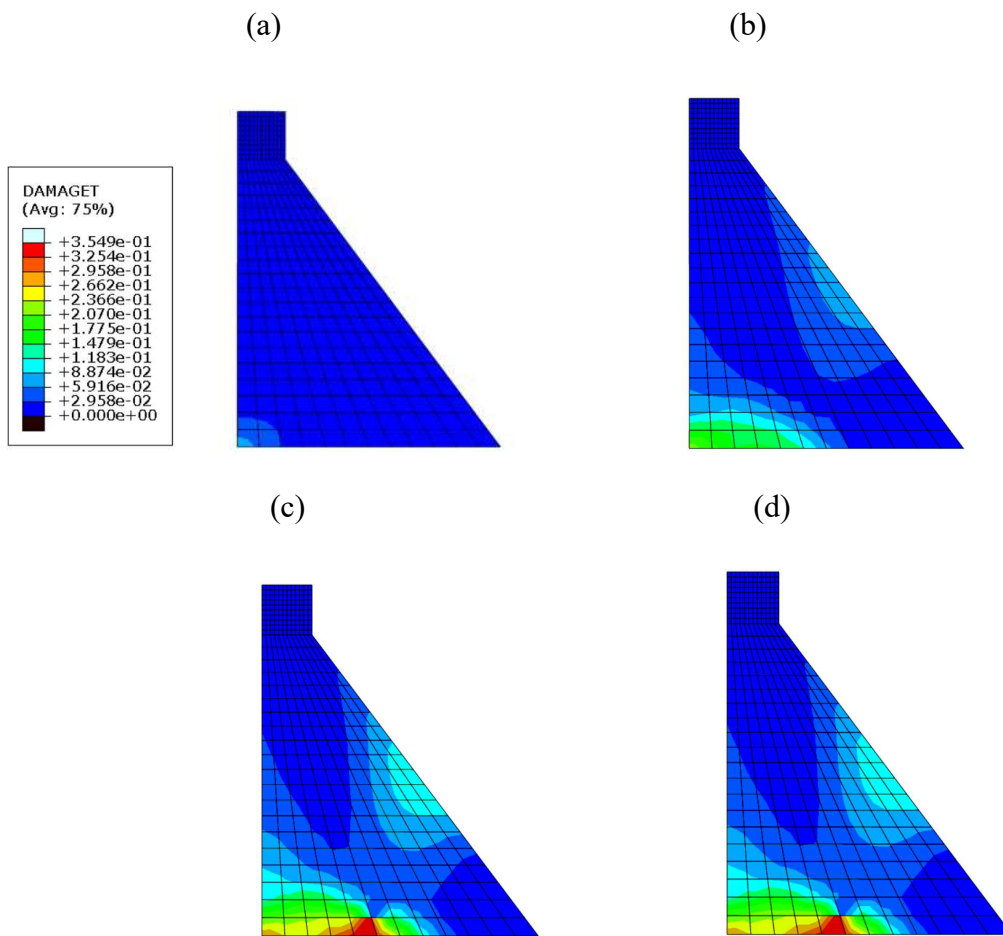


Figure 4.22 Contours of tensile damage d_t for D1 at time: (a) $t = 13.51$ s; (b) $t = 14.05$ s; (c) $t = 17.89$ s; (d) $t = 32.90$ s for scaled acceleration record of site 10L.

The simulation for Site 14L revealed moderate cracking across both the upstream base corner and the downstream wall below the crest. The dam experienced a maximum crest displacement of 25.99 mm (Fig. 4.23), with tensile damage initiating shortly thereafter. At the base, the damage values peaked at 2.38×10^{-1} , 2.17×10^{-1} , and 1.93×10^{-1} , forming a concentrated cracking zone near the heel region (Fig. 4.24). The tensile damage near the crest reached a value of 6.51×10^{-2} .

In summary, the results clearly demonstrate that D1, when subjected to scaled earthquake records, experienced substantially more frequent and severe tensile cracking than under the original inputs. The upstream base corner remained the most critical and recurrent damage zone. Additionally, several simulations revealed cracking at the downstream sloping wall near the crest, underscoring the impact of amplified energy input, stress wave reflection, and dynamic interaction on dam behavior. These findings highlight the importance of considering scaled ground motions for seismic safety assessment, as real earthquake recordings may underestimate damage potential during more intense future events.

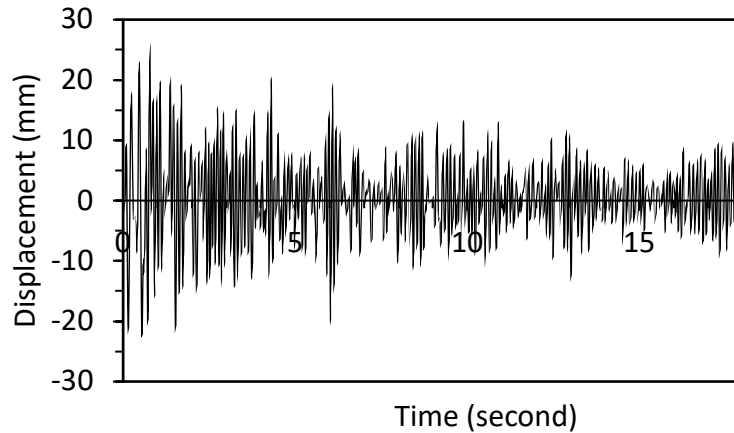


Figure 4.23 Graph showing horizontal crest displacement with time $u_c(t)$ for D1- scaled acceleration record site 14L.

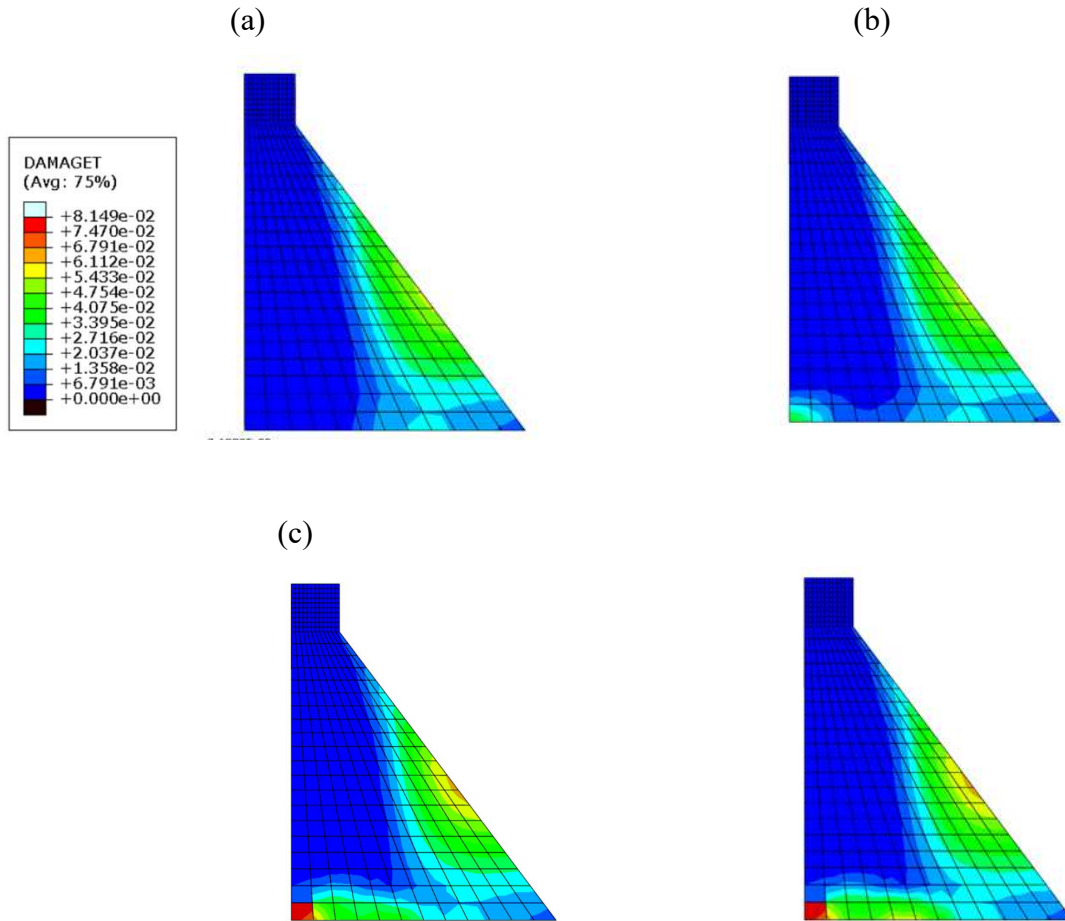


Figure 4.24 Contours of tensile damage d_t for D1 at time: (a) $t = 0.071$ s; (b) $t = 0.32$ s; (c) $t = 1.31$ s; (d) $t = 17.35$ s for scaled acceleration record of site 14L.

4.4.3 Dam D2 – Response to original acceleration records

Dam D2, characterized by a larger base width and greater overall mass compared to Dam D1, exhibited a noticeably more dynamic and damage-sensitive response when subjected to the original Saguenay earthquake acceleration records. A total of 22 simulations were carried out 11 with longitudinal and 11 with transverse components mirroring the methodology used for Dam D1. Unlike its smaller counterpart, Dam D2 demonstrated tensile damage in the majority of these simulations, with only four records (Sites 5L, 5T, 14L, and 14T) failing to produce visible cracking. This widespread damage pattern underscores the dam's increased vulnerability, which can be attributed to its larger dimensions.

In nearly all simulations, the upstream base corner emerged as the primary location for initial crack development, consistent with the behavior observed in Dam D1. However, the response of Dam D2 often included more complex damage propagation. Ground motions such as those recorded at Sites 1T, 9T and 20L induced tensile cracking not only at the upstream heel but also along the downstream wall near the crest.

Among all original ground acceleration record; simulations for Dam D2, Site 1T produced the highest recorded displacement, reaching 85.04 mm at 13.92 seconds (Fig. 4.25). The response was both intense and prolonged, with the dam exhibiting strong structural vibrations throughout the duration of seismic input. Tensile cracking initiated at 13.78 seconds (Fig. 4.26), closely aligned with the displacement peak, and intensified to its maximum by 17.28 seconds. The damage localized in two primary zones: at the upstream base corner, where the peak damage reached 3.20×10^{-2} , and along the upstream and downstream crest regions, where values reached 7.18×10^{-2} .

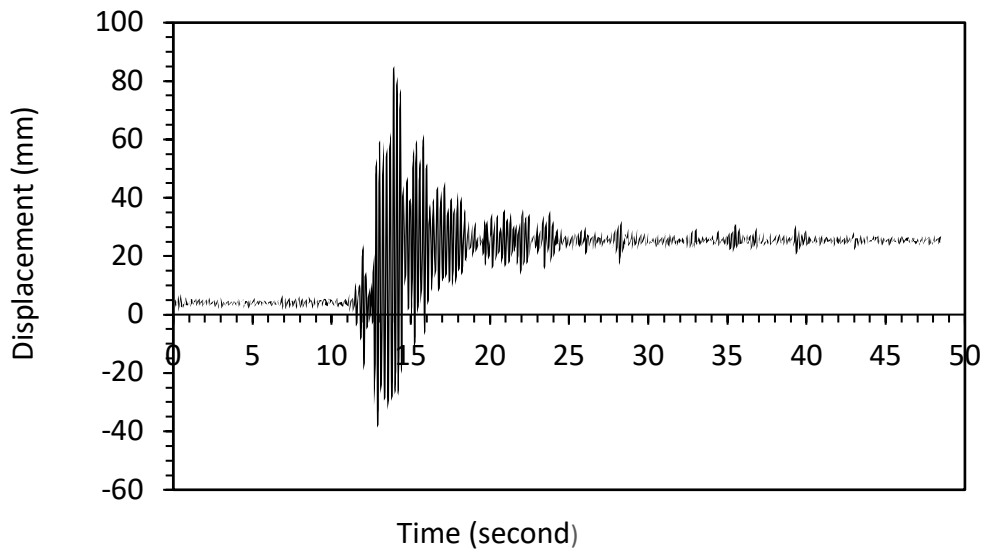


Figure 4.25 Graph showing horizontal crest displacement with time $u_c(t)$ for D2- site 1T.

The simulation for Site 9T resulted in a substantial crest displacement of 38.77 mm (Fig. 4.27), which peaked at 14.85 seconds. The dam exhibited a more prolonged and energetic vibration pattern compared to many other records, leading to progressive tensile cracking along the upstream base (Fig. 4.28). While the damage was not extensive in area, it was clearly traceable, with contour values ranging from 6.24×10^{-3} to 1.13×10^{-3} , centered at the heel of the structure. The evolution

of these fine-scale cracks demonstrates a gradual buildup of tensile stress, likely driven by repeated loading cycles during the peak shaking phase. Although the damage intensity remained relatively low, its appearance following a high displacement response reflects the dam's sensitivity to dynamic amplification and cumulative stress concentration at the base.

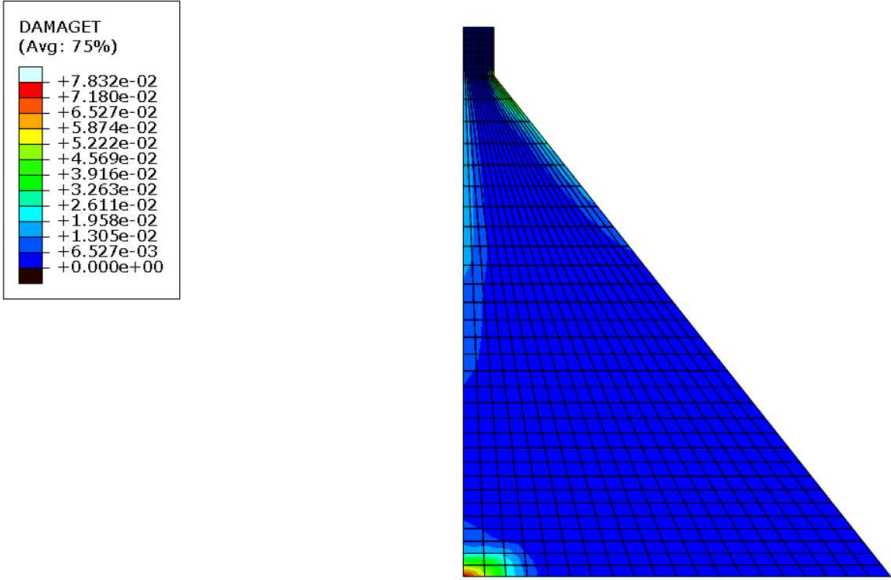


Figure 4.26 Contours of tensile damage d_t for D2 at time $t = 17.28$ s for record of site 1T.

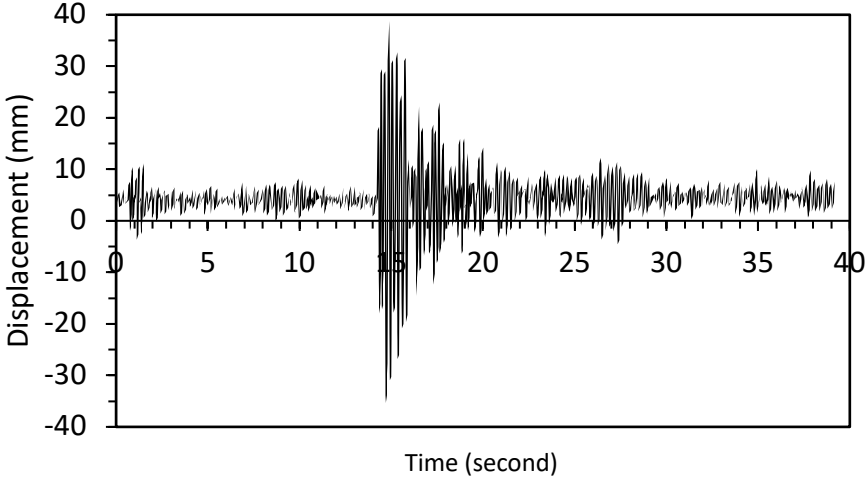


Figure 4.27 Graph showing horizontal crest displacement with time $u_c(t)$ for D2- site 9T.

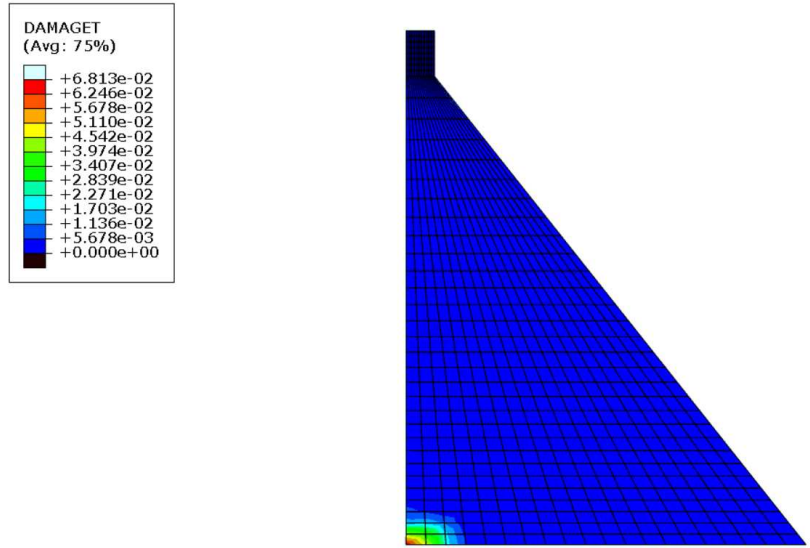


Figure 4.28 Contours of tensile damage d_t for D2 at time $t = 15.20$ s for record of site 9T.

The simulation for Site 20L showed a strong response, with the dam reaching a maximum displacement of -47.26 mm at 10.91 seconds (Fig. 4.29). Cracks began forming near the upstream base corner at 10.60 seconds and reached their peak by 11.29 seconds (Fig. 4.30). The tensile damage values in this region were 1.14×10^{-2} , 7.30×10^{-2} , and 3.13×10^{-2} . This result shows that high ground motion can cause noticeable cracking at the base of the dam in a short period. Even though the damage was not very large, it highlights that the base corner is a critical area under seismic loading.

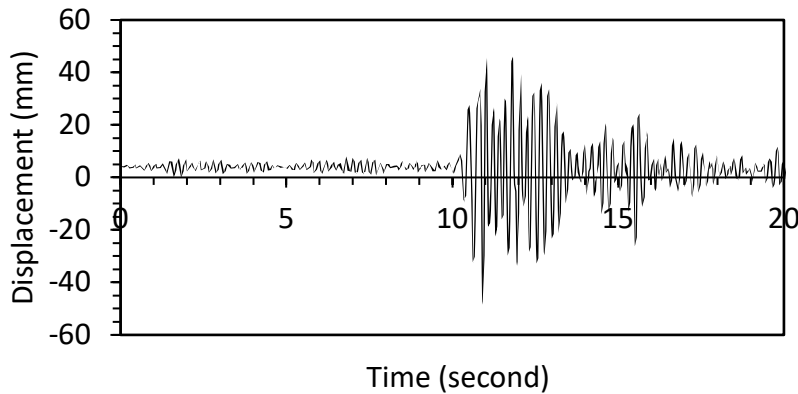


Figure 4.29 Graph showing horizontal crest displacement with time $u_c(t)$ for D2- site 20L.

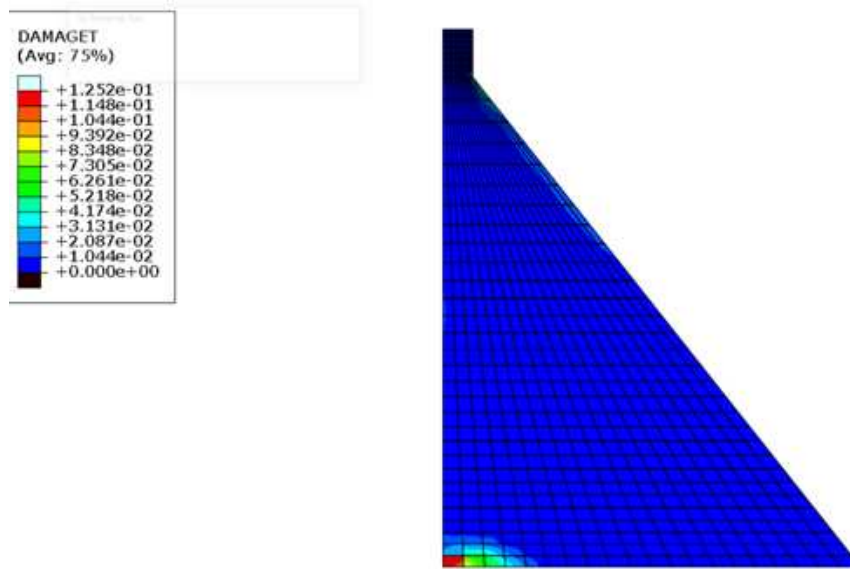


Figure 4.30 Contours of tensile damage d_t for D2 at time $t = 11.29$ s for record of site 20L.

In conclusion, Dam D2's response to the original Saguenay earthquake records highlights a significantly higher susceptibility to seismic-induced tensile damage than Dam D1. The results reveal frequent cracking, often distributed across multiple zones, particularly in simulations with high energy input or prolonged motion. The upstream base remained the most common crack initiation zone, but additional damage appeared along the sloped crest regions

4.4.4 Dam D2 – Response to scaled acceleration records

For the scaled acceleration records applied to D2, tensile damage was observed across nearly all simulations. While a few records showed only minimal damage localized to the upstream heel, many exhibited significant crack propagation both in extent and intensity-spanning the base and crest regions of the dam. The increased energy content from the scaled records, reflective of design-level seismic inputs, revealed critical vulnerabilities in the structure's seismic behavior.

The simulation for Site 1L showed a maximum displacement of -91.15 mm at 13.90 seconds, one of the largest in the entire scaled dataset. Tensile cracks appeared at the upstream heel at the same time as the displacement peak (Fig. 4.31). The maximum damage value at the heel reached 7.18×10^{-2} , with surrounding damage contours showing 3.91×10^{-2} . In addition to the

base damage, minor cracks extended vertically along both the upstream and downstream wall edges near the crest.

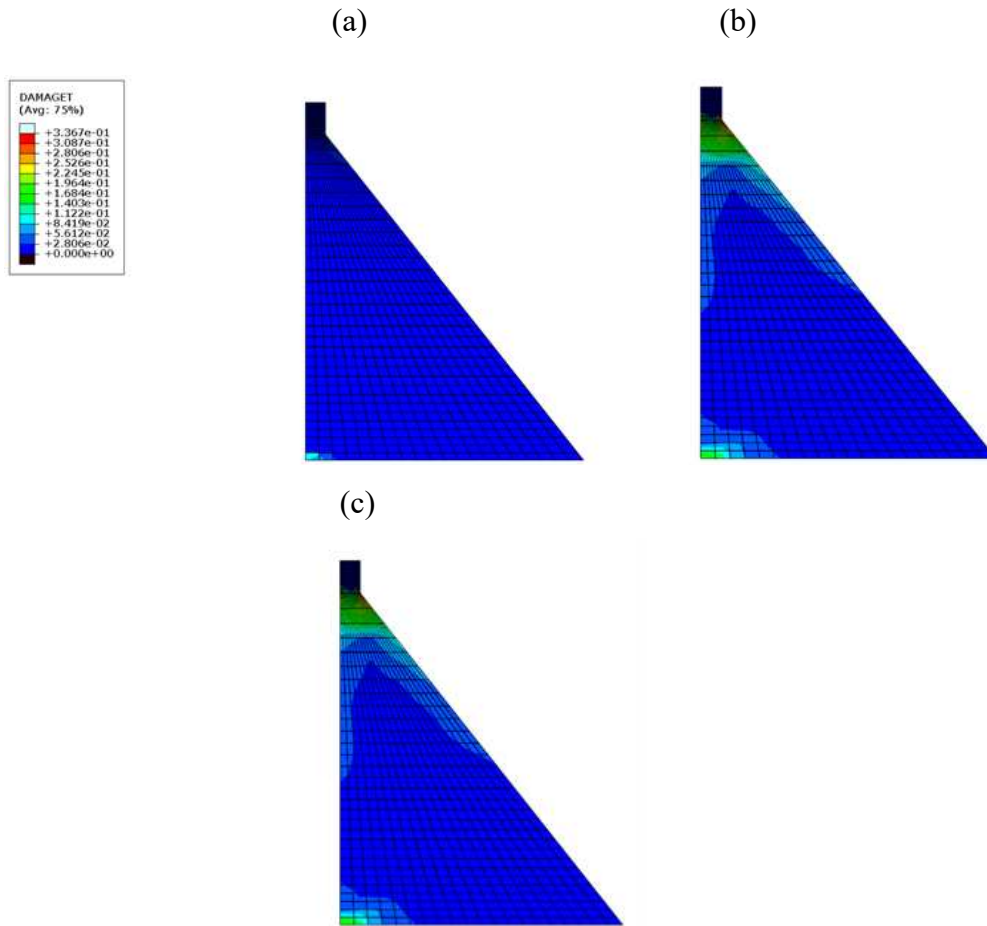


Figure 4.31 Contours of tensile damage d_t for D2 at time: (a) $t = 13.74$ s; (b) $t = 17.29$ s; (c) $t = 14.26$ s for scaled acceleration record of site1L.

The simulation for Site 9L recorded a maximum crest displacement of 105 mm at 14.00 seconds, making it one of the most extreme deformation cases. This large displacement was followed by significant cracking near the crest region (Fig. 4.32). The tensile damage peaked at 8.25×10^{-1} , spreading across the entire crest width. The damage then extended downward along the downstream face, where the intensity gradually reduced through contour values of 5.25×10^{-1} , 1.50×10^{-1} , and 7.50×10^{-2} . This pattern suggests a strong flexural response near the top, likely due to rotational effects under high dynamic loading.

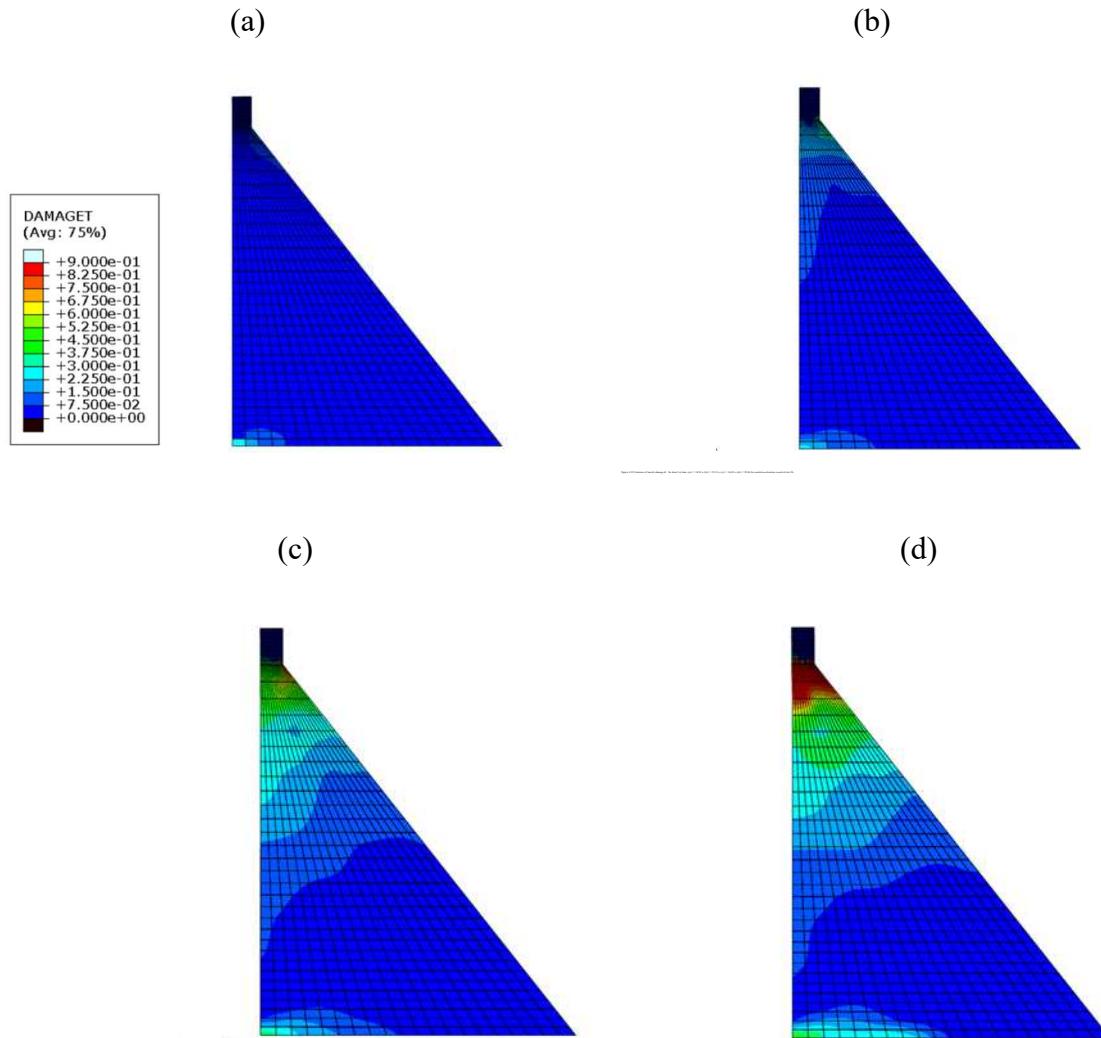


Figure 4.32 Contours of tensile damage d_t for D2 at time: (a) $t = 14.83$ s; (b) $t = 15.13$ s; (c) $t = 16.83$ s; (d) $t = 39.06$ for scaled acceleration record of site 9L.

The simulation for Site 9T recorded the highest displacement among all scaled acceleration cases, reaching 115.91 mm at 14.60 seconds. The cracking profile was nearly identical to that of Site 9L, with extensive damage concentrated near the crest region. The maximum tensile damage reached 8.25×10^{-1} (Fig. 4.33), covering the top section of the dam and extending down the downstream face. The crack propagation followed a descending gradient, with surrounding contour values of 5.25×10^{-1} , 1.50×10^{-1} , and 7.50×10^{-2} . This damage pattern reflects significant

flexural and inertial effects during peak ground motion, highlighting the crest as a critical zone for failure under intense seismic loads.

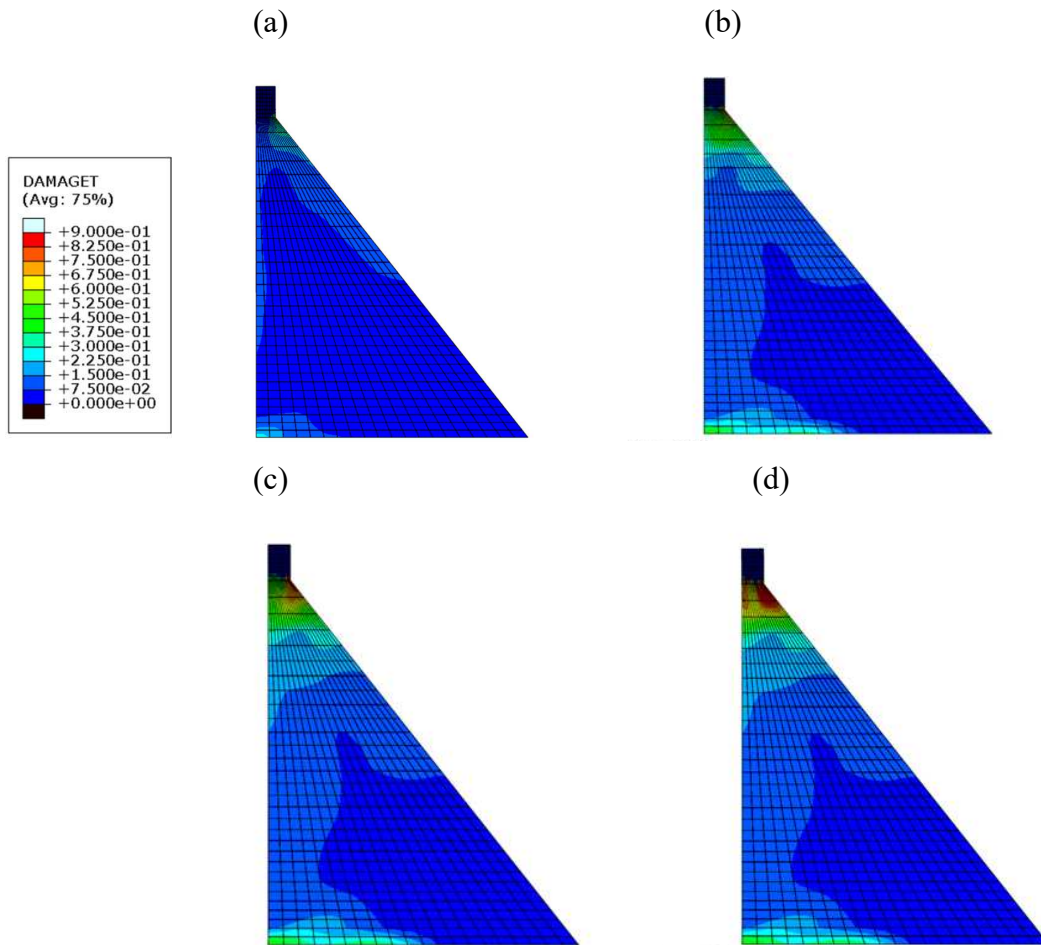


Figure 4.33 Contours of tensile damage d_t for D2 at time: (a) $t = 14.78$ s; (b) $t = 17.03$ s; (c) $t = 17.75$ s; (d) $t = 39.15$ s for scaled acceleration record of site 9T.

The simulation for Site 14L showed a very early and strong response, with the dam reaching a maximum displacement of 108 mm at just 0.4 seconds. This rapid motion led to significant tensile cracking, especially at the crest, where the peak damage reached 8.25×10^{-1} . Additional cracking was visible in the central and base regions of the dam (Fig. 4.34). The base damage was measured at 4.50×10^{-1} , while the central body recorded descending values of $1.50 \times$

10^{-1} and 7.50×10^{-2} . This distribution suggests a severe flexural response under the intense early ground motion, with cracking spreading both upward and downward from the crest.

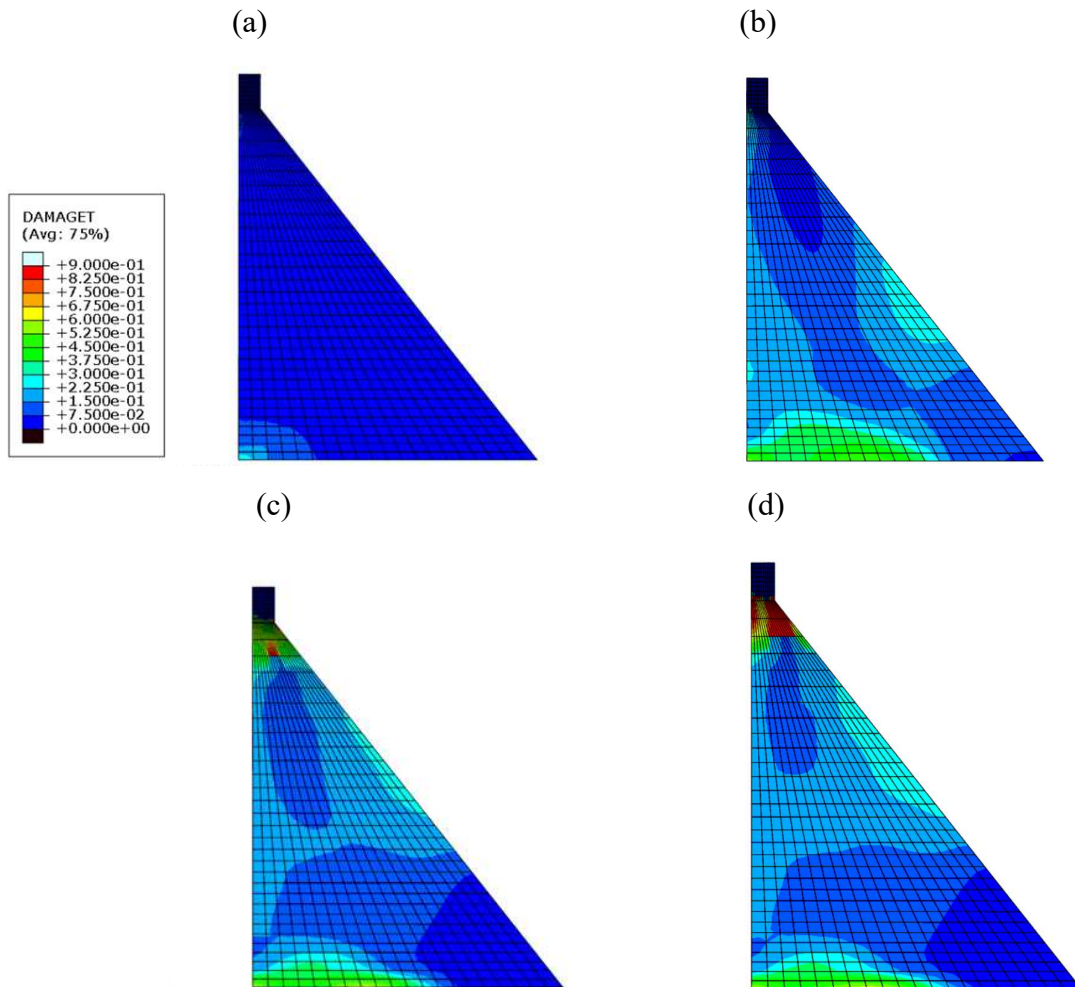


Figure 4.34 Contours of tensile damage d_t for D2 at time: (a) $t = 0.27$ s; (b) $t = 0.53$ s; (c) $t = 6.91$ s; (d) $t = 17.75$ s for scaled acceleration record of site 14L.

The simulation for Site 16L showed a strong and early seismic response, with the dam reaching a maximum displacement of -86.52 mm at 7.50 seconds. This record caused significant tensile damage at the crest, where the peak value reached 8.25×10^{-1} (fig. 4.35). In contrast, the damage at the base remained minimal, with a recorded value of 2.25×10^{-1} . This pattern suggests that the upper section of the dam experienced the most intense flexural stress during the shaking, while the base absorbed relatively less tensile impact.

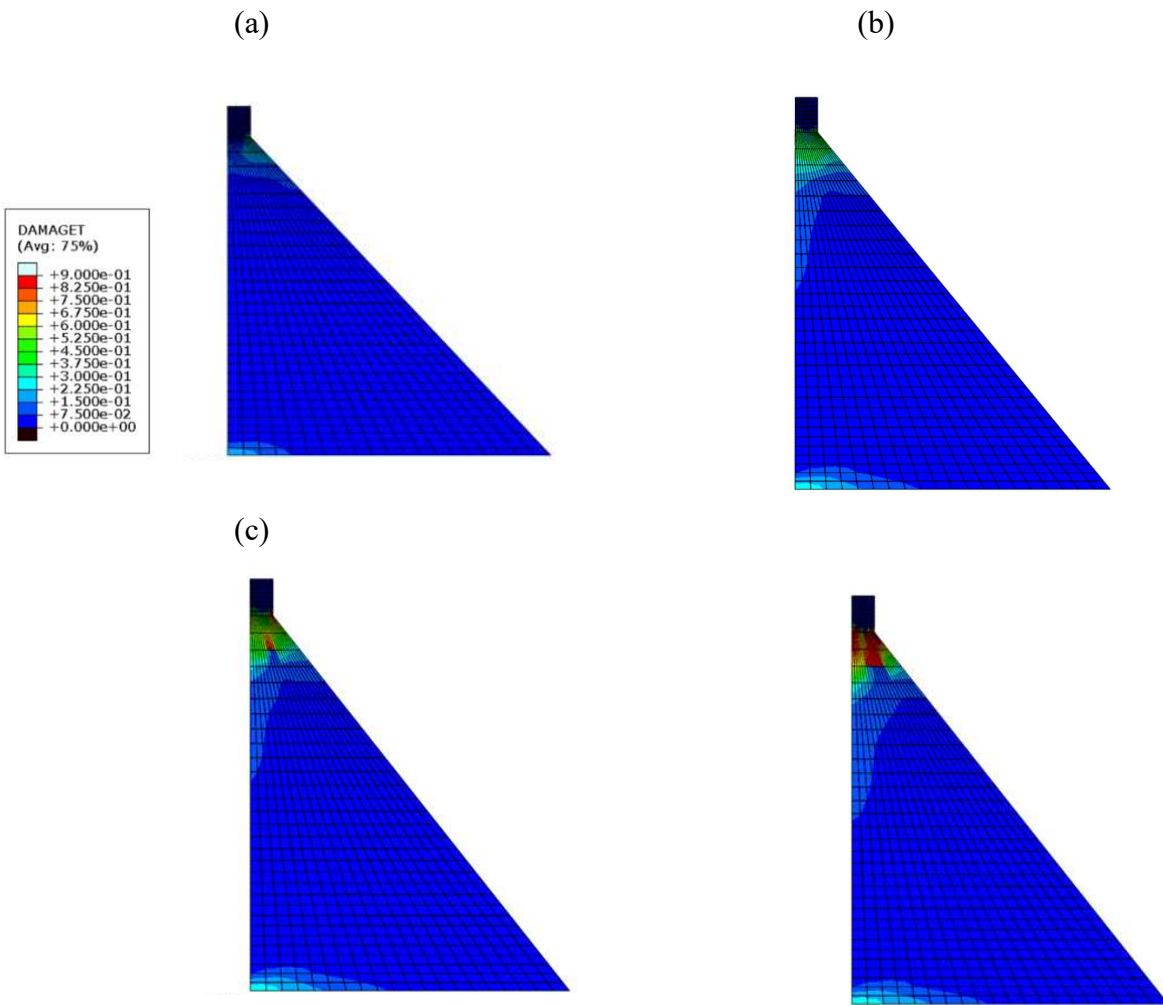


Figure 4.35 Contours of tensile damage d_t for D2 at time: (a) $t = 7.33$ s; (b) $t = 8.49$ s; (c) $t = 12.72$ s; (d) $t = 33.86$ s for scaled acceleration record of site 16L.

In the simulation for Site 20L, the dam experienced a maximum displacement of 89.86 mm at 11.80 seconds. Tensile damage was observed at both the upstream heel and the crest region (Fig. 4.36). Most of the cracking in these areas had values around 2.25×10^{-1} , while a small spot near the heel reached a peak of 4.14×10^{-1} . This result shows that the dam was affected at both the bottom and top, likely due to the strong shaking causing stress to build up in multiple locations.

In summary, when subjected to scaled records, Dam D2 showed intensified damage across nearly all cases. The crest became the dominant damage zone, with records like Site 9L and 9T resulting in extremely high crest displacements (105 mm and 115.91 mm) and peak tensile damage

values up to 8.25×10^{-1} . Additional simulations, such as Site 14L and 16L, demonstrated rapid response and flexural cracking, especially near the top of the dam. Some base cracking persisted, particularly under records like Site 20L, but overall, the crest consistently emerged as the most critical failure zone. These results highlight the dam's reduced resilience under higher intensity seismic events.

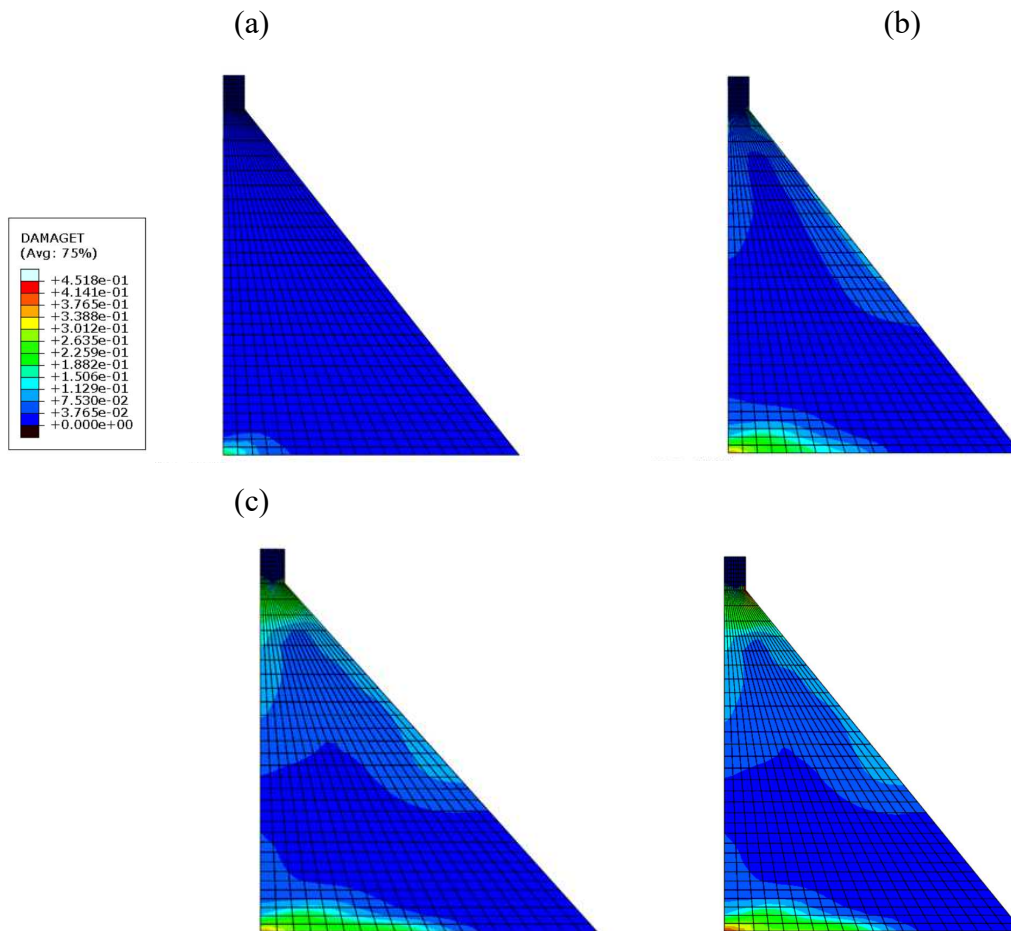


Figure 4.36 Contours of tensile damage d_t for D2 at time: (a) $t = 10.56$ s; (b) $t = 11.30$ s; (c) $t = 12.41$ s; (d) $t = 20.59$ s for scaled acceleration record of site 20L.

4.5 Discussion

4.5.1 Heel Damage Mechanisms

Across both dams, the upstream heel emerged as the most consistently affected location for tensile cracking, particularly under scaled seismic input. This vulnerability is attributed to the concentration of tensile stress that forms at the interface between the dam body and the base. In this study, the base was assumed to be fixed, with no foundation or dam–foundation interaction modelled, which may have amplified stress accumulation near the heel due to the lack of energy dissipation through the foundation medium. During dynamic excitation, especially under upstream-directed ground motion, the dam undergoes rocking about its toe, inducing uplift forces at the heel. This rotation generates tensile stresses that are further intensified by hydrostatic pressure acting in opposition and stress wave reflections at the rigid base. These combined effects often exceed the tensile strength of concrete, particularly when amplified by strong ground shaking, resulting in material degradation and the initiation of cracks. The CDP model effectively captured this progressive tensile damage, with visible crack evolution in scaled simulations such as Sites 2L and 10L for Dam D1 and in nearly all scaled records for Dam D2.

In Dam D2, the broader base and greater mass led to higher inertial forces, which magnified the base shear and concentrated dynamic stresses at the heel. The resulting damage zones were not only more frequent but also extended deeper and across wider regions, indicating a compounded influence of geometry, mass, and loading intensity. In several simulations, the accumulation of tensile degradation across multiple stress cycles sometimes occurring before peak displacement, suggested a fatigue-driven cracking mechanism. This highlights the importance of accounting for time-dependent material softening when assessing seismic vulnerability in dam structures.

4.5.2 Crest Damage Mechanisms

The crest region became increasingly susceptible to cracking as seismic input was scaled. This can be attributed to the flexural behaviour of the dam body under scaled acceleration records. As inertial forces act on the dam, the structure behaves like a cantilevered wall, bending back and forth about its base. This bending creates a tension-compression pair across the height of the dam: compression develops near the toe, and tensile stresses arise at the crest. Due to the absence of overburden pressure or lateral confinement at the top, the crest is structurally weaker and more vulnerable to crack initiation under tension.

In scaled simulations such as Sites 7T and 14L, Dam D2 exhibited significant crest cracking, sometimes extending vertically downward through the downstream face. These patterns indicate that flexural tension, coupled with geometric amplification of displacement at the crest, plays a dominant role in damage development. The extreme values of tensile damage (~ 0.9) observed near the crest further suggest that this region is not merely a secondary failure zone but a critical one under high-magnitude dynamic loading.

4.5.3 Crest Displacement Response

Crest displacement reflects the dam's dynamic response, with the crest typically undergoing the highest lateral movement due to its position as the free end of a cantilevered structure. In Dam D1, crest displacements were modest under original records but exceeded 40 mm under scaled inputs, marking the transition to nonlinear behaviour and triggering flexural cracking at both crest and heel.

Dam D2 showed much larger displacements, often surpassing 100 mm in scaled cases (e.g., Sites 9T and 14L), due to resonance with long-period ground motions and lower stiffness. These large displacements contributed to severe crest cracking, confirming that flexural demand and modal amplification drive damage patterns. Crest displacement thus serves as a key indicator of structural performance and should be closely monitored in seismic assessments and retrofit planning.

Moreover, in several scaled records such as Site 9T, the crest displacement time histories showed a permanent residual offset, where the displacement baseline did not return to zero after the strong shaking phase. This residual shift is indicative of irreversible nonlinear behavior caused by tensile cracking and stiffness degradation at the crest. Such permanent deformations demonstrate that the crest region undergoes not only transient amplification of motion but also long-term structural damage, which could compromise serviceability under subsequent seismic events.

4.5.4 Modal Interaction Effects

The distinct seismic behavior of D1 and D2 highlights the importance of modal characteristics in governing dam response. Dam D1, with a higher fundamental frequency, did not resonate with the long-period energy content of the Saguenay records. As a result, its response under original inputs remained within the elastic regime, and damage was minimal. Conversely,

Dam D2, with lower stiffness and longer natural periods, experienced dynamic amplification due to modal alignment with the dominant ground motion frequencies. This resonance significantly increased crest displacement and tensile stresses, triggering widespread damage even under unscaled motions. Moreover, several simulations revealed a delay between peak displacement and peak tensile damage, particularly in Dam D2. This temporal gap supports the presence of modal coupling and cumulative damage effects, where energy is absorbed and redistributed over time, gradually degrading material capacity. These interactions become more pronounced in larger dams, where higher-mode participation and longer vibration durations allow for internal stress redistribution that cannot be captured by simplified models.

4.5.5 Compressive Damage

Although the CDP model allows simulation of compressive crushing (d_c), a screening of representative simulations was performed to check for this mode of failure. The results showed no compressive damage in the cases examined. This outcome is consistent with the expected flexural response of gravity dams, where tensile cracking at the crest and heel dominates the seismic behavior, while compressive stresses at the toe remain within capacity. Because the screened cases showed no compressive damage, detailed contour plots for d_c were not included, and the analysis focused on tensile damage, which represents the critical failure mechanism.

4.5.6 Evaluation Framework and Comparative Insights

The seismic assessment framework presented in this study offers a practical and adaptable procedure for evaluating the structural safety of concrete gravity dams under earthquake loading. The nonlinear finite element approach using the CDP model in ABAQUS has been successfully applied to two Canadian dams (D1 and D2) each featuring distinct geometries and frequency characteristics. The same modeling approach was also validated using the well-documented Koyna Dam, reinforcing its generalizability. This workflow comprising dam geometry modeling, mesh generation, material property assignment, loading application, and damage analysis can be readily applied to other dams globally. Only the dam geometry and concrete parameters need to be updated, making this a flexible method for engineers and researchers aiming to assess seismic vulnerability in diverse regions.

Compared to previous studies, this work incorporates important methodological differences. Alembagheri (2016), for instance, employed linear time-history simulations with

empirical damage criteria based on crest displacements and demand-capacity ratios. While useful for fast screening, such approaches require post-processing assumptions about failure states and cannot simulate the full range of nonlinear behaviour, including crack initiation, propagation, and residual capacity. Our method eliminates this gap by using a constitutive model capable of directly capturing inelastic concrete behavior under seismic loading. Similarly, fragility-based studies (Bernier et al., 2016; Lupoi & Callari, 2012) often rely on simplified lumped-mass models or reduced-order finite element formulations, which may neglect spatial damage distribution or realistic material degradation. In contrast, our use of full-continuum models provides spatial resolution of cracking patterns, enabling the identification of critical zones like the upstream heel and dam crest.

A key advantage of the proposed method lies in its generalizability. Once dam-specific parameters are defined, the same modelling procedure can be applied elsewhere. The use of ABAQUS software also makes the process accessible, even for engineering teams with limited computational resources, as the tool offers prebuilt CDP modules and efficient meshing capabilities. However, the study does come with limitations. Most notably, dam-foundation and soil-structure interaction (SSI) effects were not explicitly modelled both dams were assumed to be rigidly fixed at the base. While this simplification is common in many nonlinear dam studies, it may lead to overestimation of internal stress and underrepresentation of energy dissipation through the foundation. Future studies should incorporate SSI and hydrodynamic pressure effects to refine results, especially for dams founded on softer soils or deep reservoir bases.

Regionally, this study helps fill an important gap in seismic safety literature. Eastern Canada has received relatively little attention in dam focused seismic assessments, despite the existence of hundreds of aging structures, many built before modern seismic codes. While seismicity in this region is considered moderate, events such as the 1988 Saguenay Earthquake revealed the potential for damaging ground motions. By applying scaled records from that event, our study provides a site-specific evaluation using realistic ground motion inputs, aligned with Canadian seismic hazard maps. It also offers a foundation upon which future Eastern Canadian dam studies particularly those exploring fragility curves or probabilistic risk can build. The comparative analysis between D1 and D2 further emphasizes how modal properties, geometry, and input directionality influence seismic response, offering insight for regional prioritization of dam retrofitting needs.

In summary, this study contributes both technically and regionally. Technically, it presents a detailed and validated nonlinear modelling approach that improves on traditional and semi-empirical methods by capturing true material behaviour and spatial damage patterns. Regionally, it addresses the lack of dam-specific seismic evaluations in Eastern Canada and provides a repeatable framework that others can adopt or extend. While limitations such as neglecting SSI remain, the presented results form a robust basis for future fragility analysis, performance-based design, and seismic retrofitting decisions across similar moderate seismic regions.

Chapter 5 : Conclusions

5.1 Summary and Conclusions

This thesis presented a comprehensive numerical study on the seismic response of two gravity dams, Dam D1 (Montreal) and Dam D2 (La Malbaie), subjected to both original and scaled acceleration records from the 1988 Saguenay Earthquake. The methodology integrated advanced finite element modeling using ABAQUS, scaling using SeismoLEE, and damage assessment through the CDP model. The primary goal was to assess crack initiation, displacement response, and overall seismic vulnerability of each structure under a range of realistic and intensified ground motions. To ensure the accuracy of the modeling approach, validation was first conducted using the Koyna Dam case study. The results of modal analysis, crest displacement history, and damage contours showed excellent agreement with existing literature and open-source ABAQUS references, confirming the reliability of the simulation setup.

Subsequent modal analysis revealed clear distinctions between the two dams. Dam D1, being smaller and stiffer, had a higher fundamental frequency (68.45 rad/s), while Dam D2, with its greater mass and flexibility, exhibited lower natural frequencies (29.70 rad/s). This dynamic difference significantly influenced each dam's response to ground motions. Under original unscaled earthquake inputs, Dam D1 showed high seismic resilience. Tensile damage was sparse, low in magnitude, and localized primarily at the upstream base corner, confirming the structural soundness of the dam under moderate seismic demand. In contrast, Dam D2 demonstrated significantly higher susceptibility to cracking, with damage appearing in most simulations, including flexural cracks near the crest and broader crack propagation paths due to its larger size and dynamic flexibility.

The impact of scaled acceleration records was even more pronounced. In Dam D1, tensile damage became widespread, with many simulations showing multi-zone cracking including both the base and crest areas. Scaled records highlighted the importance of early acceleration pulses and their alignment with the dam's modal characteristics in triggering failure. For Dam D2, the scaled inputs led to extreme crest displacements and severe tensile. The crest emerged as a critical failure zone, with flexural and inertial stresses creating a full-depth cracking pattern in multiple

cases. Records such as Sites 9T, 14L, and 16L produced damage values nearing complete material degradation ($d_t = 0.9$), indicating structural instability under high-energy excitation.

Overall, the study confirms that:

1. The upstream heel consistently emerged as the most vulnerable region, but under intense input, crest regions and downstream faces also became susceptible to cracking due to rocking and flexural effects.
2. Seismic vulnerability is strongly influenced by dam geometry and dynamic properties.
3. Scaled records provide a more critical and realistic assessment of structural demand, especially in regions of low-to-moderate seismicity where design ground motions may underestimate true performance thresholds.

5.2 Recommendations and Future Work

While this study provides meaningful insights into the seismic performance of concrete gravity dams through advanced numerical modeling, several simplifying assumptions limit the generalizability of the findings and point toward avenues for future research. Most notably, the analysis did not consider the interaction between the dam, foundation, and reservoir, which is known to significantly influence seismic response. The effects of hydrodynamic pressures from the upstream reservoir during ground shaking were also not explicitly modeled. As a result, the current simulations may underestimate or oversimplify key dynamic behaviors, including energy transmission, damping, and added mass effects due to water-structure interaction. Future studies should aim to incorporate fully coupled dam–foundation–reservoir models, potentially using fluid–structure interaction (FSI) techniques or acoustic-structural coupling available in finite element platforms such as Abaqus. These additions would allow for a more realistic assessment of hydrodynamic pressure distribution and its influence on stress localization and crack propagation.

In addition, the current work assumes ideal boundary and interface conditions. Future investigations may benefit from modeling nonlinear soil–structure interaction at the dam–foundation interface, as well as time-dependent phenomena such as concrete aging, thermal effects, and degradation under sustained loading. In this study, an ultimate compressive strength of 25 MPa was adopted, consistent with American Concrete Institute (2014) guidelines for mass concrete. However, the actual strength of dam concrete can vary depending on the construction era and long-term material aging. Older dams may have significantly lower strengths than modern

ones, and degradation over decades of service may further affect seismic performance. Future work should therefore examine the influence of material aging and strength variability on dam seismic safety. The use of probabilistic seismic demand models or the development of fragility curves could further enhance the practical application of this research, particularly for risk-informed decision-making and prioritization of dam safety upgrades in seismically active or infrastructure-critical regions. By addressing these limitations, future work can build upon the solid foundation established in this thesis to achieve a more comprehensive and robust understanding of gravity dam performance under seismic loading.

Chapter 6 : References

- 1) Abaqus. (2014). Abaqus theory manual (Version 6.14). <https://classes.engineering.wustl.edu/2009/spring/mase5513/abaqus/docs/v6.6/books/stm/default.htm>
- 2) ABAQUS. (2009). Example 2.1.15: Seismic analysis of a concrete gravity dam. In ABAQUS Example Problems Manual (Version 6.6). Retrieved from <https://classes.engineering.wustl.edu/2009/spring/mase5513/abaqus/docs/v6.6/books/exa/default.htm?startat=ch02s01aex67.html>
- 3) Alembagheri, M. (2016). Earthquake damage estimation of concrete gravity dams using linear analysis and empirical failure criteria. *Soil Dynamics and Earthquake Engineering*, 90, 327-339. <https://doi.org/10.1016/j.soildyn.2016.09.005>
- 4) Al Marahlleh, N. H. (2022). Two-dimensional dynamic nonlinear finite element model based seismic analysis of a concrete gravity dam. *IOSR Journal of Mechanical and Civil Engineering (IOSR-JMCE) e-ISSN*, 19, 1–10.
- 5) Sesli, H., Altunişik, A. C., Akköse, M., & Hüsem, M. (2016). Near-fault ground motion pulse effects on the dynamic behavior of concrete gravity dam–reservoir–foundation systems using different water modelling approaches. In *Proceedings of the 12th International Congress on Advances in Civil Engineering*, Istanbul, Turkey, September 2016.
- 6) Alsuleimanagha, Z., & Liang, J. (2012). Dynamic analysis of the Baozhusi dam using FEM. (Dissertation). Retrieved from <https://urn.kb.se/resolve?urn=urn:nbn:se:kth:diva-171817>
- 7) American Concrete Institute. (2014). ACI 318-14: Building code requirements for structural concrete (Code & Commentary). <https://www.phd.eng.br/wp-content/uploads/2015/12/en.1992.1.1.2004.pdf>
- 8) Bader, S., & Clayton, P. (2022). Determining natural frequency and dynamic characteristics of structures using free and force vibration testing methods. (NSF NHERI data report: PRJ-2045). <https://doi.org/10.17603/DS2998P>

- 9) Baker, J. W., & Cornell, C. A. (2006). Spectral shape, epsilon and record selection. *Earthquake Engineering and Structural Dynamics*, 35(9), 1077-1095. <https://doi.org/10.1002/eqe.571>
- 10) Bernier, C., Monteiro, R., & Paultre, P. (2016). Using the conditional spectrum method for improved fragility assessment of concrete gravity dams in Eastern Canada. *Earthquake Spectra*, 32(3), 1449–1468. <https://doi.org/10.1193/072015EQS116M>
- 11) Bray, J. D., & Rodriguez-Marek, A. (2004). Characterization of forward-directivity ground motions in the near-fault region. *Soil Dynamics and Earthquake Engineering*, 24, 815-828. <https://doi.org/10.1016/j.soildyn.2004.05.001>
- 12) Canadian Dam Association. (2013). *Dam Safety Guidelines*. <https://cda.ca/publications/cda-guidance-documents/dam-safety-publications>
- 13) Chen, D. H., Yang, Z. H., Wang, M., & Xie, J. H. (2019). Seismic performance and failure modes of the Jin'anqiao concrete gravity dam based on incremental dynamic analysis. *Engineering Failure Analysis*, 100, 227-244. <https://doi.org/10.1016/j.engfailanal.2019.02.018>
- 14) Chopra, A. K. (1995). *Dynamics of structures: Theory and applications to earthquake engineering* (2nd ed.). Prentice Hall, Englewood Cliffs, NJ.
- 15) Chopra, A. K., & Chakrabarti, P. (1973). The Koyna earthquake and the damage to Koyna Dam. *Bulletin of the Seismological Society of America*, 63(2), 381-397. <https://doi.org/10.1785/bssa0630020381>
- 16) Chopra, A.K., & Chakrabarti, P. (1981). Earthquake response of concrete gravity dams including dam-water-foundation rock interaction. *Earthquake Engineering and Structural Dynamics*, 9(4), 363-383. <https://doi.org/10.1002/eqe.4290090406>
- 17) Canadian Standards Association. (2019). *Design of concrete structures*. Canadian Standards Association, Mississauga, ON, Canada. CSA A23.3:19. <https://www.csagroup.org/store/product/CSA%20A23.3:19/?srsltid=AfmBOopd0VLYTeF0rwSli7R7J8E6xZa9MCPTytb47nGknzw2UI8jYxj>
- 18) Duan, W., Bouaanani, N., & Miquel, B. (2019). Effects of selection and modification of ground motions on the seismic safety evaluation of gravity dams in Eastern Canada. *Proceedings of the 12th Canadian Conference on Earthquake Engineering*, June 17–20, 2019, Quebec, QC, pp. 1-8.

- 19) European Committee for Standardization. (2004). Eurocode 2: Design of concrete structures - Part 1-1: General rules and rules for buildings (EN 1992-1-1). European Commission (JRC). Retrieved from <https://www.phd.eng.br/wp-content/uploads/2015/12/en.1992.1.1.2004.pdf>
- 20) Federal Emergency Management Agency. (2005). Federal guidelines for dam safety: Earthquake analyses and design of dams (FEMA 65). Association of State Dam Safety Officials. https://damfailures.org/sites/default/files/wp-pdf/Federal-Guidelines-for-Dam-Safety_Earthquake-Analysis-and-Design-of-Dams.pdf
- 21) Ghaemian, M., & Ghobarah, A. (1997). Seismic response of the Sefidrud concrete buttress dam. *European Earthquake Engineering*, 11(1), 3–15. https://www.researchgate.net/publication/272025873_Seismic_response_of_the_Sefidrud_concrete_buttress_dam.
- 22) Grassl, P., Xenos, D., Nyström, U., Rempling, R., & Gylltoft, K. (2013). CDPM2: A damage-plasticity approach to modelling the failure of concrete. *International Journal of Solids and Structures*, 50(24), 3805–3816. <https://doi.org/10.1016/j.ijsolstr.2013.07.008>
- 23) Hafezolghorani, M., Hejazi, F., Vaghei, R., Jaafar, M. S. Bin, & Karimzade, K. (2017). Simplified damage plasticity model for concrete. *Structural Engineering International*, 27(1), 68–78. <https://doi.org/10.2749/101686616X1081>
- 24) Hydro-Québec (2023). Generating stations. <https://www.hydroquebec.com/generation/generating-stations.html>
- 25) International Commission on Large Dams (ICOLD). (2022). World Register of Dams 2022. Paris, France: ICOLD. Retrieved from <https://www.icold-cigb.org>
- 26) Jiang, S., Du, C., & Hong, Y. (2013). Failure analysis of a cracked concrete gravity dam under earthquake. *Engineering Failure Analysis*, 33, 265-280. <https://doi.org/10.1016/j.engfailanal.2013.05.024>
- 27) Chavez, B. W., & Fenves, G. L. (1995). Earthquake response of concrete gravity dams including base sliding. *Journal of Structural Engineering*, 121(5), 865–875 [https://doi.org/10.1061/\(ASCE\)0733-9445\(1995\)121:5\(865\)](https://doi.org/10.1061/(ASCE)0733-9445(1995)121:5(865))
- 28) Lee, J., & Fenves, G. L. (1998). A plastic-damage concrete model for earthquake analysis of dams. *Earthquake Engineering & Structural Dynamics*, 27(9), 937-956,

[https://doi.org/10.1002/\(SICI\)1096-9845\(199809\)27:9%3C937::AID-EQE764%3E3.0.CO;2-5](https://doi.org/10.1002/(SICI)1096-9845(199809)27:9%3C937::AID-EQE764%3E3.0.CO;2-5)

- 29) Lei, B., Qi, T., Li, Y., Jin, Z., & Qian, W. (2023). An enhanced damaged plasticity model for concrete under cyclic and monotonic triaxial compression. *European Journal of Mechanics, A/Solids*, 100, 104999. <https://doi.org/10.1016/j.euromechsol.2023.104999>
- 30) Lin, L., & Adams, J. (2008). Seismic vulnerability and prioritization ranking of dams in Canada. In *Proceedings of the 14th World Conference on Earthquake Engineering (14WCEE)*, Beijing, China, October 12–17, 2008.
- 31) Lubliner, J., Oliver, J., Oller, S., & Oñate, E. (1989). A plastic-damage model for concrete. *International Journal of Solids and Structures*, 25(3), 299–326. [https://doi.org/10.1016/0020-7683\(89\)90050-4](https://doi.org/10.1016/0020-7683(89)90050-4)
- 32) Lupoi, A., & Callari, C. (2012). A probabilistic method for the seismic assessment of existing concrete gravity dams. *Structure and Infrastructure Engineering*, 8(10), 985–998. <https://doi.org/10.1080/15732479.2011.574819>
- 33) Madandoust, R., Kazemi, M., & Yousefi Moghadam, S. (2017). Analytical study on tensile strength of concrete. *Romanian Journal of Materials (Vol. 47, Issue 2)*. <https://www.researchgate.net/publication/318506827>
- 34) Mansouri, A., Ahmad Lashteh Neshaei, M., & Aghajany, R. (2011). Fracture analysis of concrete gravity dam under earthquake induced loads. *Journal of Applied Sciences and Environmental Management*, 15(2), 317-325. <http://hdl.handle.net/1807/51826>
- 35) Matsumoto, N., Sasaki, T., & Sato, N. (2012). Effects of the 2011 Tohoku earthquake on dams. In *Proceedings of the International Symposium on Dams for a Changing World* (pp. 1–6). Kyoto, Japan: International Commission on Large Dams (ICOLD). <https://search.jcold.or.jp/icold/symposium/2012/2012.52.pdf>
- 36) Mazighi, H., & Mihoubi, M. K. (2022). Damage of a concrete gravity dam under the effect of the hydrodynamic loads. *Procedia Structural Integrity*, 42, 1714–1720. <https://doi.org/10.1016/j.prostr.2022.12.216>
- 37) National Research Council of Canada. (2010). *National Building Code of Canada 2010*. Institute for Research in Construction, NRC, Ottawa, Ontario, Canada. <https://nrc.canada.ca/en/certifications-evaluations-standards/codes-canada/codes-canada-publications/national-building-code-canada-2010>

- 38) Beltaos, S., & Peters, D. L. (2020). Naturalized flow regime of the regulated Peace River, Canada, during the spring breakup of the ice cover. *Cold Regions Science and Technology*, 172, 103005. <https://doi.org/10.1016/j.coldregions.2020.103005>
- 39) Pekau, O. A., Lingmin, F., & Chuhan, Z. (1995). Seismic fracture of Koyna dam: Case study. *Earthquake Engineering & Structural Dynamics*, 24(1), 15-33. <https://doi.org/10.1002/eqe.4290240103>
- 40) Qu, Y., Zou, D., Kong, X., Yu, X., & Chen, K. (2020). Seismic cracking evolution for anti-seepage face slabs in concrete faced rockfill dams based on cohesive zone model in explicit SBFEM-FEM frame. *Soil Dynamics and Earthquake Engineering*, 133, 106106. <https://doi.org/10.1016/j.soildyn.2020.106106>
- 41) Sarkhel, S., Padhi, J., & Dash, A. K. (2020). Seismic analysis of a concrete gravity dam using ABAQUS. In *Lecture notes in civil engineering* (pp. 253-263). https://doi.org/10.1007/978-981-15-4577-1_21
- 42) Segura, R., Bernier, C., Monteiro, R., & Paultre, P. (2019). On the seismic fragility assessment of concrete gravity dams in Eastern Canada. *Earthquake Spectra*, 35(1), 211–231. <https://doi.org/10.1193/012418EQS024M>
- 43) Serra, C., Batista, A. L., Azevedo, N. M., Custódio, J. (2017). prediction of dam concrete compressive and splitting tensile strength based on wet-screened concrete test results. *Journal of Materials in Civil Engineering*, 29(10), 04017188. [https://doi.org/10.1061/\(asce\)mt.1943-5533.0002012](https://doi.org/10.1061/(asce)mt.1943-5533.0002012)
- 44) Shome, N., Cornell, C. A., Bazzurro, P., & Carballo, J. E. (1998). Earthquakes, records, and nonlinear responses. *Earthquake Spectra*, 14(3), 469-500. <https://doi.org/10.1193/1.1586011>
- 45) Tanaka, T., Tatsuoka, F., & Mohri, Y. (2012). Earthquake-induced failure of Fujinuma Dam. In *Proceedings of the International Symposium on Dams for a Changing World (1–12)*. Kyoto, Japan: International Commission on Large Dams (ICOLD) <https://search.jcold.or.jp/icold/symposium/2012/2012.51.pdf>.
- 46) Tayie, M. S. (2018). Impact of the international context on the political and legal dimensions of the Aswan High Dam (1952-1960). In A. Negm & S. Abdel-Fattah (Eds.), *Grand Ethiopian Renaissance Dam versus Aswan High Dam (The Handbook of Environmental Chemistry, 79)*. Cham: Springer. https://doi.org/10.1007/698_2017_219

- 47) Tidke, A. R., & Adhikary, S. (2021). Seismic fragility analysis of the Koyna gravity dam with layered rock foundation considering tensile crack failure. *Engineering Failure Analysis*, 125. <https://doi.org/10.1016/j.engfailanal.2021.105361>
- 48) U.S. Army Corps of Engineers. (2003). Time-history dynamic analysis of concrete hydraulic structures (Engineer Manual No. EM 1110-2-6051). U.S. Army Corps of Engineers. Washington, DC, USA. https://www.publications.usace.army.mil/Portals/76/Publications/EngineerManuals/EM_1110-2-6051.pdf
- 49) United States Army Corps of Engineers, Northwestern Division. (2012). Missouri River flood 2011: Vulnerabilities assessment report. U.S. Army Corps of Engineers. <https://usace.contentdm.oclc.org/digital/collection/p266001coll1/id/2186/>
- 50) Xu, G.; Guo, B.; Meng, Z.; Zhao, J.; Xue, Y. (2022). Seismic Safety Review of Gravity Dam Based on Finite Element Method. *Geofluids*, 2022, 5463613. <https://doi.org/10.1155/2022/5463613>
- 51) Yazdani, Y., & Alembagheri, M. (2017). Seismic vulnerability of gravity dams in near-fault areas. *Soil Dynamics and Earthquake Engineering*, 102, 15-24. <https://doi.org/10.1016/j.soildyn.2017.08.020>
- 52) Zhai, Y., Zhang, L., Cui, B., Zhang, H., & Ma, T. (2022). Evolution criteria of overall damage of concrete gravity dam body and foundation under near-fault ground motion. *Structures*, 43, 594–605. <https://doi.org/10.1016/j.istruc.2022.06.052>
- 53) Zhang, S., Wang, G., & Yu, X. (2013). Seismic cracking analysis of concrete gravity dams with initial cracks using the extended finite element method. *Engineering Structures*, 56, 528-543. <https://doi.org/10.1016/j.engstruct.2013.05.037>
- 54) Zou, D., Han, H., Liu, J., Yang, D., & Kong, X. (2017). Seismic failure analysis for a high concrete face rockfill dam subjected to near-fault pulse-like ground motions. *Soil Dynamics and Earthquake Engineering*, 98, 235-243. <https://doi.org/10.1016/j.soildyn.2017.03.031>

Appendix A — Abaqus input: Dam 1 (Modal Analysis)

*Heading

Dam D1: Modal Analysis

Units - n, m, sec

*Preprint, echo=NO, model=NO, history=NO, contact=NO

**

** PARTS

*Part, name=Part-1

*End Part

**

** ASSEMBLY

**

*Assembly, name=Assembly

**

*Instance, name =Part-1

*Node

1, 5., 30.

2, 0., 30.

401, 3.75, 34.5

402, 4.16666651, 34.5

403, 4.58333349, 34.5

*Element, type=CPE4R

1, 1, 9, 107, 68

*Nset, nset=Set-1, generate

1, 403, 1

*Elset, elset=Set-1, generate

1, 360, 1

** Section: Concrete

*Solid Section, elset=Set-1, material=Concrete

,

*End Instance

**

*Instance, name=Part-1-1, part=Part-1

*End Instance

**

*Nset, nset=Set-1, instance=Part-1-4

3, 4, 39, 40, 41, 42, 43, 44, 45, 46, 47, 48, 49

*Elset, elset=Set-1, instance=Part-1-4, generate

229, 240, 1

*Nset, nset=Set-2, instance=Part-1-4, generate

1, 403, 1

*Elset, elset=Set-2, instance=Part-1-4, generate

1, 360, 1

*Elset, elset=_Surf-1_S2, internal, instance=Part-1-4, generate

12, 288, 12

*Surface, type=ELEMENT, name=Surf-1

_Surf-1_S2, S2

*End Assembly

*Amplitude, name=Amp-Longitudinal

**

** MATERIALS

**

*Material, name=Concrete

*Damping, beta=0.003367

*Density

2400.,

*Elastic

2.5e+10, 0.15

*Concrete Damaged Plasticity

36.31, 0.1, 1.16, 0.667, 0.0001

*Concrete Compression Hardening

1.09375e+07, 0.

1.875e+07, 0.00025

2.34375e+07, 0.0005625

2.5e+07, 0.001

2.375e+07, 0.00155

2.25e+07, 0.0021

2.125e+07, 0.00265

*Concrete Tension Stiffening

3e+06, 0.

2.31e+06, 0.0014676
2.17286e+06, 0.00191309
2.03571e+06, 0.00241857
1.89857e+06, 0.00292406
1.76143e+06, 0.00342954
1.62429e+06, 0.00393503
1.48714e+06, 0.00444051
1.35e+06, 0.004946
1.245e+06, 0.0054502
1.14e+06, 0.0059544
1.035e+06, 0.0064586
930000., 0.0069628
825000., 0.007467
720000., 0.0079712
615000., 0.0084754
510000., 0.0089796
405000., 0.0094838
300000., 0.009988

*Concrete Compression Damage

0., 0.
0., 0.00025
0., 0.0005625
0., 0.001
0.05, 0.00155

0.1, 0.0021

0.15, 0.00265

*Concrete Tension Damage

0., 0.

0.23, 0.0014676

0.275714, 0.00191309

0.321429, 0.00241857

0.367143, 0.00292406

0.412857, 0.00342954

0.458571, 0.00393503

0.504286, 0.00444051

0.55, 0.004946

0.585, 0.0054502

0.62, 0.0059544

0.655, 0.0064586

0.69, 0.0069628

0.725, 0.007467

0.76, 0.0079712

0.795, 0.0084754

0.83, 0.0089796

0.865, 0.0094838

0.9, 0.009988

**

** BOUNDARY CONDITIONS

```

**
** Name: BC-1 Type: Displacement/Rotation
*Boundary
Set-4, 1, 1
**
** STEP: Step-1
**
*Step, name=Step-1, nlgeom=NO, inc=1000
*Static
1e-10, 1., 1e-10, 1.
**
** LOADS
**
** Name: Gravity Type: Gravity
*Dload
Set-1, GRAV, 9.81, 0., -1 *End Step
**
** STEP: Step-2 FrequencyExtraction
*Step, name="Step-2 FrequencyExtraction", nlgeom=NO, perturbation
*Frequency, eigensolver=Lanczos, sim=NO, acoustic coupling=on, normalization=displacement
4,
*Output, Field, variable=PRESELECT
*End Step

```

Appendix B — Abaqus input: Dam 1 (Seismic Analysis)

*Heading

Dam D1: Seismic Analysis

Units - n, m, sec

** Step 1: Gravity load

** Step 2: Hydrostatic pressure load

** Step 3: Earthquake

**

** Requires amplitude curves : Amp-Longitudinal

** Job name: Job-1 Model name: Dam D1-Site1-Longitudinal Acceleration

** Generated by: Abaqus/CAE 2023

*Preprint, echo=NO, model=NO, history=NO, contact=NO

**

** PARTS

*Part, name=Part-1

*End Part

**

** ASSEMBLY

**

*Assembly, name=Assembly

**

*Instance, name =Part-1

*Node

1, 5., 30.

2, 0., 30.

401, 3.75, 34.5

402, 4.16666651, 34.5

403, 4.58333349, 34.5

*Element, type=CPE4R

1, 1, 9, 107, 68

*Nset, nset=Set-1, generate

1, 403, 1

*Elset, elset=Set-1, generate

1, 360, 1

** Section: Concrete

*Solid Section, elset=Set-1, material=Concrete

,

*End Instance

**

*Instance, name=Part-1-1, part=Part-1

*End Instance

**

*Nset, nset=Set-1, instance=Part-1-4

3, 4, 39, 40, 41, 42, 43, 44, 45, 46, 47, 48, 49

*Elset, elset=Set-1, instance=Part-1-4, generate

229, 240, 1

```

*Nset, nset=Set-2, instance=Part-1-4, generate
  1, 403, 1
*Elset, elset=Set-2, instance=Part-1-4, generate
  1, 360, 1
*Elset, elset=_Surf-1_S2, internal, instance=Part-1-4, generate
  12, 288, 12
*Surface, type=ELEMENT, name=Surf-1
_Surf-1_S2, S2
*End Assembly
*Amplitude, name=Amp-Longitudinal
**
** MATERIALS
Will follow Same Material properties Mentioned in Appendix A (Frequency Extraction)
**
** BOUNDARY CONDITIONS
** Name: NBASE Type: Displacement/Rotation
**
** STEP: Step-1
*Step, name=Step-1, nlgeom=YES
*Static
1e-10, 1e-10, 1e-10, 1e-10
**
** LOADS
** Name: Gravity Type: Gravity

```

```
*Dload
Set-2, GRAV, 9.81, 0., -1.
**
** OUTPUT REQUESTS
** FIELD OUTPUT: F-Output-1
**
*Output, field, variable=PRESELECT
**
** HISTORY OUTPUT: H-Output-1
**
*Output, history, variable=PRESELECT
*End Step
**
** STEP: Step2-hydro
**
*Step, name=Step2-hydro, nlgeom=YES
*Static
1e-10, 1e-10, 1e-15, 1e-10
**
** LOADS
** Name: Hydrostatic Load  Type: Pressure
*Dload
Surf-1, HP, 313920., 32., 0.
**
```

```
** OUTPUT REQUESTS
**
** FIELD OUTPUT: F-Output-1
**
*Output, field, variable=PRESELECT
**
** HISTORY OUTPUT: H-Output-1
**
*Output, history, variable=PRESELECT
*End Step
**
** STEP: Step-3Earthquake
**
*Step, name=Step-3Earthquake, nlgeom=YES, inc=5000
*Dynamic,haftol=1e+07
0.02,38.96,1e-15,0.02
**
** BOUNDARY CONDITIONS
** Name: BC-2 Type: Acceleration/Angular acceleration
*Boundary, amplitude=Amp-Longitudinal, type=ACCELERATION
Set-1, 1, 1, 9.81
**
** OUTPUT REQUESTS
**
```

*Restart, write, frequency=0
**
** FIELD OUTPUT: F-Output-1
**
*Output, field, variable=PRESELECT, frequency=1
**
** FIELD OUTPUT: F-Output-2
**
*Output, field
*Element Output, directions=YES
DAMAGET,
**
** HISTORY OUTPUT: H-Output-1
**
*Output, history, variable=PRESELECT, frequency=1
*End Step

Appendix C — Abaqus input: Dam 2 (Seismic Analysis)

*Heading

Dam D2: Seismic Analysis

Units - n, m, sec

** Step 1: Gravity load

** Step 2: Hydrostatic pressure load

** Step 3: Earthquake

**

** Requires amplitude curves : Amp-Longitudinal

** Job name: Job-1 Model name: Dam D2-Sitel-Longitudinal Acceleration

** Generated by: Abaqus/CAE 2023

*Preprint, echo=NO, model=NO, history=NO, contact=NO

**

** PARTS

*Part, name="Dam body"

*End Part

**

** ASSEMBLY

**

*Assembly, name=Assembly

**

*Instance, name="Dam body-1", part="Dam body"

*Node

1, 5., 82.

2, 0., 82.

818, 4.5, 89.

819, 4.75, 89.

*Element, type=CPE4R

1, 1, 9, 155, 104

2, 9, 10, 156, 155

Nset, nset=Set-1, generate

1, 819, 1

*Elset, elset=Set-1, generate

1, 760, 1

** Section: concrete

*Solid Section, elset=Set-1, material=Concrete

*End Instance

*Nset, nset=Set-1, instance="Dam body-1", generate

1, 819, 1

*Elset, elset=Set-1, instance="Dam body-1", generate

1, 760, 1

*Nset, nset=Set-2, instance="Dam body-1"

3, 4, 57, 58, 59, 60, 61, 62, 63, 64, 65, 66, 67, 68, 69, 70

71, 72, 73, 74, 75

*Elset, elset=Set-2, instance="Dam body-1", generate

581, 600, 1

*Elset, elset=_Surf-3_S2, internal, instance="Dam body-1", generate
20, 680, 20

*Surface, type=ELEMENT, name=Surf-3
_Surf-3_S2, S2

*End Assembly

*Amplitude, name=Amp-Longitudinal

MATERIALS

**

Will follow Same Material properties Mentioned in Appendix A (Frequency Extraction)

**

** STEP: Step-GRAVITY

**

*Step, name=Step-GRAVITY, nlgeom=YES

*Static

1e-10, 1e-10, 1e-15, 1e-10

**

** BOUNDARY CONDITIONS

**

** Name: NBASE Type: Displacement/Rotation

*Boundary

Set-12, 1, 1

**

** LOADS

**

** Name: GRAVITY LOAD Type: Gravity

*Dload

Set-11, GRAV, 9.81, 0., -1.

**

** OUTPUT REQUESTS

**

*Restart, write, frequency=0

**

** FIELD OUTPUT: F-Output-1

**

*Output, field, variable=PRESELECT

**

** HISTORY OUTPUT: H-Output-1

**

*Output, history, variable=PRESELECT

*End Step

**

** STEP: Step-Hydro

*Step, name=Step-Hydro, nlgeom=YES

*Static

1e-10, 1e-10, 1e-15, 1e-10

**

** LOADS

**

```
** Name: hydro  Type: Pressure
*Dload
Surf-3, HP, 843660., 86., 0.
**
** OUTPUT REQUESTS
***
** FIELD OUTPUT: F-Output-1
**
*Output, field, variable=PRESELECT
**
** HISTORY OUTPUT: H-Output-1
**
*Output, history, variable=PRESELECT
*End Step
**
** STEP: Step-3 earthquake
**
*Step, name="Step-3 earthquake", nlgeom=YES, inc=5000
*Dynamic,haftol=1e+07
0.02,38.96,1e-15,0.02
**
** BOUNDARY CONDITIONS
**
** Name: BC-2 Type: Acceleration/Angular acceleration
```

*Boundary, amplitude=Amp-Longitudinal, type=ACCELERATION

Set-12, 1, 1, 9.81

**

** OUTPUT REQUESTS

**

** FIELD OUTPUT: F-Output-1

**

*Output, field, variable=PRESELECT, frequency=1

**

** FIELD OUTPUT: F-Output-2

**

*Output, field

*Element Output, directions=YES

DAMAGET,

**

** HISTORY OUTPUT: H-Output-1

**

*Output, history, variable=PRESELECT, frequency=1

*End Step